Characterisation and Remediation of Depleted Uranium Munitions Residues and Aqueous Chromium (VI)

Daniel Edward Crean

A thesis presented for the degree of Doctor of Philosophy

October 2013

The University of Sheffield

Faculty of Engineering

Department of Materials Science and Engineering

Abstract

Depleted uranium (DU) munitions particles and aqueous chromium(VI) are hazardous and challenging toxic metal contaminants. This thesis develops new approaches for remediating these pollutants, and provides insight into the long term behaviour of DU contamination by characterisation of environmentally aged residues.

DU munitions particles exposed to the environment for ~25 years were studied using synchrotron X-ray chemical imaging. Micron-scale domains of U speciation were resolved in particles, indicating heterogeneous formation conditions and a variable extent of particle weathering. Two soil samples from a UK firing range were shown to have different U speciation, linked to environmentally mediated alteration in one soil. This study represents a novel application of X-ray chemical imaging to U in environmental materials, allowing domains of U(IV), U(V) and U(VI) to be resolved. An aged particle containing $UFeO_4$ was shown to contain U(V), providing new evidence for the stability of this oxidation state under environmental conditions.

Remediation of DU contaminated soils was studied by chemical extraction using bicarbonate, sulfric acid and citric acid lixivants. Single batch extraction in bicarbonate was the most effective, and able to remove 50% total DU. Residual particles showed partially leached microstructures, and the formation of secondary phases. An alternating pH multi-batch extraction was developed to promote secondary phase dissolution and improve the decontamination yield to a maximum of 87% total DU.

In the last section, remediation of aqueous Cr(VI) was studied by reduction to insoluble Cr(III) using a hybrid Pd functionalised biomineral, magnetite. A means to increase the reactive capacity of the Pd-magnetite was demonstrated by addition of sodium formate, and the system performance was not affected by dissolved oxygen or nitrate. Using advanced spectroscopic and microscopic techniques, analysis of the reacted mineral showed Cr(III) was retained in the magnetite structure, and Pd recrystallisation resulted in a loss of reductive capacity.

Acknowledgements

This thesis would not have been possible without the collaboration, input, advice and support of a number of people.

First off, I want to sincerely thank my primary academic supervisor, Neil Hyatt, for the constant stream of technical advice, encouragement, guidance and inspiration - and for more than a few beers! Neil has always pushed me throughout my PhD, and opened more than a fair number of doors, and I'd really like to thank him for helping to make the past few years such an interesting and enjoyable time. I also thank my second supervisor, Francis Livens (University of Manchester) for his input, discussions and advice along the way, and for braving the Irish Sea to get stuck in with digging up soil at Eskmeals.

I want to thank Daniel Grolimund and Camelia Borca at the Swiss Light Source for working with me on the microfocus X-ray experiments that make up a rather large portion of this thesis. It was a great opportunity to go out and do some work at SLS, and the efforts of Daniel and Camelia in obtaining and making the most out of this time are greatly appreciated.

Thanks are also due to Mustafa Sajih (Manchester) for help getting the project going, Martin Stennett (Sheffield) for keeping me sane on beam time and help with all things XAS, and Paul Heath (Sheffield) for giving up his time to help out on our second trip to SLS.

The final experimental chapter of this thesis is the product of some work done in the School of Earth and Atmospheric Sciences at the University of Manchester at the start of my PhD. I'd like to particularly thank Vicky Coker for her help in every aspect of this work, Jon Lloyd for his supervision during this time, and the geomicrobiology group for making it a great place to start!

I've been very fortunate to be part of two interesting and dynamic research groups, the Immobilisation Science Laboratory here in Sheffield, and the Centre for Radiochemistry Research at the University of Manchester. Thanks to all the people who I've shared office space with over the past three years for plenty of welcome distraction, interesting chat and seriously strong rounds of coffee. Particular nods of thanks to the many ISL people - Kris, Paul H, Sam,

Martin, Jimmy, Claire, Amy, Laura G, Neda, Dans B and B, Swifty, Silvia and Oday, and Manchester chemists - Dan W, Kurt, Chris G, Mustafa, and Saif who have made the past few years substantially more fun than they otherwise might have been!

The Engineering and Physical Sciences Research Council (EPSRC) are thanked for providing funding for my studentship through the Nuclear First DTC grant. Funding for the Swiss Light Source was provided through the Actinet i3 project, funded by the European Commission/Euratom. The work in Chapter 7 was supported by Nametech, a Collaborative Project co-funded by the Research DG of the European Commission, the EPSRC University of Manchester Knowledge Transfer Account (KTA) and the Leeds EPSRC Nanoscience and Nanotechnology Research Equipment Facility (LENNF).

I want to say thanks to my family (Mum, Dad, Tom and Hannah) and friends for their support during my PhD studies. And finally to Emma, for her love and support throughout.

Table of Contents

List of figures with captions

List of tables with captions

Chapter 1

Introduction

1.1 Background

Contamination of the environment with various toxic metals as a result of industrial and military activity is a worldwide problem. Engineered intervention to reduce the risks of exposure to these contaminants is termed remediation, and can range from monitoring natural attenuation of contaminant concentrations to excavation of contaminated soils for disposal as hazardous waste. However, wholesale disposal of soils and sediments can be impossible or prohibitively expensive. Many remediation technologies aim instead to achieve risk reduction by removing contaminants from the environmental matrix or preventing transport of a contaminant into the biosphere by immobilising it in-situ.

This thesis investigated options for the remediation of two challenging contaminants, depleted uranium (DU) particles and aqueous chromate (CrO_4^{2-}). The focus for DU particles was their removal from contaminated soils through chemically enhanced leaching, whereas remediation of aqueous chromate contamination was investigated by reductive immobilisation using a biogenic Fe(II) bearing mineral, magnetite (Fe_3O_4).

1.2 Depleted Uranium Particles - Characterisation and Remediation

Depleted uranium (DU) particles are produced by military use in armour piercing munitions, and are dispersed widely in the environment following impact with an armoured target [1]. Uranium is a highly toxic radioactive heavy metal, and the presence of DU particles in the environment can pose a risk to human health [2, 3]. Decontamination of soils has been investigated by physical separation [4], radiometric isolation of fragments [5, 6] and dissolution of particles with recovery of DU in a liquid phase [7, 8]. However, these approaches have not

yet reached field application, although some heavily DU contaminated sites have been remediated by bulk disposal of soil [9]. There is a need to continue the development and testing of these remediation technologies such that there are options for reliable, cost-effective decontamination of DU residues where an environmental risk assessment may require it. One of the objectives of this project was to develop the use of chemical extraction as a potentially viable route for low cost decontamination of munitions DU.

The lack of field deployable remediation technology means that for the majority of DU munitions sites, decontamination is currently impracticable. There is then a need to consider the long term behaviour of DU particles in the environment to improve understanding of how the risk from this contamination changes over time. Any changes in DU speciation caused by weathering will also have an impact on remediation, as for many decontamination technologies the efficiency is strongly linked to the contaminant properties [10, 11]. One of the main themes of this thesis is the characterisation of aged DU munitions particles, both to understand their developing environmental fate and potential impacts on the remediation of DU contaminated soils.

Characterisation of complex particles for their environmental behaviour requires a means to spatially resolve chemical information, as heterogeneities in speciation linked to alteration processes may be obscured by bulk techniques. In this project synchrotron X-ray imaging, complemented by electron microscopy, was used to probe micron scale gradients in U speciation, particle composition and morphology.

1.3 Remediation of Aqueous Chromium (VI) Contamination

Chromium (VI) is used in a number of industrial processes including metal plating, leather tanning, as a corrosion inhibitor and in nuclear fuel reprocessing [12], which has led to its release to the environment. Chromium(VI) is a strong oxidant, and is highly toxic and carcinogenic [13]. As an oxyanion, chromate (CrO_4^{2-}) is also highly mobile in the environment

and interacts weakly with mineral surfaces, which increases the risk of migration into the biosphere [14].

As the risk posed by Cr(VI) is linked directly to its high mobility in aqueous environmental systems, the objective of remediation is typically to prevent further migration of toxic chromate species, by reduction to insoluble Cr(III) [14]. One means to achieve this is deployment of a permeable reactive barrier (PRB) which is installed in the flow path of contaminated water and consists of a material which can effectively reduce and immobilise Cr(VI). Such materials must be selective for Cr(VI) reduction, as other oxidising species such as nitrate (NO_3^-) are often present in high concentrations in industrially contaminated waters. This has shown to be a key flaw in the performance of some candidate materials such as zero-valent iron [15]. Development of materials of high reductive capacity with respect to Cr(VI) is an important research goal in the engineering of effective Cr(VI) remediation. The objective of the final part of this thesis was to investigate the reactivity of a novel functionalised biogenic mineral system for reduction of Cr(VI) in the presence of oxidising co-contaminants.

1.4 Aims and Objectives

This thesis has three main research themes which develop the characterisation and remediation of toxic metal affected environments. These themes, and associated project objectives are:

(i) Characterisation of environmentally aged DU munitions particles. The main aim of this theme is to improve understanding of the interaction of DU particles with the surface environment over periods of years to decades. This was undertaken by characterising environmentally aged particles using electron microscopy and synchrotron X-ray microanalysis. A second objective of this work was to probe soil geochemical influences on DU behaviour by characterisation of particles recovered from distinct sample sites.

(ii) Remediation of soils contaminated with DU munitions particles. The basis for this theme was to evaluate the application of a chemical leaching methodology for DU remediation on contaminated soils. To improve understanding of this process, an objective was to characterise

residual particles to provide insight on the mechanism of chemical extraction and identification of recalcitrant U phases. Using this characterisation data, the aim was to explore routes to optimise and improve the chemical leaching processes.

(iii) Improving the reductive removal of Cr(VI) from contaminated waters. The aim of the final theme was to build on previous work in remediating Cr(VI) with Fe(II) bearing biominerals [16] by functionalising the surface of biogenic magnetite with Pd. The objective was to evaluate the extent to which the Pd-functionalised surface may act as a heterogeneous catalyst to recharge magnetite reactivity when supplied with a suitable electron donor. The performance of this system to remove Cr(VI) from solution in the presence of dissolved oxygen and an oxidising co-contaminant (NO_3^-) was also studied. The final objective was to improve understanding of the reduction mechanism, chromium retention and eventual loss of reductive capacity in the system by characterising Pd-functionalised magnetite reacted with Cr(VI).

1.5 Thesis Structure

Chapter 2 provides a review of the relevant literature related to the environmental behaviour and remediation of munitions DU and Cr(VI), with more specific introductions for each section of work presented at the start of each chapter. Experimental procedures are covered in a similar style, Chapter 3 outlines the various analytical techniques with a brief theoretical background and justification for their use, with specific procedures and details covered in the relevant experimental chapter. This style may result in some limited repetition, but has the advantage of allowing the results chapters to be read without repeated reference to the opening chapters, whilst still providing the reader with an appropriate background to the research presented in this thesis.

The experimental chapters are divided by the themes discussed above (section 1.4). Chapters 4 and 5 present the results of characterisation of environmentally aged DU particles. Chapter 4 reports micro analytical X-ray imaging of DU speciation in particles from two distinct sampling

sites. The ternary oxide $UFeO_4$ was discovered in a DU particle, and an extensive characterisation of U valence in this unusual compound is presented in Chapter 5.

Chapter 6 details the development of an alternating reagent batch chemical leaching system for the remediation of the soils contaminated with DU particles characterised in Chapter 4. The third theme is covered in Chapter 7, which deals with the characterisation of a functionalised biogenic magnetite system for selective and sustained removal of chromium VI in contaminated waters. This part of the thesis was conducted during a project rotation at the University of Manchester as part of the Nuclear First Doctoral Training Centre programme.

In the final chapter, conclusions from each of these three research themes are synthesised and discussed from the results presented in each respective chapter. Further work in each of these areas is outlined, along with discussion of a potential comparative project on heavy metal munitions contamination using the soil samples studied in this thesis.

1.6 References

[1] Bleise, A.; Danesi, P. R.; Burkart, W., Properties, use and health effects of depleted uranium (DU): a general overview. *Journal of Environmental Radioactivity* **2003,** *64*, (2-3), 93-112.

[2] Briner, W., The Toxicity of Depleted Uranium. *International Journal of Environmental Research and Public Health* **2010,** *7*, (1), 303-313.

[3] Briner, W. E., The evolution of depleted uranium as an environmental risk factor: lessons from other metals. *Int J Environ Res Public Health* **2006,** *3*, (2), 129-35.

[4] Larson, S.; Ballard, J.; Medina, V.; Thompson, M.; O'Connor, G.; Griggs, C.; Nestler, C. Separation of Depleted Uranium From Soil; *Engineer Research and Development Centre, Vicksburg MS Environmental Labs*: **2009**.

[5] Miller, M.; Galloway, B.; VanDerpoel, G.; Johnson, E.; Copland, J.; Salazar, M., An Alternative for Cost-Effective Remediation of Depleted Uranium (DU) at Certain Environmental Restoration Sites. *Health Physics* **2000,** *78*, S9-S12.

[6] Farr, C. P.; Alecksen, T. J.; Heronimus, R. S.; Simonds, M. H.; Farrar, D. R.; Miller, M. L.; Baker, K. R., Recovery of Depleted Uranium Fragments from Soil. *Health Physics* **2010,** *98*, (2), S6-S11

[7] Choy, C. C.; Korfiatis, G. P.; Meng, X. G., Removal of depleted uranium from contaminated soils. *Journal of Hazardous Materials* **2006,** *136*, (1), 53-60.

[8] Mason, C. F. V.; Turney, W.; Thomson, B. M.; Lu, N.; Longmire, P. A.; ChisholmBrause, C. J., Carbonate leaching of uranium from contaminated soils. *Environmental Science & Technology* **1997,** *31*, (10), 2707-2711.

[9] Salbu, B.; Janssens, K.; Lind, O. C.; Proost, K.; Gijsels, L.; Danesi, P. R., Oxidation states of uranium in depleted uranium particles from Kuwait. *Journal of Environmental Radioactivity* **2005,** *78*, (2), 125-135.

[10] Gavrilescu, M., Emerging processes for soil and groundwater cleanup – potential benefits and risks. *Environmental Engineering and Management Journal* **2009,** *8*, (5), 1293-1307.

[11] Gavrilescu, M.; Pavel, L. V.; Cretescu, I., Characterization and remediation of soils contaminated with uranium. *Journal of Hazardous Materials* **2009,** *163*, (2-3), 475-510.

[12] He, Y. T.; Traina, S. J., Cr(VI) reduction and immobilization by magnetite under alkaline pH conditions: The role of passivation. *Environ. Sci. Technol.* **2005,** *39*, (12), 4499-4504.

[13] Costa, M.; Klein, C. B., Toxicity and carcinogenicity of chromium compounds in humans. *Crit. Rev. Toxicol.* **2006,** *36*, (2), 155-163.

[14] Richard, F. C.; Bourg, A. C. M., Aqueous geochemistry of chromium - a review. *Water Res.* **1991,** *25*, (7), 807-816.

[15] Rivero-Huguet, M.; Marshall, W. D., Impact of various inorganic oxyanions on the removal rates of hexavalent chromium mediated by zero-valent iron. *Environ. Chem.* **2010,** *7*, (3), 250-258.

[16] Cutting, R. S.; Coker, V. S.; Telling, N. D.; Kimber, R. L.; Pearce, C. I.; Ellis, B. L.; Lawson, R. S.; der Laan, G. V.; Pattrick, R. A. D.; Vaughan, D. J.; Arenholz, E.; Lloyd, J. R., Optimizing Cr(VI) and Tc(VII) remediation through nanoscale biomineral engineering. *Environ. Sci. Technol.* **2010,** *44*, 2577-2584.

Chapter 2

Literature Review

2.0 Introduction

This chapter presents a review of previous work related to the environmental behaviour and remediation of depleted uranium munitions particles and chromium (VI) contamination. In each of the subsequent results chapters a shorter, more focussed review of relevant literature is included as introduction to that section of the thesis.

The first section of this chapter gives an introduction to the environmental chemistry of munitions depleted uranium, which is followed by a more detailed review of the literature relating to the characterisation of DU munitions particles. The second section details remediation of depleted uranium munitions, identifying and reviewing technologies which may be applicable to the removal of DU particles from soil. The final section introduces the environmental behaviour of chromium (VI) and reviews methods to remediate this contamination, with a focus on the Fe(II)/Fe(III) mineral, magnetite (Fe_3O_4)

2.1 Depleted Uranium Munitions Particles

2.1.1 Uranium in the Environment

Uranium is a naturally occurring radioactive heavy metal that is ubiquitous in the Earth's crust [1]. The uranium concentration in terrestrial rocks and soils is in the range of 0.3 – 11.7 ppm [2], with an average of 3 ppm [3]. Natural uranium is a combination of three radioisotopes, ^{234}U (0.0055 atom %), ^{235}U (0.72%) and ^{238}U (99.27%). Of these isotopes ^{235}U can undergo fission, which has led to the exploitation of uranium as a fuel for nuclear weapons and electricity generation.

The industrial and military use of uranium has led to localised contamination of the environment at various locations worldwide. Activities such as mining and milling of uranium

ore, nuclear fuel reprocessing, and improper waste disposal have resulted in substantial release of uranium to the environment [4]. Uranium is chemically toxic and radioactive [5], and its presence and transport in the environment has raised concern about the impacts of uranium contamination on environmental quality and human health.

The mobility of uranium in the environment is linked to its chemical speciation, which is influenced by soil properties such as pH, the presence of complexing species, and the action of micro-organisms. One of the key chemical controls on mobility is the U oxidation state. Uranium can exist in oxidation states +3, +4, +5 and +6, but only the +4 and +6 oxidation states are stable in aqueous systems, and consequently are the most important oxidation states in the natural environment. Under reducing conditions, U(IV) species are stabilised, whereas under the oxidising to slightly reducing conditions usually encountered in the near surface environment, U(VI) is stable. U(IV) species have low solubility and environmental mobility under alkaline and mildly acid conditions because U^{4+} is readily hydrolysed or sorbed to mineral surfaces [1]. In contrast, U(VI) forms the uranyl dioxocation UO_2^{2+} and has higher solubility, environmental mobility and bioavailability [6, 7]. The oxidation-reduction between U(VI) and U(VI) is an important control on the fate of uranium in the environment, and the risk that U contamination poses.

The mobility of U(VI) in a system is strongly dependent on local geochemical conditions. Uranium(VI) as the uranyl ion readily complexes with ligands naturally present in groundwaters. In particular, uranyl forms strong complexes with carbonate (CO_3^{2-}) in oxic waters at circumneutral and alkaline conditions [8]. The formation of soluble carbonate species such as UO_2CO_3, $UO_2(CO_3)_2^{2-}$ and $UO_2(CO_3)_3^{4-}$ [4] enhances the mobility of uranyl by impairing mineral sorption and hydrolysis reactions. The presence of carbonate can be a key mediator of the solubility and mobility of uranium in a system [9]. U(VI) can precipitate with a range of anions such as hydroxide, silicate, carbonate, phosphate, arsenate and vanadate [1], and is susceptible to sorption by Fe oxyhydroxides [10] and organic matter, which serve to reduce the mobility of U in a system.

2.1.2 Natural and Depleted Uranium

The primary industrial use for uranium is as a fuel in thermal nuclear reactors for electricity generation. Although some reactor designs can accept natural uranium, the majority of modern reactors require a higher relative concentration of fissile ^{235}U (~ 3 atom %) in order to sustain a chain reaction. The creation of uranium enriched in ^{235}U produces a stream of 'depleted' uranium (DU) - a waste product that contains a lower relative concentration of ^{235}U (typically between 0.2-0.3%) and ^{234}U (0.001%). As the specific activities of the isotopes ^{234}U and ^{235}U are higher than ^{238}U, the altered isotopic composition makes DU around 40% less radioactive than purified natural uranium (Table 1).

Table 1 – Isotopic composition of natural uranium and depleted uranium by weight, radioactivity and specific activity (Bq/g).

Isotope	Weight % [3]		Activity %		Contribution to Total Activity (Bq/g U) [3]	
	Natural U	Depleted U	Natural U	Depleted U	Natural U	Depleted U
U-234	0.006	0.001	48.9	15.2	12.4	2.26
U-235	0.72	0.2	2.2	1.1	0.57	0.16
U-238	99.3	99.8	48.9	83.7	12.4	12.4
Total	-	-	-	-	**25.3**	**14.8**

Although not useful as a fuel in current thermal neutron reactor systems, depleted uranium has found a number of commercial applications. In civilian uses it is employed as an aircraft counterweight, in radiation shielding, as a catalyst and it has potential for use in breeder reactors [11]. It is used in military applications as armour plating and armour piercing munitions [3].

The exploitation of DU in these various technological roles has resulted in its release to the environment. Aircraft crashes, such as that which occurred in Amsterdam in 1992, may release large amounts (*ca* 150 kg) of DU as counterweights are destroyed on impact [12]. Industrial processing activities have also resulted in localised release of DU from fabrication plants [13].

However, its use in munitions has resulted in the majority of widespread DU release to the environment [14].

Ammunition containing DU has been used by NATO forces in conflicts in Iraq and Kuwait in 1991 (320 tonnes) and 2003 (not disclosed), Bosnia-Herzegovina in 1995 (3 tonnes) and Kosovo in 1999 (10 tonnes) [3]. Testing of DU weapons and armours in countries including the USA and UK has also resulted in localised contamination of firing ranges [15-17].

2.1.3 Depleted Uranium Munitions

The main military use of depleted uranium is kinetic energy munitions, which are designed to pierce the armour of modern tanks. These weapons carry no explosive charge, consisting of a dart of 99.25% DU - 0.75% Ti alloy mounted in an aluminium sabot, which allows it to be fired from a normal tank gun at speeds of up to 1.8 km/s [14]. Due to the high density of metallic uranium (19 g/cm^3), this speed amounts to sufficient kinetic energy to pierce complex amour plate. In addition, metallic uranium has unique properties that make it more attractive than similarly dense materials such as tungsten (ρ = 19.3 g/cm^3). When a uranium dart strikes armour plate, it interacts in a self-sharpening mechanism whereby fragments of DU are discarded from the penetrator-target interface [18]. In tungsten rounds this does not occur, leading to the formation of blunt 'mushroomed' tip, which decreases penetrative power compared to DU.

Metallic uranium is also pyrophoric (meaning it will spontaneously combust in air) and has a low melting point (1132°C for metallic U), which under high temperature conditions on impact causes the formation of uranium aerosols which are dispersed and ignited. This combustion increases damage to the target and is a major advantage of DU over tungsten, which is not pyrophoric [14, 19]. Many years of enriching uranium for nuclear fuel have created large stockpiles of depleted uranium, making it easily accessible and relatively low cost compared to other dense materials [3].

2.1.4 DU Munitions in the Environment

DU associated with munitions enters the environment by two main routes – settling of dust and aerosol particles produced on impact, and deposition of metallic fragments or whole penetrators,

the products of which display distinct physiochemical characteristics [15, 20]. Munitions DU has also been released to the environment during accidents such as a munitions depot fire [21], but such events represent a minor fraction compared to combat use.

Uranium oxide dusts created by pyrophoric oxidation of small fragments and aerosols produced on impact with a hard target are found in surface areas surrounding a DU strike site [22]. These dusts have a small characteristic size with median aerodynamic diameter d < 15μm [23], which can result in wide dispersal of this material in the environment. Due to small characteristic size, DU dust particles may be subject to resuspension in winds and physical transport in soils, as well as being redistributed over longer terms by weathering reactions which may liberate U(VI) species

The remaining penetrator mass and DU rounds that miss the intended target may become buried in soils intact or as large fragments at depths of up to 2 m in clay soils and 7 m in sandy soils [20, 24]. Munitions grade DU alloys deposited in oxic or suboxic soils undergo corrosion, generating uranium rich minerals, oxides and soluble UO_2^{2+} species [20]. These species may migrate in the environment and DU penetrators can act as a source of mobile U under these redox regimes. Under sufficiently reducing conditions, U(IV) is stabilised and an insoluble passivating film forms on the surface of the metallic fragment, preventing further corrosion and dissolution [20].

These two distinct routes of DU deposition in the environment present different hazards to human health and the environment. Although in most cases the production of impact particulates accounts for a minority of the total mass (10 - 35% [25]) of DU released into the environment [24], the exposure risks posed by this material are significant due to its predominance in the near surface [5, 26]. Whilst the corrosion of large fragments of DU metal may result in the delayed long-term release of substantial quantities of uranium to the environment [20], the presence of particulate in surface soils presents an immediate near term inhalation risk due to the potential for resuspension of DU fines. In most scenarios, inhalation of dust particles is thought to be the most significant route of exposure for survivors, clean up

personnel and civilians [26]. Over longer periods of time, corrosion and alteration of the particles may also act as a source of mobile U(VI) in the surface environment.

Whilst a number of recent investigations have probed the corrosion and alteration of metallic munitions grade DU alloys [20, 27-30], there has been little emphasis on assessing the long term behaviour of impact residues. One focus of this thesis is to address this uncertainty by characterising environmentally aged residues from a UK firing range. Investigation of particle physiochemical properties, especially U speciation, will improve understanding of how the risk posed by this contamination will change over extended periods of time in the environment.

2.1.5 Characterisation of Depleted Uranium Munitions Particles

Although the long term behaviour of DU munitions particles in uncertain, their properties have been extensively characterised after short periods of environmental exposure. Residues were recovered from Kosovo in 1999 and 2000 [31-34] and Kuwait in 2002 [21, 32] during UN/IAEA post-conflict environmental assessments. Particles produced directly by test firing, which were not exposed to the environment, have also been characterised [18, 35, 36]. This section reviews the findings of these studies to generate a picture of U particle properties on formation, and to understand their short term behaviour in the environment. This is a required point of comparison for the characterisation of aged particles which are investigated in this thesis.

2.1.5.1 Composition and Uranium Speciation

Pyrophoric oxidation of the metallic uranium penetrator generates uranium oxides as the dominant species in DU particles [21, 33]. Minor presence of non-oxide phases such as metallic uranium, UC, UFe_2 [32] and unidentified mixtures of uranium, aluminium and iron also reported, indicative of penetrator-target interaction [15, 18]. DU particles are polycrystalline, with the majority composed of UO_2, U_3O_8 [15, 21, 33, 37] and varying proportions of UO_3, U_3O_7, U_2O_5 and U_4O_9 as minority components [18, 33, 35, 36]. This variation in the proportion and stoichiometry of uranium oxide phases reflects heterogeneities in the high energy formation

of these materials. In general, these oxides of uranium are considered to have among the lowest solubility and bioavailability of all uranium species [37].

2.1.5.2 Morphology and Structure

DU impact particles most often have a spherical morphology, characteristic of solidification from liquid drops of molten uranium [18]. This formation controlled characteristic morphology is observed in environmental samples, suggesting limited alteration over the reported timescales [15, 33]. Spheres with rough or lobed surfaces are common [18, 31, 37], and some have been found to be cracked or hollow. A combustive heating process which results in volatilisation and venting of the internal material leaving a hollow shell [38] was suggested as a possible formation route for these particles, due to the pyrophoricity of metallic U and UO_2 [37]. In addition to spherical particles, particles with morphologies resulting from fragmentation and shearing processes are produced by self-sharpening whereby fragments of DU are ejected from the penetrator/target interface and the sharp tip of the dart is retained [18, 37].

2.1.5.3 Formation Conditions

Particle characteristics can give indication of the conditions which occur during impact of DU penetrators with armour plate. Branched Fe/Al rich regions indicative of vaporisation of Fe (T_V = 2861°C) and Al (T_V = 2581°C) but not U (T_V = 4131°C) are observed in some samples, which gives an upper banding of the temperature [18]. The impact temperature must be higher than the melting point of metallic uranium (1183°C) which accounts for the presence of spherical, drop-cooled particles. Krupka *et. al.* estimated the instantaneous temperature reaches up to 3000°C on impact [18].

Partial oxidation of uranium from U(0) to mainly U(IV) rather than U(VI) gives indication that the reaction was quenched rapidly, with variation in U-O stoichiometry between UO_2, U_4O_9, U_3O_7 and U_3O_8 suggesting that oxidation conditions were variable. In comparison, DU residues produced by prolonged oxidation in a munitions fire were fully oxidised to U(VI) species [21].

2.5.1.4 Short Term Environmental Stability

Comparison of DU particles studied from deposition in different environments, e.g. arid soils in Kuwait [32], variably moist soils in Kosovo [34] and the UK [15], and particles which have not been exposed to the environment [18] shows that particle properties are generally independent of the environmental history of the material. In the near term, particle properties are controlled by the formation processes during impact and not by interaction with the surface environment. This suggests that DU residues have a degree of stability in the surface environment over the short time scale between deposition and sampling, typically 1-3 years in the majority of environmental studies [33, 34, 39], up to a maximum of 11 years in arid Kuwait soils [21].

Due to this short time scale there is uncertainty surrounding the evolution of impact particle properties with time in the environment. Variably moist, oxic conditions in the near surface would be expected to promote the oxidation and dissolution of uranium oxides to mobile U(VI) species [8, 40]. This will change the behavior of DU in these systems, and there is a need to investigate particle behavior over longer periods of time in the environment. An analogue study of aged contamination arising from burning of scrap U metal at a processing plant in Colonie, NY, USA [13, 41] showed that U oxide particles can persist in the environment for over 25 years with little extent of weathering [37]. The compositions and morphologies of particles in this study suggest they are a reasonable analogue for DU [37], and there is a need to compare the results of this study with data on aged DU particles under a range of environmental conditions to gain further insight into the long term fate of U oxide particles in the surface environment.

2.2 Remediation of Land Contaminated with DU Munitions Residues

2.2.1 Risks Associated with Exposure to DU

Uranium is radioactive and highly chemically toxic, and exposure to large quantities can present a serious health hazard [42]. The main radioactive emission from purified uranium is alpha particles, which have low penetrating power and are stopped easily by the skin, meaning that the external radiation hazard from DU is not considered to be significant [14]. However, alpha

emitters are a serious health hazard inside the body, which with the substantial chemical toxicity of uranium [43] means DU is considered a serious internal health hazard [42].

The primary risk to health is the intake of DU into the body by ingestion, inhalation or wounding, of which inhalation of dusts from hard target impacts is considered the most significant near term pathway [26]. Due to the low solubility of uranium oxide phases produced by DU impacts [32], particles can persist in the body for long periods, particularly in the lungs where particles are deposited on inhalation [44]. Although the acute chemical toxicity of uranium is well established, the effects of long term low-level exposure are still unclear [5]. Chronic, sub-acute exposure to DU has been suggested to cause similar adverse health problems to lead exposure due to some similarities in their biological behaviour [5, 26]. The near term risks to public health from impact dusts and uncertainty surrounding the long term risks of chronic DU exposure have driven concerns about the presence of DU in the surface environment following its use in conflict.

2.2.2 Drivers for Remediation

In heavily contaminated areas, it may be necessary to remove DU dusts from the environment to avoid further dispersal and prevent long-term exposures, thereby reducing the risk to public health. Current operational practice for the clean-up of heavily contaminated DU soils involves excavation and removal of soil to a hazardous waste or low level radioactive waste (LLW) repository [17, 21]. The costs of disposing large volumes of soil in an LLW repository are high, and this may be prohibitive of applying this method to all contaminated sites. Methods to decontaminate bulk soils and separate DU contamination into a smaller volume for disposal are therefore attractive.

There is a wide body of literature covering remediation of uranium contamination (recently reviewed by Gavrilescu *et. al*. [4, 45]), but many methods are not applicable to DU munitions residues as uranium is present in many contaminated soils as mobile U(VI) species rather than low solubility particulates [4]. Remediation of these sites focuses on reducing the risk associated with uranium transport by immobilisation of U(VI), usually by reduction to U(IV)

[45] or precipitation as low solubility phases, such as U(VI) phosphate species [46]. However, the risks from aqueous migration of munitions DU contamination are expected to be comparatively low due to the low solubility of U oxide phases in soils [32, 39, 47]. As DU is speciated as low solubility oxide particles, the hazards posed by particle resuspension, airborne transport and inhalation are more significant, and the objective of remediation will be to remove rather than immobilise DU contamination.

Although there have been reports of remediation schemes specific to DU munitions residues, the focus has been on removal of corrosion products [48, 49] or intact penetrators [50] rather than the surface aerosol contamination encountered at DU strike sites and firing ranges. Several options for removing DU impact residues from soil are considered in the following sections, with reference to remediation of soils contaminated with other low solubility uranium phases.

2.2.3 Physical Separation Processes

Physical separation processes are based on differences in characteristics such as size, shape, density, radioactivity or magnetism. Radiometric separation approaches have been proposed for heavily contaminated soils, but are generally only considered effective for large DU fragments due to the low specific activity of the material [50, 51].

A range of physical decontamination options including sieving and density separation were studied for soils at the Yuma Proving Ground, AZ, USA [17]. The efficiency of each method in removing DU from soils was sensitive to the extent of aging of the residues in the soil. Processes such as weathering and agglomeration with soil matrix particles change the apparent particle size and density of the contaminant residues, reducing the efficiency of physical separation processes. Although density separation was determined to be highly effective for removing impact particles from soils, the high cost of the very high density (ρ = 3.3 g/cm^3) liquids and reduced efficiency for agglomerated or weathered residues limit a large scale application [17].

2.2.4 Chemical Extraction by Soil Washing

Physical and radiometric separations are hindered by size redistribution processes and the low specific activity of DU, and a different approach is required to reliably remove impact residues from soils. Soil washing with chemical extraction could overcome these limitations by leaching DU phases directly from the soil with a reduced sensitivity to the physical properties of the contamination.

Soil washing refers to a range of wet treatment technologies that remove contaminants from soils by transfer into a liquid phase. As the goal of soil washing is removal of the contaminant, it is one of the main technologies that provide a permanent and irreversible treatment of metal contaminated soils [52]. Often soil washing is conducted with leaching solutions to increase mobilisation of contaminants into the liquid phase. The composition of the leaching solution depends on the nature of the contamination present, and for uranium, both inorganic (e.g. CO_3^{2-}, H_2SO_4) and organic (e.g. citrate, EDTA) ligands can be used with the aim of extracting the contaminant metal into a weakly sorbing complex ion, which can be removed from the soil in the liquid phase [45]. Many remedial chemical extraction technologies for uranium have a basis in mining processes. In particular, both CO_3^{2-} and H_2SO_4 are used to extract U from porous rocks in in-situ leaching processes, and in extracting uranium from conventionally mined ores in the milling stage of ore processing [1, 4, 45].

Remediation by chemical leaching requires careful control to prevent mobilisation and transport of contaminants out of the system and into the environment. One convenient way to realise this is to use ex-situ systems, such as heap leaching [53], a technique often used in the mining industry to extract metals from low grade ore [54, 55]. In a heap leaching system, soils are placed on a pad which isolates the heap from the environment and allows recovery of the leaching liquor, which can be recirculated to reduce fluid demand. Leaching in engineered systems such as heaps or tanks gives means to isolate mobilised contaminants from the geosphere, allowing safe recovery. However, ex-situ approaches require moving large volumes of contaminated soil, which can potentially mobilise fines, and in the case of soils with high

levels of radioactive contamination can cause additional radiation doses to be received by workers [4, 45].

2.2.4.1 Carbonate Leaching

In uranium mining and milling, bicarbonate and carbonate extractions are applied to alkali soils and rocks where carbonates present in the rock increase the amount of acid required for dissolution to an uneconomical level. Carbonate leaching is also favoured for its high selectivity – acid based extraction creates a mixed effluent with high amounts of other metals including Al, Fe, Ca, Si, from which it can be difficult to separate U and treat the effluent [56]. Due to the low cost and low toxicity of bicarbonate salts, high concentrations may be used to achieve extraction in heavily contaminated soils. U(VI) is extracted as a soluble tricarbonate complex according to the following reaction [49].

$$UO_2^{2+} + 2HCO_3^- + CO_3^{2-} \rightarrow UO_2(CO_3)_3^{4-} + 2H^+$$

In reduced ores, U(IV) must first be oxidised to U(VI) for this extraction to occur. For some U(IV) phases, such as UO_2, extraction can occur directly with molecular oxygen [57]. Alternative oxidants such as $KMnO_4$ or H_2O_2 may also be used [1].

$$UO_2 + ½\ O_2 + 3CO_3^- + H_2O \rightarrow UO_2(CO_3)_3^{4-} + 2OH^-$$

The use of carbonate extraction for soil remediation was piloted at the Fernald site in Ohio, USA, which was the site of a uranium processing plant that has become contaminated from spills and incinerator discharges [57]. A number of studies have detailed potential remediation of the site [49, 56, 57], with a particular focus on carbonate chemical leaching. Uranium speciation at the Fernald site is dominated by low solubility uranyl phosphates such as meta-autunite $Ca(UO_2)_2(PO_4)_2.xH_2O$ [57], with uraninite (UO_2) also present. The application of carbonate leaching has been demonstrated to successfully extract around 80% U from Fernald soils, enhanced by the application of an oxidising agent such as $KMnO_4$ to increase U(IV) dissolution [56, 57].

Bicarbonate extraction was also studied in lab scale batch tests for DU contamination at US military sites [49, 58]. The maximum bicarbonate extraction efficiency was found to vary widely between the different sites, from 25% to > 90%, likely reflecting differences in total soil contamination and speciation between samples. In some soils, enhanced extraction was observed with the addition of H_2O_2, which accelerates the oxidation and dissolution of U(IV) phases (e.g. UO_2) commonly associated with DU impact residues.

These studies demonstrate that oxidative carbonate extraction can remove low solubility uranium phases from heterogeneously contaminated soil matrices. As demonstrated in studies of Fernald soil contamination [57], for better application to DU contaminated soils there is a need to link the speciation of U with the extraction efficiency, in order to understand and overcome limiting effects, such as the presence of carbonate-insoluble U phases.

2.2.4.2 Citrate Leaching

Citric acid (2-hydroxypropane-1,2,3-tricarboxylic acid) is a weak organic acid that has been studied for U extraction as the citrate anion forms stable complexes with U(VI) [56, 58-60]. As for carbonate extraction, application of an oxidant is required for U(IV) phases. Citric acid has been identified as particularly suitable for extraction of heavy metal contamination due to low cost, low toxicity, low affinity for alkali earth metals [61] and relative ease of biodegradation versus other organic chelators such as EDTA (Ethylenediaminetetraacetic Acid) [60].

Citric acid extraction has been investigated in comparison to carbonate extraction for U contaminated soils. In the previously discussed studies of Fernald (Ohio, USA) contaminated soils, extraction of U using citrate had a maximum efficiency range from 70% – 100% depending on the soil characteristics [56]. Extraction was observed to be increasingly efficient with lower pH and for pH < 4, the amount of U extracted was independent of citrate concentration. Soil contaminated as a consequence of water soluble uranium interactions was found to have the highest proportion of extractable uranium, whereas lower U extraction efficiencies were measured in soil contaminated with incinerator residues. In these soils uranium metaphosphate ($U(PO_3)_4$) was found to be the main component of U residues

remaining after chemical leaching [56, 57]. These extraction efficiencies compare well with those reported using carbonate and bicarbonate lixivants [56].

Citric acid was also considered as an extractant for DU contamination from a US military firing range [58]. The efficiency of extraction varied depending on the source of the material studied – DU from aged sands was extractable at 50-60%, whereas material more recently contaminated was more resistant to extraction, with around 20-30% achieved. Aged soils would be expected to have greater proportion of U(VI), which is more amenable to extraction in citrate [59]. Experiments on recovery of uranium in citric acid from sands synthetically contaminated with uranyl nitrate solutions ($UO_2(NO_3)_2$) show 98% extraction, demonstrating a high affinity for soluble U(VI) species [59].

The results of these studies suggest that citric acid could be a viable extraction agent for contaminant U from a variety of environmental matrices. In comparative studies [56, 58] citric acid and bicarbonate salts have similar U extraction efficiencies, and are often studied together as low cost, environmentally compatible extraction agents.

2.2.4.3 Mineral Acid Leaching

Mineral acids such as H_2SO_4 and HNO_3 are used in fuel cycle operations to dissolve uranium oxide fuels, as extractants for in-situ leach mining of uranium ores, or as part of acid milling in conventional mining. Mineral acids however present a higher degree of handling risk and environmental hazard than weak organic acids such as citric acid. A number of comparative studies favour carbonate or citrate extraction over strong mineral acids due to comparable extraction efficiencies and lower extents of soil matrix alteration [48, 56, 60]. In some cases it was observed that the most effective strong mineral acid leaching solutions have severe detrimental effects on the soil character that may outweigh benefits of remediation [48].

2.3 Chromium Contamination

2.3.1 Chromium in the Environment

Chromium (Z = 22) is a transition metal used in a wide variety of industrial processes including stainless steel manufacture, leather tanning and chrome plating. This widespread industrial use has resulted in the release of large quantities of chromium compounds to the environment, which is of concern as chromium can be highly toxic and carcinogenic, posing direct threats to human health and environmental quality [62].

In nature, chromium is redistributed in soils and waters by weathering of parent mineral phases, with typical natural concentration ranges of 0.02 to 58 μmol/g in soils [63] and 0.5–100 nM in freshwater systems [62]. Chromium can exhibit a wide range of oxidation states from -2 to +6, with only the trivalent and hexavalent states of importance under natural ranges of redox potential and pH [63]. In natural waters, trivalent chromium readily undergoes hydrolysis to form insoluble oxyhydroxides [64] and interacts strongly with mineral surfaces [63, 65], both of which reduce its mobility in the environment.

Cr(III) is readily oxidised to Cr(VI) in oxic conditions and in the presence of oxidising soil components such a manganese dioxide [62]. Hexavalent chromium is present in waters as the chromate (CrO_4^{2-}) oxyanion. In contrast to Cr(III), oxyanionic Cr(VI) is highly mobile in the environment, as the lower charge density results in weaker interaction with mineral surfaces and a lesser tendency to form insoluble hydrolysis products [66]. In natural systems, the Cr(III)/Cr(VI) ratio is dependent on a variety of factors including photochemical and chemical redox processes, presence of competing species and interaction with sorbing mineral phases [62].

The differences in Cr(III) and Cr(VI) aqueous chemistry are reflected in different biological properties. Trivalent chromium is an essential nutrient for animals and plants, and is involved in a number of important biological mechanisms including glucose metabolism and amino and nucleic acid synthesis [63, 67]. In contrast hexavalent chromium is highly toxic and

carcinogenic as it a strong oxidant [68]. Chromate is readily taken into cells by sulphate (SO_4^{2-}) transport mechanisms owing to similarities in the charge and structure, making aqueous Cr(VI) highly bioavailable [68].

2.3.2 Remediation of Hexavalent Chromium Contamination

The combination of high toxicity, bioavailabity and environmental mobility make Cr(VI) an extremely hazardous contaminant. The release of Cr(VI) by industrial processes and waste materials poses a serious threat to the environment and human health, and many instances of chromate contamination require intervention to reduce this hazard. The introduction of strict regulation for Cr(VI) levels in industrial discharges (e.g. < 0.05 mg/L, US EPA [69]) has led to increasing interest in the removal of Cr(VI) from industrial effluents, in addition to the development of environmental remediation technologies to reduce the risks posed by high levels of Cr(VI) from legacy contamination [69].

Current industrial practice for removal of Cr(VI) uses physiochemical processing, as chromate toxicity generally prevents the deployment of biological methods [69]. The reduction of Cr(VI) to Cr(III) is an important reaction to control the risk associated with chromium contamination as Cr(III) exhibits lower environmental mobility, toxicity and bioavailabity than Cr(VI). Most industrial effluent treatment processes target this reaction – the most commonly used approaches are precipitation technologies, which employ reduction of Cr(VI) to Cr(III) at low pH, followed by an increase in pH to precipitate $Cr(OH)_3$, which is then disposed of as a sludge [70]. Where it is desirable to recover chromium, evaporation may be used to concentrate Cr in a small volume and permit return of the evaporated stream to the environment [69, 70]. Other non-reductive approaches include flotation, for example with hydrocalcite as a collector [71], and electrolysis, which is particularly employed to treat and recycle chromium in electroplating effluents [70].

Remedation of chromium contaminated waters in the environment exploits the same physical principles, particularly reduction and precipitation, but requires a different method of implementation from industrial wastewater treatment. Both ex-situ and in-situ processes are

employed, with in-situ methods typically requiring less environmental disturbance and operational cost, and ex-situ treatment offering greater control over process parameters [72]. The selection of technology requires an understanding of the site characteristics, concentration of the target contaminant and any co-contaminant species, and the required end state for the remediated site [72].

The most widely employed technologies at full scale include solidification, electrokinetic remediation, and in-situ chemical extraction [72]. For Cr(VI), solidification employs reduction to insoluble Cr(III) compounds, typically with Fe(0)/Fe(II) species [66]. Alternative reductants have been trialled, including mineral surface catalysed reduction by low molecular weight organic molecules [73] and reaction with hydrogen sulphide [74]. Electrokinetic remediation is widely used the U.S.A. to remediate Cr(VI), by encouraging controlled contaminant migration and subsequent collection using low current electrodes. In-situ extraction is a means to selectively mobilise and collect Cr(VI) in a liquid phase for disposal, thereby removing it from the environment [72].

In the case of legacy contamination, transport of species from a pollutant source forms a plume in the water flow direction, which once located may require treatment. A common method to remediate contaminant plumes is the insertion of a reactive barrier downstream from the source [75]. In the case of Cr(VI) contamination, the reactive barrier is designed to reduce Cr(VI) to Cr(III), which due to the lower solubility of Cr(III) compounds, has the effect of removing chromium from the water. In some cases, direct removal of chromium from heavily contaminated soils has been considered in the form of heap leaching Cr from contaminated soils, removing the point source of chromium and thereby preventing its long term release into the environment [53]. However, in the case of existing chromium contaminant plumes or areas where soil treatment is impractical, there is still a requirement to prevent Cr(VI) migration, and the development of effective reactive barriers is an important research goal.

2.3.3 Reduction of Cr(VI) by Magnetite

The development of reactive materials from chromium reduction has received much attention. In particular, reduced Fe species such as zerovalent Fe [76], green rust (an Fe corrosion product with ideal formula $[Fe(II)_4Fe(III)_2(OH)^{12}][CO_3]\cdot 3H_2O$) [77] and magnetite $[Fe(II)Fe(III)_2O_4]$ [78] have received significant attention as reductants for Cr(VI). Magnetite has been of special interest as it is a common mineral present in the geosphere and at some sites may act as a natural reductant for Cr(VI) [79, 80], providing native attenuation in the mobility of contaminant chromium. Magnetite can also be produced by dissimilatory iron reducing bacteria (DIRB) [81], which has been suggested as a potential facile low temperature route to engineered or in-situ production [82, 83]. Biogenic magnetite is nanoscale (particle size is 20-30 nm [84]), which provides a large surface area for remediation. Sub-stoichiometric magnetite with a higher Fe(II)/Fe(III) ratio can also be produced by tuning the conditions under which microorganisms precipitate the mineral, increasing the reductive reactivity [85]. Comparative studies demonstrate the enhanced reactivity of biogenic over synthetic magnetite [83, 85], highlighting that potentially simpler synthesis of magnetite by microorganisms is accompanied by improvements in the performance of the material for Cr(VI) reduction.

Magnetite adopts the cubic spinel structure ($A^{2+}B^{3+}{}_2O_4$), which is flexible for the incorporation of other bivalent, trivalent and quadravalent anions. Incorporation of Cr(III) into the structure of biogenic magnetite has been demonstrated to occur during Cr(VI) reduction [82]. This has important implications for remediation, as incorporated Cr may be expected to exhibit greater stability with respect to reoxidation than a surface precipitate of $Cr(OH)_3$ [87].

The ability of magnetite produced by microorganisms to effectively reduce Cr(VI) has been demonstrated in a number of studies [66, 82, 83, 85, 88]. These small scale demonstrations typically employ idealised conditions, without the presence of other redox active contaminants and in narrow pH ranges. It has been demonstrated for natural magnetites that at high pH, mineral transformations and passivation of the surface reduce their reactivity for chromate reduction [79, 84]. Studies of zero-valent iron demonstrate that reduction of Cr(VI) is impaired

against a background of other anions and redox active contaminants, particularly in the presence of nitrate [76]. These studies highlight that the performance of a remediation system needs to be evaluated under field relevant conditions, which is a clear research goal in the further development of biogenic magnetite for Cr(VI) remediation.

Pd functionalised biogenic magnetite has recently been demonstrated as an effective magnetically recoverable heterogeneous catalyst [84]. The use of Pd to catalyse electron transfer to the magnetite support has been hypothesised as a means to extend the reactive capacity of these materials, and investigation of this system forms the basis of chapter 7 of this thesis. In particular, Pd-catalyst systems have shown to be insensitive to nitrate reduction [89, 90], and this system may also provide some resistance to nitrate impairment of mineral reactivity.

2.4 Conclusions

This review has highlighted the potential risks to human health and the environment caused by DU munitions and chromium(VI) contamination. Current research on the remediation of these contaminants has been outlined, and with no mature technology available for flexible and cost-effective hazard reduction in either case, a need to investigate new processes alongside optimisation of currently proposed methodologies was identified.

Residues from DU munitions occur as microparticles (typical d = 1-15μm) in surface soils, which present inhalation hazard and may be readily dispersed in the environment. The properties of these residues have been extensively studied, but there is uncertainty concerning their long term behaviour in the surface environment. Reviewing the literature related to DU particle characterisation revealed that particles deposited into different environments had similar properties, suggesting a degree of stability of these residues over the short timescales between deposition and sampling in these studies. There is a need to investigate this stability over longer periods of time in order to accurately understand the risks posed by DU contamination.

Current best practice for soil DU remediation is disposal of contaminated soil. A number of approaches have been suggested for removing DU residues from soil, of which chemical

extraction using citric acid or bicarbonate salts appear to offer the most promising route for low cost decontamination. There is a need to apply these techniques to additional DU contaminated environments, and in particular to assess the influence of particle weathering on remediation performance.

Chromium (VI) poses severe risks to human health and the environment because of its high mobility, toxicity and carcinogenicity. Remediation of chromium(VI) contamination targets reduction of Cr(VI) to Cr(III), which has low mobility and is non-toxic. Magnetite, an Fe^{2+} bearing mineral, was identified as capable of reducing Cr(VI). This material is particularly attractive because it may be synthesised at the nanoscale by microorganisms, which provide an enhancement to reactivity compared to conventional synthetic magnetite. In common with DU remediation, there is a need to evaluate the performance of biogenic magnetite under a range of conditions to understand interferences which may affect the reactivity and selectivity of magnetite to reduce Cr(VI) under field relevant conditions.

2.5 References

[1] Grenthe, I.; Drozdynski, J.; Fujino, T.; Buck, E. C.; Ablrecht-Schmitt, T. E.; Wolf, S. F., Uranium. In *The Chemistry of the Actinide and Transactinide Elements*, Morss, L. R.; Edelstein, N. M.; Fuger, J., Eds. Springer: 2010; Vol. 1, p 253.

[2] UNSCEAR, United Nations Scientific Committee on the Effects of Atomic Radiation, Sources and Effects of Ionising Radiation, Report to the General Assembly, with scientific annexes; New York 1993.

[3] Bleise, A.; Danesi, P. R.; Burkart, W., Properties, use and health effects of depleted uranium (DU): a general overview. *Journal of Environmental Radioactivity* **2003,** *64*, (2-3), 93-112.

[4] Gavrilescu, M.; Pavel, L. V.; Cretescu, I., Characterization and remediation of soils contaminated with uranium. *Journal of Hazardous Materials* **2009,** *163*, (2-3), 475-510.

[5] Briner, W., The Toxicity of Depleted Uranium. *International Journal of Environmental Research and Public Health* **2010,** *7*, (1), 303-313.

[6] Ansoborlo, E.; Prat, O.; Moisy, P.; Den Auwer, C.; Guilbaud, P.; Carriere, M.; Gouget, B.; Duffield, J.; Doizi, D.; Vercouter, T.; Moulin, C.; Moulin, V., Actinide speciation in relation to biological processes. *Biochimie* **2006,** *88*, (11), 1605-1618.

[7] Borch, T.; Kretzschmar, R.; Kappler, A.; Cappellen, P. V.; Ginder-Vogel, M.; Voegelin, A.; Campbell, K., Biogeochemical Redox Processes and their Impact on Contaminant Dynamics. *Environ. Sci. Technol.* **2009,** *44*, (1), 15-23.

[8] Choppin, G. R.; Stout, B. E., Actinide behaviour in natural waters. *Science of the Total Environment* **1989,** *83*, (3), 203-216.

[9] Elless, M. P.; Lee, S. Y., Uranium Solubility of Carbonate-Rich Uranium-Contaminated Soils. *Water, Air, & Soil Pollution* **1998,** *107*, (1-4), 147-162.

[10] Moyes, L. N.; Parkman, R. H.; Charnock, J. M.; Vaughan, D. J.; Livens, F. R.; Hughes, C. R.; Braithwaite, A., Uranium uptake from aqueous solution by interaction with goethite, lepidocrocite, muscovite, and mackinawite: An X-ray absorption spectroscopy study. *Environ. Sci. Technol.* **2000,** *34*, (6), 1062-1068.

[11] Betti, M., Civil use of depleted uranium. *Journal of Environmental Radioactivity* **2003,** *64*, (2-3), 113-119.

[12] de Haag, P.; Smetsers, R.; Witlox, H. W. M.; Krus, H. W.; Eisenga, A. H. M., Evaluating the risk from depleted uranium after the Boeing 747-258F crash in Amsterdam, 1992. *Journal of Hazardous Materials* **2000,** *76*, (1), 39-58.

[13] Parrish, R. R.; Horstwood, M.; Arnason, J. G.; Chenery, S.; Brewer, T.; Lloyd, N. S.; Carpenter, D. O., Depleted uranium contamination by inhalation exposure and its detection after similar to 20 years: Implications for human health assessment. *Science of the Total Environment* **2008,** *390*, (1), 58-68.

[14] The Royal Society, The health hazards of depleted uranium munitons - Part 1: Policy Document 6/01, **2002**.

[15] Sajih, M.; Livens, F. R.; Alvarez, R.; Morgan, M., Physicochemical characterisation of depleted uranium (DU) particles at a UK firing test range. *Sci Total Environ* **2010,** *408*, (23), 5990-6.

[16] Oliver, I. W.; Graham, M. C.; MacKenzie, A. B.; Ellam, R. M.; Farmer, J. G., Assessing depleted uranium (DU) contamination of soil, plants and earthworms at UK weapons testing sites. *Journal of Environmental Monitoring* **2007,** *9*, (7), 740-748.

[17] Larson, S.; Ballard, J.; Medina, V.; Thompson, M.; O'Connor, G.; Griggs, C.; Nestler, C. Separation of Depleted Uranium From Soil; *Engineer Research and Development Centre, Vicksburg MS Environmental Labs*: **2009**.

[18] Krupka, K. M.; Parkhurst, M. A.; Gold, K.; Arey, B. W.; Jenson, E. D.; Guilmette, R. A., Physicochemical characterization of capstone depleted uranium aerosols III: morphologic and chemical oxide analyses. *Health Phys*. **2009**, *96* (3), 276-291.

[19] Mellini, M.; Riccobono, F., Chemical and mineralogical transformations caused by weathering in anti-tank DU penetrators ("the silver bullets") discharged during the Kosovo war. *Chemosphere* **2005,** *60*, (9), 1246-1252.

[20] Handley-Sidhu, S.; Keith-Roach, M. J.; Lloyd, J. R.; Vaughan, D. J., A review of the environmental corrosion, fate and bioavailability of munitions grade depleted uranium. *Sci Total Environ* **2010,** *408*, (23), 5690-700.

[21] Salbu, B.; Janssens, K.; Lind, O. C.; Proost, K.; Gijsels, L.; Danesi, P. R., Oxidation states of uranium in depleted uranium particles from Kuwait. *Journal of Environmental Radioactivity* **2005,** *78*, (2), 125-135.

[22] Bem, H.; Bou-Rabee, F., Environmental and health consequences of depleted uranium use in the 1991 Gulf War. *Environment International* **2004,** *30*, (1), 123-134.

[23] Cheng, Y. S.; Kenoyer, J. L.; Guilmette, R. A.; Parkhurst, M. A., Physicochemical characterization of capstone depleted uranium aerosols II: particle size distributions as a function of time. *Health Phys*. **2009**, *96* (3), 266-275.

[24] Papastefanou, C., Depleted Uranium in Military Conflicts and the Impact on the Environment. *Health Physics* **2002,** *83*, (2), 280-282.

[25] Harley, N.; Foulkes, E.; Hilborne, L. H.; Hudson, A.; Anthony, C. R.; A Review of the Scientific Literature As It Pertains to Gulf War Illnesses: Volume 7: Depleted Uranium. In Calif: RAND Corporation: **1999**.

[26] Briner, W. E., The evolution of depleted uranium as an environmental risk factor: lessons froms other metals. *Int J Environ Res Public Health* **2006,** *3*, (2), 129-35.

[27] Handley-Sidhu, S.; Bryan, N. D.; Worsfold, P. J.; Vaughan, D. J.; Livens, F. R.; Keith-Roach, M. J., Corrosion and transport of depleted uranium in sand-rich environments. *Chemosphere* **2009,** *77*, (10), 1434-1439.

[28] Handley-Sidhu, S.; Worsfold, P. J.; Boothman, C.; Lloyd, J. R.; Alvarez, R.; Livens, F. R.; Vaughan, D. J.; Keith-Roach, M. J., Corrosion and Fate of Depleted Uranium Penetrators under Progressively Anaerobic Conditions in Estuarine Sediment. *Environmental Science & Technology* **2008,** *43*, (2), 350-355.

[29] Vaughan, D. J.; Alvarez, R.; Bryan, N. D.; Fomina, M.; Gadd, G. M.; Handley-Sidhu, S.; Keith-Roach, M. J.; Livens, F. R.; Lloyd, J. R., Uranium stability in near-surface environments: Lessons from the study of depleted uranium munitions. *Geochim. Cosmochim. Acta* **2009,** *73*, (13), A1375-A1375.

[30] Alvarez, R.; Livens, F. R.; Lloyd, J. R.; Holt, J. P.; Boothman, C.; Wincott, P.; Handley-Sidhu, S.; Keith-Roach, M.; Vaughan, D. J., Geochemical and Microbial Controls of the Decomposition of Depleted Uranium in the Environment: Experimental Studies using Soil Microorganisms. *Geomicrobiology Journal* **2011,** *28*, (5-6), 457-470.

[31] Danesi, P. R.; Markowicz, A.; Chinea-Cano, E.; Burkart, W.; Salbu, B.; Donohue, D.; Ruedenauer, F.; Hedberg, M.; Vogt, S.; Zahradnik, P.; Ciurapinski, A., Depleted uranium particles in selected Kosovo samples. *Journal of Environmental Radioactivity* **2003,** *64*, (2-3), 143-154.

[32] Lind, O. C.; Salbu, B.; Skipperud, L.; Janssens, K.; Jaroszewicz, J.; De Nolf, W., Solid state speciation and potential bioavailability of depleted uranium particles from Kosovo and Kuwait. *Journal of Environmental Radioactivity* **2009,** *100*, (4), 301-307.

[33] Salbu, B.; Janssens, K.; Lind, O. C.; Proost, K.; Danesi, P. R., Oxidation states of uranium in DU particles from Kosovo. *Journal of Environmental Radioactivity* **2003,** *64*, (2-3), 167-173.

[34] Torok, S.; Osan, J.; Vincze, L.; Kurunczi, S.; Tamborini, G.; Betti, M., Characterization and speciation of depleted uranium in individual soil particles using microanalytical methods. *Spectrochimica Acta Part B-Atomic Spectroscopy* **2004,** *59*, (5), 689-699.

[35] Mitchel, R. E. J.; Sunder, S., Depleted uranium dust from fired munitions: Physical, chemical and biological properties. *Health Physics* **2004,** *87*, (1), 57-67.

[36] Chazel, V.; Gerasimo, P.; Dabouis, V.; Laroche, P.; Paquet, F., Characterisation and dissolution of depleted uranium aerosols produced during impacts of kinetic energy penetrators against a tank. *Radiat. Prot. Dosim.* **2003,** *105*, (1-4), 163-166.

[37] Lloyd, N. S.; Mosselmans, J. F. W.; Parrish, R. R.; Chenery, S. R. N.; Hainsworth, S. V.; Kemp, S. J., The morphologies and compositions of depleted uranium particles from an environmental case-study. *Mineral. Mag.* **2009,** *73*, (3), 495-510.

[38] Martz, J. C.; Haschke, J. M., A mechanism for combustive heating and explosive dispersal of plutonium. *J. Alloy. Compd.* **1998,** *266*, (1-2), 90-103.

[39] Akerblom, G., Depleted uranium - Experience of the united nations environmental programme missions. *Natural Radiation Environment* **2008,** *1034*, 69-77.

[40] Grenthe, I.; Drożdżyński, J.; Fujino, T.; Buck, E.; Albrecht-Schmitt, T.; Wolf, S., Uranium. In *The Chemistry of the Actinide and Transactinide Elements*, Morss, L.; Edelstein, N.; Fuger, J., Eds. Springer Netherlands: **2011**; pp 253-698.

[41] Lloyd, N. S.; Chenery, S. R. N.; Parrish, R. R., The distribution of depleted uranium contamination in Colonie, NY, USA. *Science of the Total Environment* **2009,** *408*, (2), 397-407.

[42] Craft, E. S.; Abu-Qare, A. W.; Flaherty, M. M.; Garofolo, M. C.; Rincavage, H. L.; Abou-Donia, M. B., Depleted and natural uranium: chemistry and toxicological effects. *Journal of Toxicology and Environmental Health-Part B-Critical Reviews* **2004,** *7*, (4), 297-317.

[43] Priest, N. D., Toxicity of depleted uranium. *The Lancet* **2001,** *357*, (9252), 244-246.

[44] Durakovic, A.; Horan, P.; Dietz, L. A.; Zimmerman, I., Estimate of the time zero lung burden of depleted uranium in Persian Gulf War Veterans by the 24-hour urinary excretion and exponential decay analysis. *Military Medicine* **2003,** *168*, (8), 600-605.

[45] Gavrilescu, M., Emerging processes for soil and groundwater cleanup – potential benefits and risks. *Environmental Engineering and Management Journal* **2009,** *8*, (5), 1293-1307.

[46] Fanizza, M. F.; Yoon, H.; Zhang, C.; Oostrom, M.; Wietsma, T. W.; Hess, N. J.; Bowden, M. E.; Strathmann, T. J.; Finneran, K. T.; Werth, C. J., Pore-scale evaluation of uranyl phosphate precipitation in a model groundwater system. *Water Resources Research* **2013,** *49*, (2), 874-890.

[47] Di Lella, L. A.; Nannoni, F.; Protano, G.; Riccobono, F., Uranium contents and U-235/U-238 atom ratios in soil and earthworms in western Kosovo after the 1999 war. *Science of the Total Environment* **2005,** *337*, (1-3), 109-118.

[48] Duff, M. C.; Mason, C. F. V.; Hunter, D. B., Comparison of acid and base leach for the removal of uranium from contaminated soil and catch-box media. *Canadian Journal of Soil Science* **1998,** *78*, (4), 675-683.

[49] Mason, C. F. V.; Turney, W.; Thomson, B. M.; Lu, N.; Longmire, P. A.; ChisholmBrause, C. J., Carbonate leaching of uranium from contaminated soils. *Environmental Science & Technology* **1997,** *31*, (10), 2707-2711.

[50] Farr, C. P.; Alecksen, T. J.; Heronimus, R. S.; Simonds, M. H.; Farrar, D. R.; Miller, M. L.; Baker, K. R., Recovery of Depleted Uranium Fragments from Soil. *Health Physics* **2010,** *98*, (2), S6-S11

[51] Miller, M.; Galloway, B.; VanDerpoel, G.; Johnson, E.; Copland, J.; Salazar, M., An Alternative for Cost-Effective Remediation of Depleted Uranium (DU) at Certain Environmental Restoration Sites. *Health Physics* **2000,** *78*, S9-S12.

[52] Dermont, G.; Bergeron, M.; Richer-Lafleche, M.; Mercier, G., Remediation of metal-contaminated urban soil using flotation technique. *Science of the Total Environment* **2010,** *408*, (5), 1199-1211.

[53] Hanson, A. T.; Dwyer, B.; Samani, Z. A.; York, D., Remediation of chromium-containg soils by heap leaching – column study. *Journal of Environmental Engineering-Asce* **1993,** *119*, (5), 825-841.

[54] Bouffard, S. C.; Dixon, D. G., Investigative study into the hydrodynamics of heap leaching processes. *Metallurgical and Materials Transactions B-Process Metallurgy and Materials Processing Science* **2001,** *32*, (5), 763-776.

[55] Bouffard, S. C.; West-Sells, P. G., Hydrodynamic behavior of heap leach piles: Influence of testing scale and material properties. *Hydrometallurgy* **2009,** *98*, (1-2), 136-142.

[56] Francis, C. W.; Timpson, M. E.; Wilson, J. H., Bench- and pilot-scale studies relating to the removal of uranium from uranium-contaminated soils using carbonate and citrate lixiviants. *Journal of Hazardous Materials* **1999,** *66*, (1-2), 67-87.

[57] Buck, E. C.; Brown, N. R.; Dietz, N. L., Contaminant uranium phases and leaching at the Fernald site in Ohio. *Environmental Science & Technology* **1996,** *30*, (1), 81-88.

[58] Choy, C. C.; Korfiatis, G. P.; Meng, X. G., Removal of depleted uranium from contaminated soils. *Journal of Hazardous Materials* **2006,** *136*, (1), 53-60.

[59] Kantar, C.; Honeyman, B. D., Citric acid enhanced remediation of soils contaminated with uranium by soil flushing and soil washing. *Journal of Environmental Engineering-Asce* **2006,** *132*, (2), 247-255.

[60] Francis, A. J.; Dodge, C. J., Remediation of soils and wastes contaminated with uranium and toxic metals. *Environmental Science & Technology* **1998,** *32*, (24), 3993-3998.

[61] Lenhart, J. J.; Cabaniss, S. E.; MacCarthy, P.; Honeyman, B. D., Uranium(VI) complexation with citric, humic and fulvic acids. *Radiochimica Acta* **2000,** *88*, (6), 345-353.

[62] Kotaś, J.; Stasicka, Z., Chromium occurrence in the environment and methods of its speciation. *Environmental Pollution* **2000,** *107*, (3), 263-283.

[63] Richard, F. C.; Bourg, A. C. M., Aqueous geochemistry of chromium - a review. *Water Res.* **1991,** *25*, (7), 807-816.

[64] Rai, D.; Sass, B. M.; Moore, D. A., Chromium(III) hydrolysis constants and solubility of chromium(III) hydroxide. *Inorganic Chemistry* **1987,** *26*, (3), 345-349.

[65] Dreiss, S. J., Chromium Migration Through Sludge-Treated Soils. *Ground Water* **1986,** *24*, (3), 312-321.

[66] Fendorf, S.; Wielinga, B. W.; Hansel, C. M., Chromium transformations in natural environments: The role of biological and abiological processes in chromium(VI) reduction. *Int. Geol. Rev.* **2000,** *42*, (8), 691-701.

[67] Lytle, C. M.; Lytle, F. W.; Yang, N.; Qian, J.-H.; Hansen, D.; Zayed, A.; Terry, N., Reduction of Cr(VI) to Cr(III) by Wetland Plants: Potential for In Situ Heavy Metal Detoxification. *Environmental Science & Technology* **1998,** *32*, (20), 3087-3093.

[68] Costa, M.; Klein, C. B., Toxicity and carcinogenicity of chromium compounds in humans. *Crit. Rev. Toxicol.* **2006,** *36*, (2), 155-163.

[69] Malaviya, P. Singh, A.; Physicochemical technologies for remediation of chromium-containing waters and wastewaters. *Critical Reviews in Environmental Science and Technology* **2001**, 41, 1111-1172.

[70] Agrawal, A., Kumar, V., Pandey, B. D.; Remediation options for the treatment of electroplating and leather tanning effluent containing chromium – a review. *Mineral Processing and Extractive Metall. Rev.* **2006**, 27, 99-130.

[71] Lazaridis, N. K., Matis, K. A., Webb, M.; Flotation of metal-loaded clay anion exchangers. Part 1: The case of chromate. *Chemosphere*, **2001**, 42, 373-378

[72] Mulligan, C.N., Yong, R.N., Gibbs, B. F.; Remediation technologies for metal-contaminated soils and groundwater: an evaluation. *Engineering Geology* **2001**, 60, 193-207.

[73] Deng, B.; Stone, A. T., Surface-Catalyzed Chromium(VI) Reduction: Reactivity Comparisons of Different Organic Reductants and Different Oxide Surfaces. *Environmental Science & Technology* **1996,** *30*, (8), 2484-2494.

[74] Kim, C.; Zhou, Q.; Deng, B.; Thornton, E. C.; Xu, H., Chromium(VI) Reduction by Hydrogen Sulfide in Aqueous Media: Stoichiometry and Kinetics. *Environmental Science & Technology* **2001,** *35*, (11), 2219-2225.

[75] Blowes, D. W.; Ptacek, C. J.; Jambor, J. L., In-Situ Remediation of Cr(VI)-Contaminated Groundwater Using Permeable Reactive Walls: Laboratory Studies. *Environmental Science & Technology* **1997,** *31*, (12), 3348-3357.

[76] Rivero-Huguet, M.; Marshall, W. D., Impact of various inorganic oxyanions on the removal rates of hexavalent chromium mediated by zero-valent iron. *Environ. Chem.* **2010,** *7*, (3), 250-258.

[77] Williams, A. G. B.; Scherer, M. M., Kinetics of Cr(VI) reduction by carbonate green rust. *Environmental Science & Technology* **2001,** *35*, (17), 3488-3494.

[78] Peterson, M. L.; Brown, G. E.; Parks, G. A., Direct XAFS evidence for heterogeneous redox reaction at the aqueous chromium/magnetite interface. *Colloids Surf., A* **1996,** *107*, 77-88.

[79] He, Y. T.; Traina, S. J., Cr(VI) reduction and immobilization by magnetite under alkaline pH conditions: The role of passivation. *Environ. Sci. Technol.* **2005,** *39*, (12), 4499-4504.

[80] Lee, W.; Batchelor, B., Reductive capacity of natural reductants. *Environmental Science & Technology* **2002,** *37*, (3), 535-541.

[81] Lovley, D. R.; Phillips, E. J. P., Availability of ferric iron for microbial reduction in bottom sediments of the fresh-water tidal potomac river. *Appl. Environ. Microbiol.* **1986,** *52*, (4), 751-757.

[82] Telling, N. D.; Coker, V. S.; Cutting, R. S.; van der Laan, G.; Pearce, C. I.; Pattrick, R. A. D.; Arenholz, E.; Lloyd, J. R., Remediation of Cr(VI) by biogenic magnetic nanoparticles: An x-ray magnetic circular dichroism study. *Appl. Phys. Lett.* **2009,** *95*, (16), 163701.

[83] Cutting, R. S.; Coker, V. S.; Telling, N. D.; Kimber, R. L.; Pearce, C. I.; Ellis, B. L.; Lawson, R. S.; der Laan, G. V.; Pattrick, R. A. D.; Vaughan, D. J.; Arenholz, E.; Lloyd, J. R., Optimizing Cr(VI) and Tc(VII) remediation through nanoscale biomineral engineering. *Environmental Science & Technology* **2010,** *44*, (7), 2577-2584.

[84] Coker, V. S.; Bennett, J. A.; Telling, N. D.; Henkel, T.; Charnock, J. M.; van der Laan, G.; Pattrick, R. A. D.; Pearce, C. I.; Cutting, R. S.; Shannon, I. J.; Wood, J.; Arenholz, E.; Lyon, I. C.; Lloyd, J. R., Microbial Engineering of Nanoheterostructures: Biological Synthesis of a Magnetically Recoverable Palladium Nanocatalyst. *ACS Nano* **2010,** *4*, (5), 2577-2584.

[85] Cutting, R. S.; Coker, V. S.; Fellowes, J. W.; Lloyd, J. R.; Vaughan, D. J., Mineralogical and morphological constraints on the reduction of Fe(III) minerals by Geobacter sulfurreducens. *Geochim. Cosmochim. Acta* **2009,** *73*, (14), 4004-4022.

[86] Jung, Y.; Choi, J.; Lee, W., Spectroscopic investigation of magnetite surface for the reduction of hexavalent chromium. *Chemosphere* **2007,** *68*, (10), 1968-1975.

[87] Ngomsik, A.-F.; Bee, A.; Draye, M.; Cote, G.; Cabuil, V., Magnetic nano- and microparticles for metal removal and environmental applications: a review. *C. R. Chim.* **2005,** *8*, (6-7), 963-970.

[88] He, Y. T.; Traina, S. J., Transformation of magnetite to goethite under alkaline pH conditions. *Clay Miner.* **2007,** *42*, (1), 13-19.

[89] Soares, O.; Órfão, J.; Pereira, M., Activated Carbon Supported Metal Catalysts for Nitrate and Nitrite Reduction in Water. *Catal. Lett.* **2008,** *126*, (3), 253-260.

[90] Prüsse, U.; Hähnlein, M.; Daum, J.; Vorlop, K.-D., Improving the catalytic nitrate reduction. *Catal. Today* **2000,** *55*, (1-2), 79-90.

Chapter 3

Experimental Techniques

3.0 Introduction

This chapter describes the experimental techniques used, with a brief justification and theoretical background where appropriate. Specifics of experimental procedures are described in detail in subsequent results chapters.

The first sections of this chapter (3.1 – 3.5) detail methods and techniques relevant to depleted uranium munitions characterisation and remediation, with a separate discussion of the techniques relating to chromate remediation by magnetite included in section 3.6. Particular focus is given to X-ray chemical imaging techniques (3.4.6 and 3.4.7) which in this project were applied for the first time to U speciation in environmental samples, and this methodology is explained in detail.

3.1 Fieldwork – Eskmeals firing range

3.1.1 Site Description and History

The Eskmeals firing range in Cumbria, UK was used for testing of depleted uranium munitions on armoured targets from the early 1960s to 1995, with the most intense research programme during the 1980s [1, 2]. DU was fired at a single range, named the VJ facility. It is estimated that around 15 tonnes of 120 mm DU rounds were fired at the Eskmeals site during the period 1981 – 1995 [3]. Due to the potential for contamination from DU fragments and aerosols, a 3 hectare area around the VJ facility was designated as a controlled radiation area. Depth profiles of uranium concentration show above-background levels (> 4 mg/kg) to a depth of around 20 cm in areas close to the impact site [4], consistent with the deposition of airborne aerosols to the top layers of soil. Eskmeals soil is classified as raw dune sand, with ~2% organic matter and a variable soil pH in the range 5.6 – 7.8 [2]. Limited DU incorporation into plant matter is

evident, with a maximum plant concentration of 0.05 times the soil concentration [2], suggesting low bioavailability of DU at the site.

3.1.2 Soil Sampling Procedure

Samples of soils from within the VJ radiation control area at Eskmeals were collected in November 2011. Sampling was conducted in three areas (Figure 3.1); Site 1 is a storage area for contaminated timbers used in the construction of targets, Site 2 is adjacent to a concrete apron area downwind from the target, and Site 3 comprises a spoil heap of disturbed sub-soil from post-operational construction at the site. In all cases surface vegetation was removed and soil to a depth of 0.15 m from an area of approximately 0.05 m^2 (total soil volume ~3 L) was sampled into plastic bags, which were sealed for transfer to the laboratory. All samples were air dried at 40 °C and sieved to remove particles above 2 mm. The remaining soil was homogenised by hand, divided into representative portions using the cone and quarter method, and dry stored in sealed containers under ambient conditions.

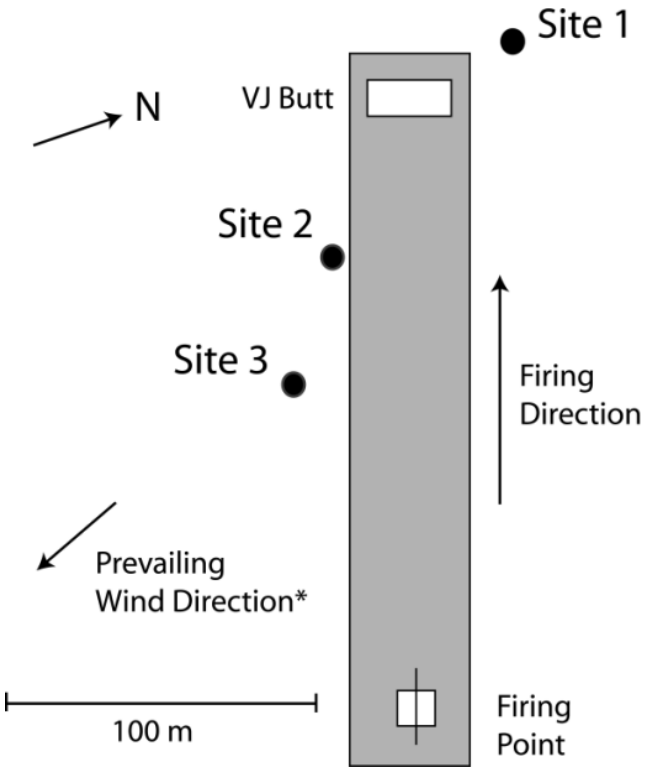

Figure 3.1 – Schematic of sampling locations within the VJ facility at MOD Eskmeals. *Prevailing wind direction adapted from Oliver *et al*. [2]. Reproduced from Chapter 6 [5].

3.2 Bulk Soil Analytical Techniques

3.2.1 Total Uranium

Soil uranium concentrations were determined by exposing 1 g of dried soil to 10 ml 8M Nitric acid at 80°C for 4 hours, heating the solution to dryness and repeating. Attack by nitric acid has been shown previously to completely dissolve DU munitions residues [6, 7]. After the second nitric acid exposure a 1 ml aliquot of the solution was analysed by ICP-AES for U concentration (section 3.2.4).

3.2.2 Sequential Extraction

Sequential extraction techniques are commonly used to define the bulk speciation of metals in terms of extraction into different classes of reagent [8, 9]. Using selective reagents in a progressively more aggressive extraction scheme provides a means to assess partitioning of a metal between different chemical constituents of a soil.

The extent of fractionation between different extraction reagents is operationally defined, and to introduce some extent of comparability between the work of different laboratories, standard procedures for sequential extraction are used, typically the BCR [8] or Tessier [9] schemes. In this thesis, the BCR scheme was used as it has previously applied to U speciation in soils [2, 10]. The BCR extraction scheme defines exchangeable, reducible and oxidisable soil fractions, which are described in Table 3.1. Although not included in the BCR scheme, a residual fraction is usually evaluated by digestion of the soil in mineral acids, allowing for a mass balance to be calculated [4]. Here the residual step was identical to the procedure used for determining total U concentration (section 3.2.1). Following each step, an aliquot of the extraction reagent was analysed by ICP-AES for U concentration (section 3.2.4).

Despite their utility as simple and rapid tools for generating quantitative data on the partitioning of an element into soil speciation fractions, the use of sequential extraction techniques has been criticised [11]. The main criticism is selectivity - there may be interferences between steps in a scheme, and chemical species with otherwise divergent properties may be solubilised to similar

extents [11, 12]. The validity of interpreting extraction under artificial conditions with respect to environmental properties of interest such as bioavailability has also been questioned [11]. It is important to take care over the interpretation of data and support the use of sequential extraction methods with other complementary techniques. Combination of sequential extraction with appropriate microanalysis can provide a means to understand detailed speciation and quantitatively assess the fractionation of an element between different chemical states [13].

Table 3.1 – Schematic of typical sequential extraction scheme steps and reagents. At each stage, the concentration of the element of interest in the extract is measured by a suitable analytical technique – in this project ICP-AES was used to analyse uranium concentration.

Step	Soil Fraction	Reagents and Conditions (BCR scheme [8])
Exchangeable	Ion-exchangeable and carbonate bound	Acetic Acid 0.11 mol/l
Reducible	Bound to reducible Fe or Mn species	Acidified 0.1 mol/l $NH_2OH{\cdot}HCl$
Oxidisable	Bound to organic matter or sulphur species	Twice extracted with 30% w/v H_2O_2 at room temperature and 85°C, residue extracted in 1 mol/l ammonium acetate.
Residual	Bound in recalcitrant species, crystalline Fe oxides and silicates.	Not defined by BCR, typically by total digestion in mineral acids including HF.

3.2.3 Storage Phosphor Autoradiography

Storage phosphor autoradiography was used to image the spatial distribution of radioactivity corresponding to the presence of DU particles in soil samples, both to localise DU particles for analysis and as a non-destructive measure of the total soil radioactivity [14]. In general, phosphor storage autoradiography is insensitive to alpha radiation, and for depleted uranium beta and gamma emissions from the immediate short lived ^{238}U daughter products ^{234}Th and

$^{234(m)}$Pa produce the image. Due to their very short half-lives compared to ^{238}U, these nuclides reach the same activity as the parent at around 200 days after purification of U [15].

3.2.4 Determination of liquid phase U concentration in soil extract supernatants

The concentration of uranium in extraction solutions was measured by inductively coupled plasma atomic emission spectroscopy (ICP-AES). This technique allows simultaneous multi element measurement of metal concentrations in a sample by exciting atoms in plasma and measuring the emitted characteristic radiation. The detection limit for U using ICP-AES can be as low as 10 ppb [16], but is dependent on the sample matrix.

The instrument used in this work was a Perkin-Elmer Optima 5300 dual view ICP-AES, operated by P. Lythgoe at the University of Manchester. Uranium calibration standards of 0.1 ppm, 0.5 ppm, 1 ppm and 10 ppm U were prepared by dilution of a 1000 ppm standard solution (Sigma Aldrich, UK). For remediation extractions, matrix matched standards in each of the extractant solutions were prepared to check for interferences on the measured concentration.

3.3 Particle Analysis Techniques

3.3.1 Particle Isolation by Autoradiography

To isolate particles for analysis, dried and homogenised soil was spread thinly (~1 mg sample/cm^2) on a grid with 1 cm^2 squares and exposed to a phosphor autoradiography imaging plate [6]. Material in grid squares which showed the presence of a particle was sampled onto adhesive carbon pads by pressing the pad onto the grid square.

3.3.2 Scanning Electron Microscopy (SEM) and Energy Dispersive X-ray Spectroscopy (EDX)

Scanning electron microscopy was used to study the morphology, composition and microstructure of depleted uranium particles, using an FEI XL30 Environmental SEM (ESEM) operated in high vacuum mode. In this configuration, the ESEM operates similarly to a conventional SEM instrument. The microscope uses a field emission gun electron source with

detectors for backscattered electrons, secondary electrons and energy dispersive X-ray (EDX) spectroscopy.

SEM requires high vacuum conditions to prevent scattering and absorption of electrons in air. Samples are also required to be conductive to prevent charging of the surface by the beam, which is usually achieved by coating with carbon or gold. If particles are sufficiently small, charging can be avoided by mounting the sample on a conductive adhesive pad, typically composed of carbon. This approach was taken to avoid destructive sample preparation which may alter surface features.

Backscattered electron imaging was used as this mode provides atomic number (Z) contrast, allowing U particles (Z = 92) to be clearly discriminated from environmental matrix particles which contain mainly O (Z = 8), Si (Z = 14) and Fe (Z = 26) [6]. In this imaging mode, high Z elements appear brightly due to backscattering of the primary beam by the higher number of electrons in atoms of these elements. Particles which appear brightly in this mode were analysed for elemental composition to confirm the presence of U by energy dispersive X-ray spectroscopy.

Energy dispersive X-ray spectroscopy measures elemental composition by analysis of characteristic X-rays emitted when core level electrons of atoms in the sample are ejected by interaction with the electron beam. The energy of emitted X-rays is characteristic of the elements present, which allows identification of the composition samples. Quantitative compositional information can be obtained by control of the sample geometry and reference to a standard with appropriate corrections. In this project, EDX was used semi-quantitatively to characterise elemental composition and confirm the presence of uranium in particles of interest.

3.4 Synchrotron X-ray Chemical Microscopy

3.4.1 Introduction

The interaction of X-rays with matter can give a wide variety of chemical information on a sample. The energy of X-rays encompasses the binding energy of core-level electrons, which

allows for investigation of chemical state and composition, and because X-rays have wavelength similar to the interatomic spacing in solids, diffraction measurements can be performed to establish the atomic structure of crystalline materials.

The use of microfocus X-ray optics makes it possible to probe chemical information in very small volumes of samples down to a typical minimum 1 μm^2 minimum spot size using X-ray mirror microfocussing [17]. With a motorized sample stage it is possible to spatially resolve this chemical information by moving different regions of interest into the beam. This setup also allows the sample to be rastered (i.e. moved stepwise) in the beam to construct a map of information, an approach which is referred to as X-ray chemical microscopy.

In this project, both single point measurements of small domains and spatially resolved X-ray chemical imaging approaches were used. Three distinct analyses were used - X-ray fluorescence microscopy to image elemental distributions, X-ray diffraction microscopy to resolve microscale phase distributions, and X-ray absorption spectroscopy microscopy to probe the oxidation state of uranium.

3.4.2 Synchrotron X-rays

3.4.2.1 Generation of Synchrotron X-rays

Synchrotron radiation is generated by the acceleration of charged particles travelling at relativistic velocities along a curved trajectory. In a synchrotron light source, this radiation is produced by high energy electrons circulating in a storage ring. In the ring a beam of electrons travels in segments of straight line connected by bending magnets which deflect the beam onto the next section of the ring. At each of these bending magnets, synchrotron radiation is emitted, which exits the storage ring along a beam-line to an experimental station. The energy of this radiation spans the microwave to hard X-ray range.

Insertion devices, such as wigglers and undulators can be placed in straight sections of the storage ring as additional point sources synchrotron radiation. These devices can also provide greater control over the brightness of radiation emitted at specific energies, and as such can be

optimised for individual experimental requirements [18]. The beamline used in this project was XL05A at the Swiss Light Source (Figure 3.2), which uses an insertion device source [17].

3.4.2.2 X-ray Microfocus Optics

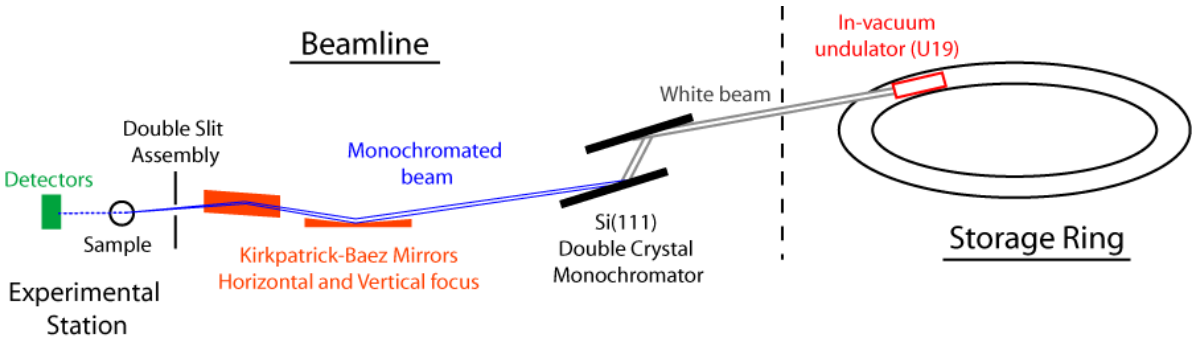

Figure 3.2 – Simplified schematic layout of microfocus X-ray beamline XL05A at the Swiss Light Source. The photon energy is selected by means of a double crystal monochromator, and focused to size using mirrors in Kirkpatrick-Baez arrangement. The size of the beam can also be further controlled using an end station slit assembly.

Broadband 'white light' radiation is emitted by bending magnets and insertion devices, containing photons with a range of energies. Due to the high intensity of synchrotron sources, it is possible to isolate a single energy by means of a monochromator whilst retaining sufficient flux to perform experiments at acceptable levels of signal-noise ratio and counting time. For X-rays, a double crystal monochromator is used, typically designed with Si crystals oriented to the beam along the (111) or (311) axes, although Ge (111) designs are also used. When the polychromatic beam strikes the monochromator crystals inclined at a specific angle relative to the beam, a single wavelength is selected which satisfies the Bragg condition, $2d\sin\theta = n\lambda$, where θ is the angle of diffraction, λ is the photon wavelength, d is monochromator crystal interplanar spacing and n is an integer. As d is fixed, changes in the orientation of the crystal can be used to select a different photon wavelength to be diffracted from the monochromator, giving a mechanism to tune the energy of the monochromatic beam delivered to the experimental station.

The monochromatic beam is focused by X-ray mirrors, and microfocus beamlines usually employ Kirkpatrick-Baez geometry, whereby pairs of long flat mirrors are used to achieve independent horizontal and vertical focus [19]. X-ray mirrors are made from flat, extremely smooth plates to totally externally reflect the X-ray beam [18]. XL05A uses Rh plated mirrors to achieve microfocussing of the X-ray beam down to a minimum spot size of 1.3 μm (H) x 0.9 μm (V) [17]. In the optical path, additional mirrors are used for preliminary focussing, as a low pass energy filter and for harmonic rejection to remove higher order multiples of the desired photon energy which can also satisfy the Bragg condition of the monochromator.

3.4.3 X-ray Analytical Techniques

3.4.3.1 X-ray Fluorescence

X-ray fluorescence (XRF) is a technique used for quantitative and qualitative analysis of elemental composition. The basic physical principle is identical to visible light fluorescence, but involves the ejection of core level electrons with high binding energies from the inner orbitals of the atom due to the higher energy of X-ray photons (~100 eV – 100 keV). On absorption of an X-ray photon with energy greater than its binding energy, a core electron is ejected from the atom leaving an unstable hole in an inner orbital. This is subsequently filled by transition of an electron from a higher energy orbital in the atom and the energy released in this transition is emitted as a second X-ray photon. The atoms of each element have characteristic energy levels in which electrons can reside, and transition between these states, and the energy difference emitted as fluorescent photons, is distinct for atoms of different elements.

Identification of elements by measuring characteristic X-ray fluorescence emissions is the basis of X-ray fluorescence spectroscopy. The number of characteristic photons emitted by a sample is proportional to the number of atoms of that element present, and XRF can be used to quantitatively measure elemental composition. As X-rays are penetrating, XRF can be a non-destructive probe. However, quantitative data must be corrected for processes which reduce the yield of photons arriving at a detector, such as scattering in air, reabsorption and scattering by the sample, and the efficiency of the detector. Quantitative XRF usually requires idealised

geometry and specialist instruments employing vacuum conditions to preserve the validity of these corrections. In this project, XRF spectroscopy is used as a semi-quantitative tool for measuring elemental composition and approximate relative amounts of elements present in a sample.

3.4.3.2 X-ray Diffraction (XRD)

X-ray diffraction was used to identify crystalline phases in the sample. As the wavelength of X-rays is similar in magnitude to interatomic spacing in solids (both on the order of 1 Å, 10^{-10} m), interference of scattered X-rays can occur. In crystalline solids, where interatomic spacing is ordered, constructive interference from planes of atoms occurs where the distance between planes (d) is an integral number of X-ray wavelengths (λ), as described by the Bragg equation, $2d\sin\theta = n\lambda$, where θ is the scattering angle. By monitoring X-ray intensity against scattering angle, peaks are observed when the Bragg equation is satisfied for a set of lattice planes at a specific angle, which gives information about the arrangement of atoms in the crystal structure. As this is unique for each crystal compound, XRD can be used to identify unknown phases in a sample by comparison to standard diffraction patterns or a database. Phases were identified in this study with reference to the ICSD-2 powder diffraction file.

3.4.3.3 X-ray Absorption Spectroscopy (XAS)

X-ray absorption (XA) spectroscopy describes a suite of techniques which can provide information on chemical properties such as oxidation state and local co-ordination environment of an element by measuring the energy dependence of X-ray absorption cross-section [20]. As discussed above, core shell electrons have characteristic binding energies and can be ejected from an atom by interaction with a photon of sufficient energy. This gives rise to 'edges' in the absorption of X-rays of different energies (Figure 3.3) - below the characteristic energy the probability of absorption is low, which increases as the X-ray energy increases above the binding energy of a core shell electron, and photons are absorbed with the ejection of a photo-electron. The dependence of absorption on energy near an absorption edge is a complex

function of the chemical environment of the absorbing atom, and information can be extracted by employing an appropriate analysis of the spectrum.

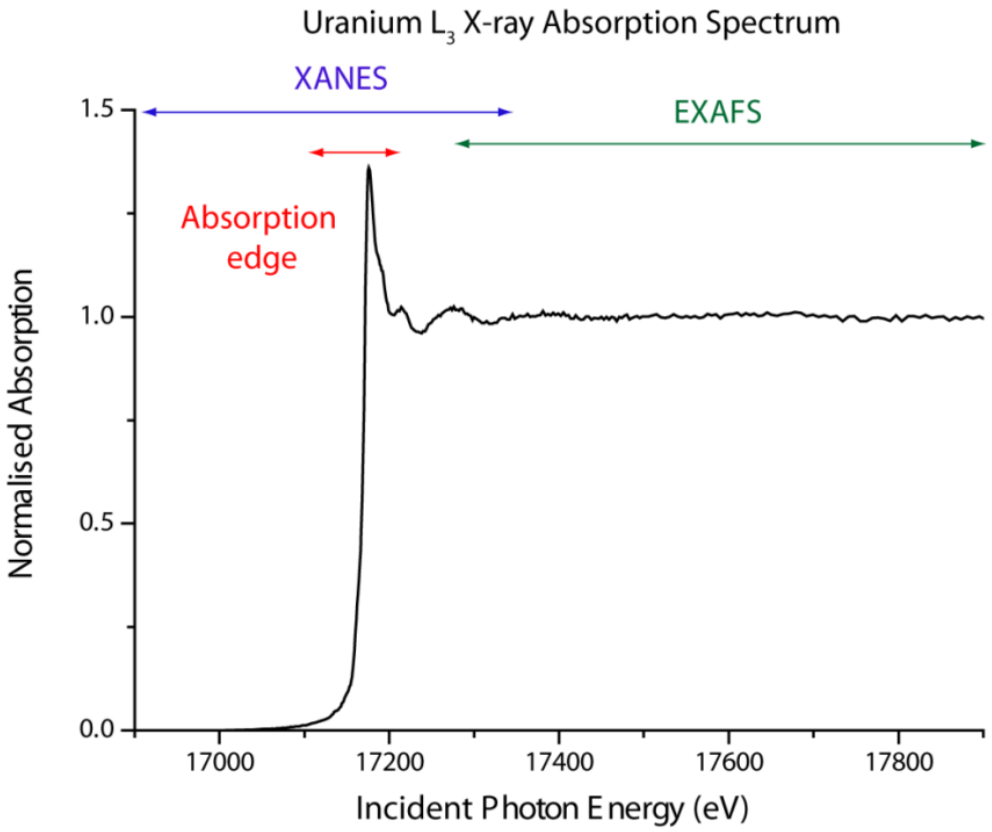

Figure 3.3 – Uranium L_3 XA spectrum illustrating regions of interest for XANES and EXAFS analyses. The rising part of the spectrum is termed the absorption edge, the energy position of which shows strong dependence on the oxidation state of the absorber.

X-ray absorption can be measured in transmission, fluorescence or electron yield geometries [18], and in this project fluorescence geometry was used. The emission of fluorescent X-rays is proportional to the absorption of incident photons, which is measured as a ratio of emitted intensity (I_F) to incident intensity (I_0). The intensity of fluorescence X-rays (I_F) is usually measured with a solid-state detector and the incident flux (I_0) is measured using an ion chamber. Fluorescence geometry is less sensitive than other geometries to sample preparation [21], and can be used on dilute samples. This makes fluorescence XAS common for environmental samples, where the element of interest may be in low concentration with respect to the bulk matrix [20].

3.4.3.4 X-ray Absorption Near Edge Structure Spectroscopy (XANES)

X-ray Absorption Near Edge Structure Spectroscopy (XANES) uses the portion of the spectrum from below the absorption edge to range of around 100 eV after, and can provide information on the oxidation state [18] and local co-ordination geometry [21]. Absorption edge energy (E_0) is directly related to the binding energy of an inner core electron, which varies with the oxidation state of the absorber. As oxidised ions have fewer electrons, the average nuclear charge per electron is increased, resulting in an increase in binding energy [20]. By reference to standards, the relationship between binding energy and oxidation state can be calibrated, allowing accurate determination of oxidation state in unknown samples. The absorption edge shape is related to the density of unoccupied states which the absorbing electron may be promoted to. This can be modulated by hybridisation of unoccupied orbitals according to the co-ordination geometry, and the absorption edge structure is sensitive to these geometry dependent changes in unoccupied states. This allows XANES to be used to quantify the presence of an element in different co-ordination geometries in a sample.

3.4.3.5 Extended X-ray Absorption Fine Structure Spectroscopy (EXAFS) Analyses

Extended X-ray Absorption Fine Structure (EXAFS) analysis uses the spectrum from just above the absorption edge up to ~1000 eV after. This region contains information related to the bonding of the absorbing atom, specifically the types and number of co-ordinating atoms, the interatomic distances and the degree of local disorder [21]. Photoelectrons are emitted as spherical waves with kinetic energy equal to the incident photon energy minus the binding energy. Oscillations in the x-ray absorption with energy are linked to scattering of photoelectrons by atoms coordinated with the absorber, which causes interference of the scattered and outgoing photoelectron waves.

As the incident energy increases, the photoelectron wavelength becomes shorter, and as the interatomic distance does not change, interference between the outgoing and scattered photoelectrons oscillates as a function of the interatomic distance [18, 21]. Photoelectrons may be scattered by a number of atoms in a structure, which is referred to as multiple scattering.

Here the scattering path distance is related to a number of interatomic distances, which can give additional information on the local structure.

These oscillations can be described using the EXAFS equation, which sums over all scattering paths the photoelectron can take. The equation describing the EXAFS component for each path is:

$$\chi_i(k) \equiv \frac{(N_i S_0^2) F_{eff_i}(k)}{kR_i^2} \sin[2kR_i + \varphi_i(k)] e^{-2\sigma_i^2 k^2} e^{\frac{-2R_i}{\lambda(k)}}$$

with $R_i = R_{0i} + \Delta R_i$ and $k^2 = \frac{2m_e(E - E_0 + \Delta E_0)}{\bar{h}}$.

The EXAFS path amplitude χ_i is expressed as a function of the photoelectron wavenumber k, which is a transform of the incident photon energy scale E, using the theoretical edge shift energy (E_0), a fitting parameter to align the experimental and theoretical energy scales (ΔE_0), the electron mass (m_e) and Plank's constant ($\bar{h}$). The term R_i describes the half path length, which for single scattering is the interatomic distance. R_{0i} is a reference value (e.g. crystallographic value) and ΔR_i represents a modification. N_i describes the path degeneracy, which for single scattering is interpreted as the co-ordination number. The parameter σ_i^2 accounts for disorder in interatomic distances as a mean-square displacement. The terms $F_{effi}(k)$, $\varphi_i(k)$ and $\lambda(k)$ represent the effective scattering amplitude, phase shift and mean free path of the photoelectron. In EXAFS analysis, these values are theoretically calculated for each path using codes such as FEFF. The remaining term S_0^2 describes relaxation in the energy of remaining electrons caused by the core hole.

This calculation allows the EXAFS spectrum to be modelled as the combination of different paths with unknown path parameters fitted to the data. As often the objective is to determine information about an unknown structure, terms related to the number of co-ordinating atoms and interatomic distance are fitted to the data, typically ΔR_i, σ_i^2 and N_i. Other parameters that cannot be readily calculated also require fitting, these are S_0^2 and the modifier for absolute edge energy ΔE_0, which aligns the modelled and measured energy spectra. Careful fitting of these

terms allows for the local molecular bonding environment to be reconstructed from the EXAFS spectrum.

3.4.4 Sample Preparation

Synchrotron hard X-ray microanalysis is an attractive technique for the study of environmental particles because it does not require destructive sample preparation techniques and can be performed at ambient temperature and pressure without the need for high vacuum conditions. This means minor features such as delicate surface alteration layers may be retained and minimal artificial alteration to the sample is introduced.

In the first instance, particles were mounted on adhesive carbon pads (Agar, UK) for analysis in the SEM. These were sealed with Kapton tape for containment during transfer to the beamline. During the experimental run some particles were transferred from the carbon pads to the Kapton tape by peeling. These tapes were mounted in a sample holder (Figure 3.4) for analysis in the beam. Remaining particles mounted on the original carbon pad were also analysed.

3.4.5 Experimental Station Setup and Instrumentation

Samples were mounted on a motorised *x*-*y*-*z* stage which was oriented at 25° to the incident beam. A micro ion chamber was used to measure the incident X-ray intensity. All experiments were performed under ambient conditions.

XRF spectra were recorded with an incident X-ray energy above the U L_3 edge (E = 17.300 or 17.500 keV) using a Si(Li) detector (KETEK Instruments) positioned at 90° to the incident beam. XRD data were measured in transmission geometry to allow co-collection with XRF spectra. The detector used was a PILATUS 100K hybrid pixel array detector [22], mounted 46 mm behind the sample with a tungsten beamstop in place to attenuate the primary beam.

X-ray absorption spectroscopy was measured in fluorescence mode as in this setup (Figure 3.4) the XRD instrument occupied the position required for a transmission geometry detector. Both XANES (X-ray Absorption Spectroscopy Near Edge Structure) and EXAFS (Extended X-ray Absorption Fine Structure) analyses were used in this thesis.

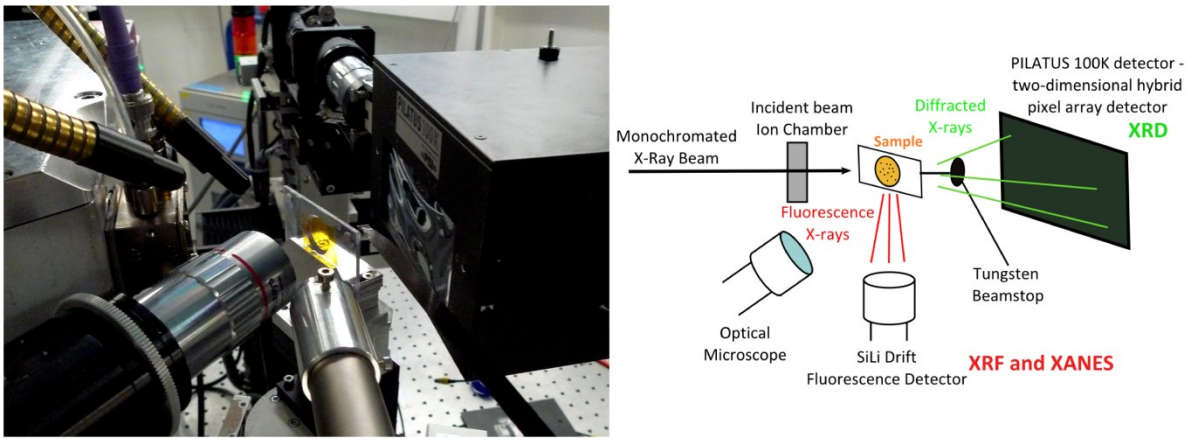

Figure 3.4 – Photograph and schematic of SLS XL05A microXAS beamline instrumentation, showing detectors for fluorescence and diffracted X-rays. The optical microscope is used for localisation and orientation of sample areas.

3.4.6 Mapping

Images of XRF, XRD and XAS data are made by rastering (scanning) the sample through the microfocussed X-ray beam. The resolution is governed by the beam spot size and the scanning step size of the stage when moving the sample. The beam spot size in this study was 2 µm (v) x 5 µm (h). The pixel size is determined by the stage step increment, which was varied depending on the size of the area studied. For XRF and XRD mapping a spectrum and diffraction pattern were recorded at each point and the sample stage is moved to the next position. XAS maps are constructed from XRF maps taken at different energies and were recorded separately as the incident photon energy was varied between scans.

3.4.7 Mapping Data Processing

3.4.7.1 X-ray Fluorescence Imaging

Semi-quantitative images of elemental distribution are constructed from XRF spectra. Regions of interest (ROI) in the XRF spectrum are defined corresponding to the emission energy of elements thought to be present in the sample. The intensity in this region is recorded during scanning of the sample, which produces a per-element map of the sample (Figure 3.5 shows the

process for uranium). These maps were recorded using in-house software at SLS (jFDA) and processed using Matlab to produce heatmap-contrast images of element fluorescence counts.

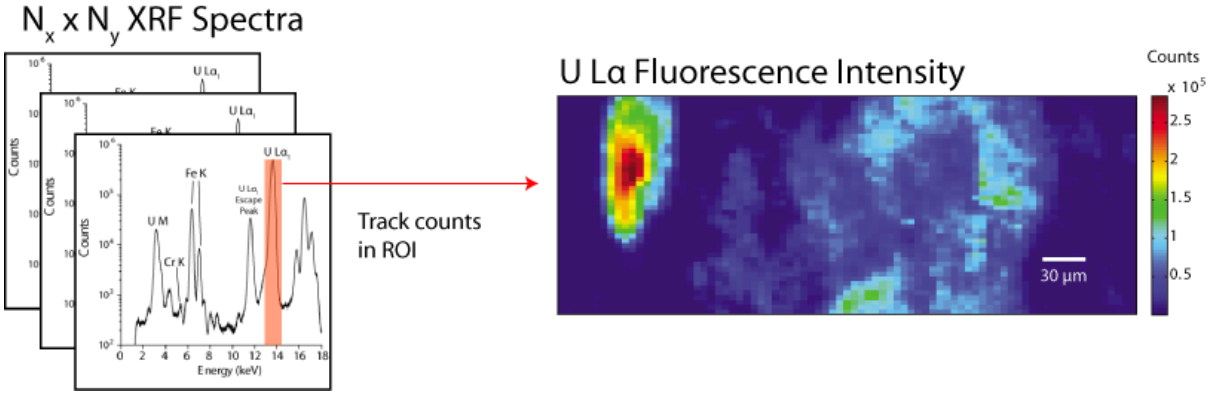

Figure 3.5 – Diagram of X-ray fluorescence imaging processing routine. The intensity of a spectral region of interest corresponding to a characteristic X-ray emission line, in this case UL*α*, is tracked through a series of XRF spectra collected during scanning of the sample in the beam.

3.4.7.2 X-ray Diffraction Imaging

Phase maps of the spatial distribution of crystalline species in the sample were constructed from X-ray diffraction patterns using the software XRDUA [23], and the process is outlined in Figure 3.6. The raw data consists of a large number of 2D diffraction patterns which each correspond to points from scanning the sample (Figure 3.6a). These patterns are superimposed to produce a whole area powder pattern, which allows all phases present in the sample to be indexed and identified (Figure 3.6b). Having identified the phases present, reflections corresponding to species of interest are selected (e.g. Meta-ankoleite (0 0 2) at ~4.5° 2θ, Figure 3.6c) to be mapped by extracting the intensity in this region from the original 2D patterns.

This intensity distribution is constructed into a map using the *x*-*y* co-ordinates of each pattern (Figure 3.6d). These maps for different species can be overlaid as different channels in RGB space to produce a map showing the distribution of several phases as different colours (Figure 3.7)

-

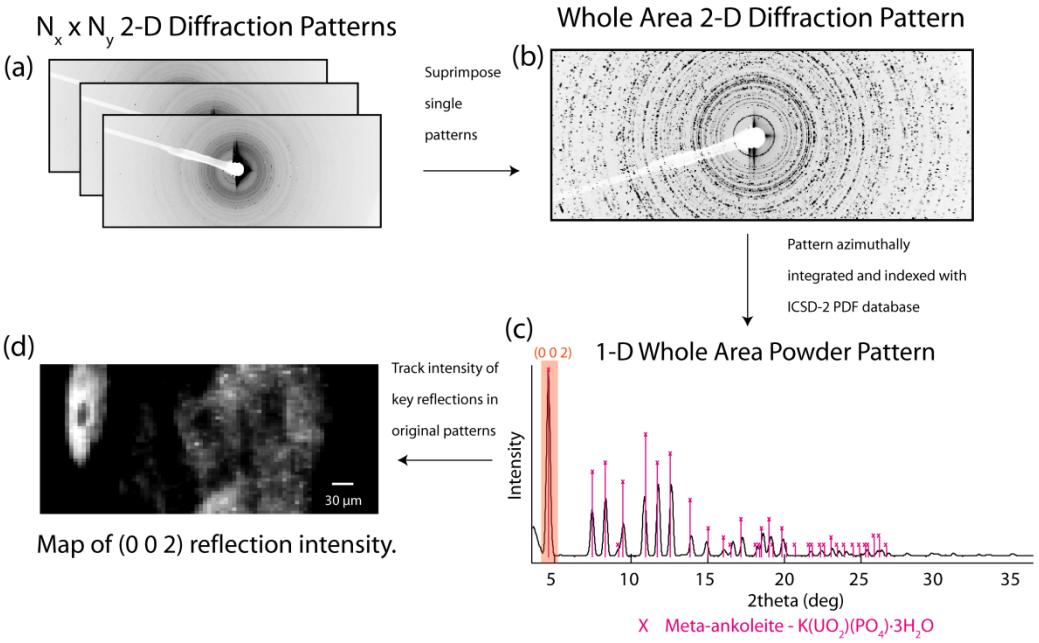

Figure 3.6 - Diagram of the step process for producing phase distribution maps from X-ray diffraction data. Superimposition of component patterns and phase intensity mapping are performed using the software XRDUA. Patterns are indexed in separate software for comparing to ICSD-2 PDF database records.

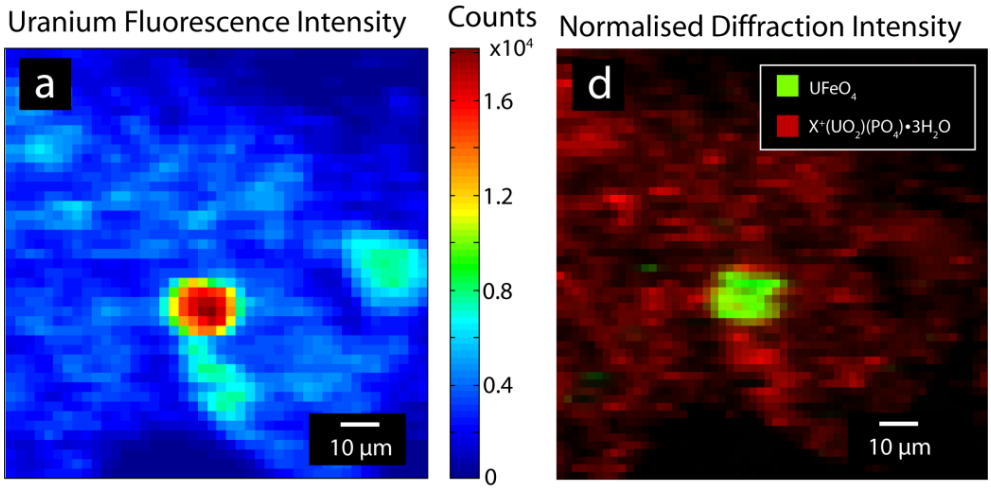

Figure 3.7 – Example phase map showing the distribution of $UFeO_4$ and $X^{+}(UO_2)(PO_4)\cdot 3H_2O$ in a sample alongside µ-XRF map of U L_α intensity. The monochrome maps (Figure 3.6d) of individual phase distributions have been combined. This figure is reproduced from Chapter 5.

3.4.7.3 X-ray Absorption Spectroscopy Imaging

XAS imaging in the XANES region may be used to produce maps of element oxidation state [24, 25] or co-ordination environment. This relies on contrast in X-ray absorption at specific energies corresponding to different chemical states. In the case of uranium, the L_3 edge position moves to higher energy with increasing oxidation state and additional resonances appear in the spectrum related to presence of uranyl (UO_2^{2+}) species, allowing U in different oxidation states to be identified. This results in regions of contrast in the spectrum, where at specific energies there are differences in the X-ray absorption co-efficient μ(E) between oxidation states of U (Figure 3.8).

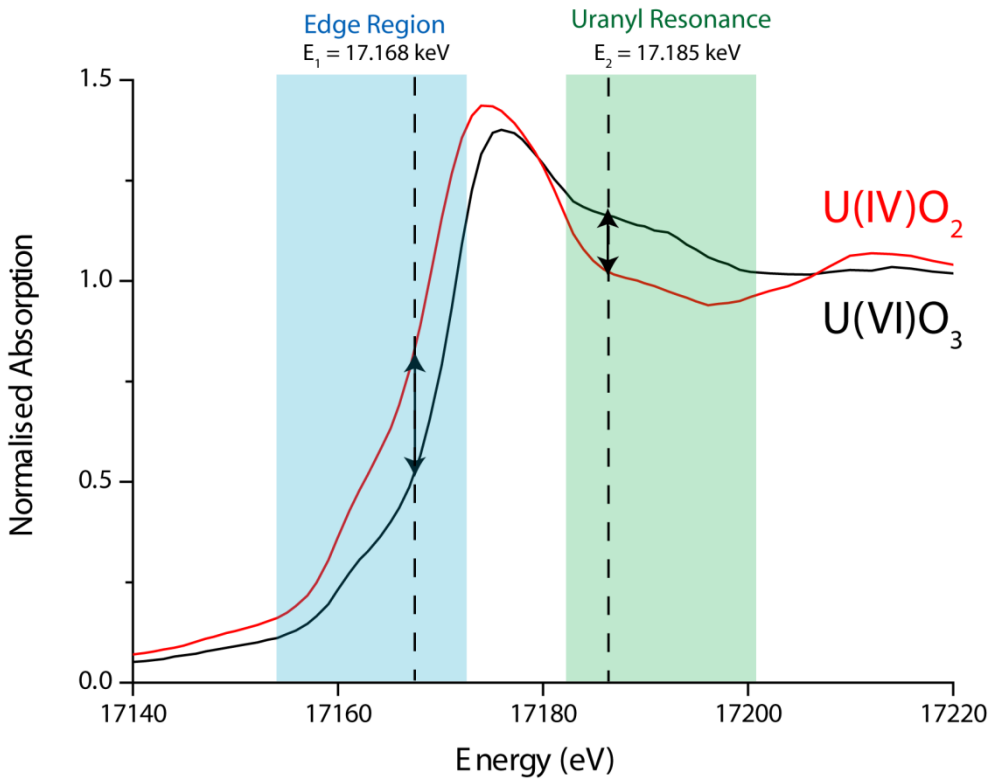

Figure 3.8 – Uranium L_3 XANES spectra showing energies of contrast between U(IV) and U(VI). At energies in the edge region, U(IV) has higher normalised absorption as the edge for this oxidation state occurs at a lower energy. In the uranyl resonance region, U(VI) species have higher absorption due to scattering along the linear uranyl species. These regions of contrast allow oxidation state to be resolved by comparing absorption at a specific energy, such as those marked by a dotted line.

Energies for mapping in both regions of contrast were chosen – E_1 = 17.168 keV corresponds to contrast in the edge region and E_2 = 17.185 keV corresponds to uranyl resonance contrast (Figure 3.8). To map the distribution of uranium oxidation states, XRF maps were measured at each of these energies with the corresponding incident X-ray intensity (I_0) recorded at each pixel point. This is required to convert the fluorescence counts into a measure of absorption, where the absorption co-efficient is proportional to I_f/I_0. Variations in fluorescence intensity (I_f) relating to the concentration distribution of uranium were normalised with reference to an additional fluorescence map recorded at E_n = 17.500 keV. This energy is in the EXAFS region, where absorption shows lower contrast between species of different oxidation state.

Raw fluorescence maps are shown in Figure 3.9. Maps were recorded using in-house JFDA software at the Swiss Light Source and processed in MATLAB. MATLAB provides a convenient environment for the per pixel operations required, e.g. dividing fluorescence intensity maps by corresponding I_0 values, and provides tools for visualising chemical imaging data as 2D heat maps. It is interesting to note that little chemical information is visible in these raw data – the distribution of uranium in all three maps is near identical. This is because contrast in raw fluorescence data is dominated by concentration differences rather than chemical gradients.

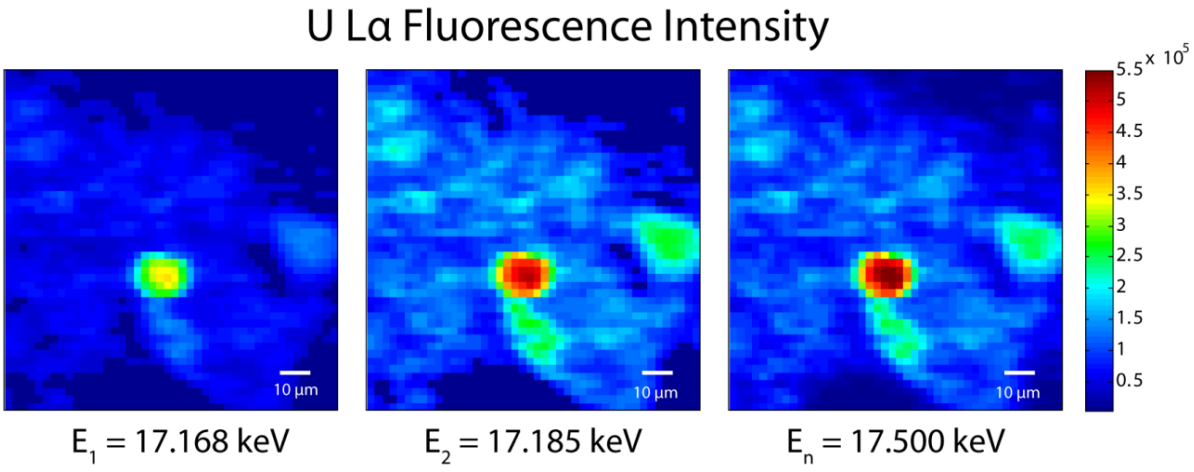

Figure 3.9 – Fluorescence maps used for calculation of U oxidation state. The E_1 map shows lower counts as this is on the rising edge part of the XANES region.

Areas of low counts in XRF maps were set to zero by a thresholding routine. This removes pixels (sets as zero value) for which counts are not sufficiently high enough to permit calculation of the U oxidation state. In conventional terms, this means that XANES spectra from these areas would have levels of noise which introduce unacceptable uncertainty into oxidation state determination. The appropriate threshold is system dependent, and in the fluorescence maps shown in Figure 3.9 set at 3 x 10^4 counts.

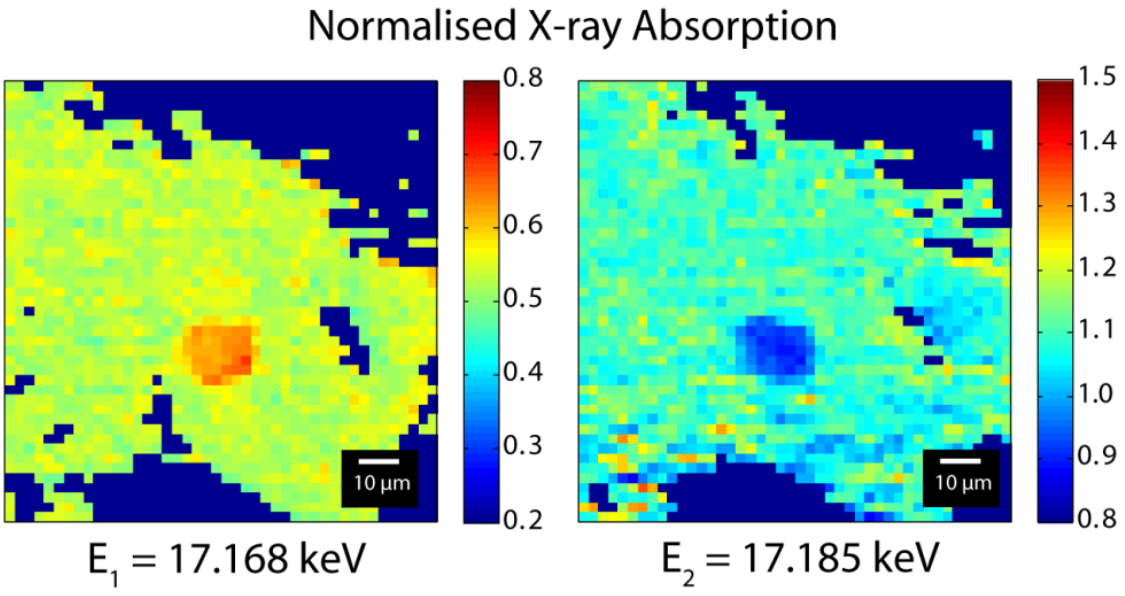

Figure 3.10 – Maps of normalised X-ray absorption at E_1 and E_2, calculated by dividing fluorescence map in Figure 11 by the incident X-ray intensity (I_0) and normalising with respect to X-ray absorption at higher energy, E_n.

Each of the maps was divided through by a corresponding matrix of I_0 values to give maps of X-ray absorption. Absorption maps at E_1 and E_2 were then normalised by dividing each pixel by the corresponding value in the E_n absorption map. Each pixel in the resulting maps (Figure 3.10) is equal to the normalised absorption coefficient at this spatial point, as given by

$$\mu(E_1) = \frac{F(E_1)/I_0(E_1)}{F(E_n)/I_0(E_n)},$$

where $\mu(E_x)$ is the matrix of normalised absorption values at energy *x*, $F(E_x)$ is the matrix of fluorescence values and $I_0(E_x)$ the matrix of incident intensity.

In these data chemical contrast between the central region and the outer rim is clear in both maps. The higher absorption at the edge energy E_1 suggests the central region is reduced with respect to the other area. This is confirmed at E_2 where the inner region has corresponding lower absorption in the post edge region.

The X-ray absorption coefficient may depend on the oxidation state of the absorbing atom, and this can be used to convert the maps in Figure 3.10 directly to maps of U oxidation state. XANES spectra of standards containing uranium in various oxidation states were measured to produce a suitable calibration relationship (Figure 3.11). The trend in absorption with oxidation state at both energies is linear in this region, and interpolation is used to calculate the oxidation state of unknown samples from the measured normalised absorption.

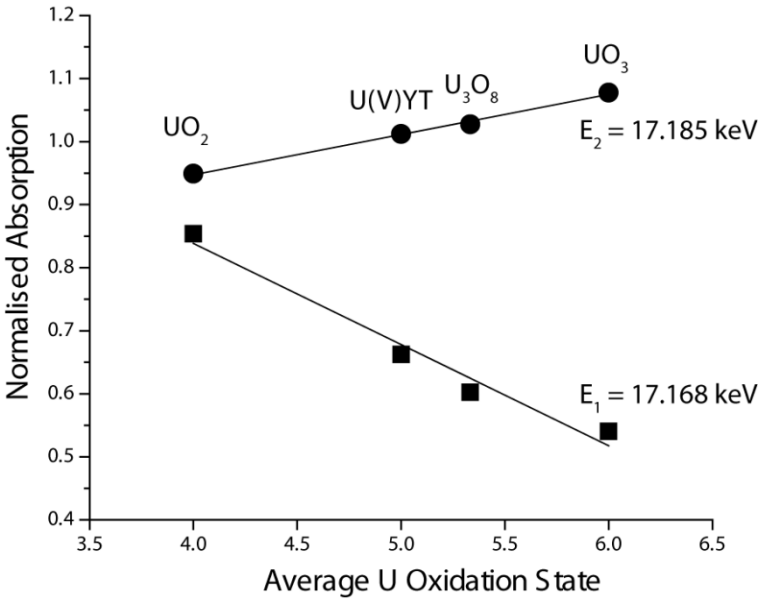

Figure 3.11 – Linear dependence of absorption at E_1 and E_2 on average U oxidation state. Normalised absorption values were extracted from spectra of UO_2, $U_{0.5}Y_{0.5}Ti_2O_6$ (U(V)YT), U_3O_8 and UO_3 standards.

Normalised absorption data in Figure 3.11 are from the average of 4 XANES scans, and the relative standard deviation is small, 0.6% at 17.168 keV. Uncertainty in the determination of oxidation state by μ-XAS mapping is estimated as ± 0.2 by comparison of mapped regions to crystallographic oxidation state and point μ-XANES spectra. This is comparable to the

oxidation state uncertainty in XANES spectroscopy, which is linked to the energy resolution of the scan, and is typically ± 0.1. The calibrated linear relationship between oxidation state and normalised absorption at a particular energy (Figure 3.11) is only applicable for similar classes of compounds, e.g. those in which the absorbing atom has a similar local environment, such as oxygen ligands. In systems where a linear calibration is not appropriate, maps may be taken at a larger number of energies and filtering or fitting of the absorption values at various energies applied to resolve speciation [24].

The converted oxidation state map is shown in Figure 3.12. The contrast observed in Figure 3.10 is revealed as a difference of nearly one oxidation state between the central region (~+5.2) and the rim (+6).

Although this technique has previously been applied to Ce and Fe speciation in glasses and archaeological relics [24, 25], the results presented in Chapters 4 and 5 of this thesis represent the first application of this technique to uranium in environmental samples. For this study, the non-destructive nature of this analysis is key to preserving weathering features and preventing artificial alteration of the sample.

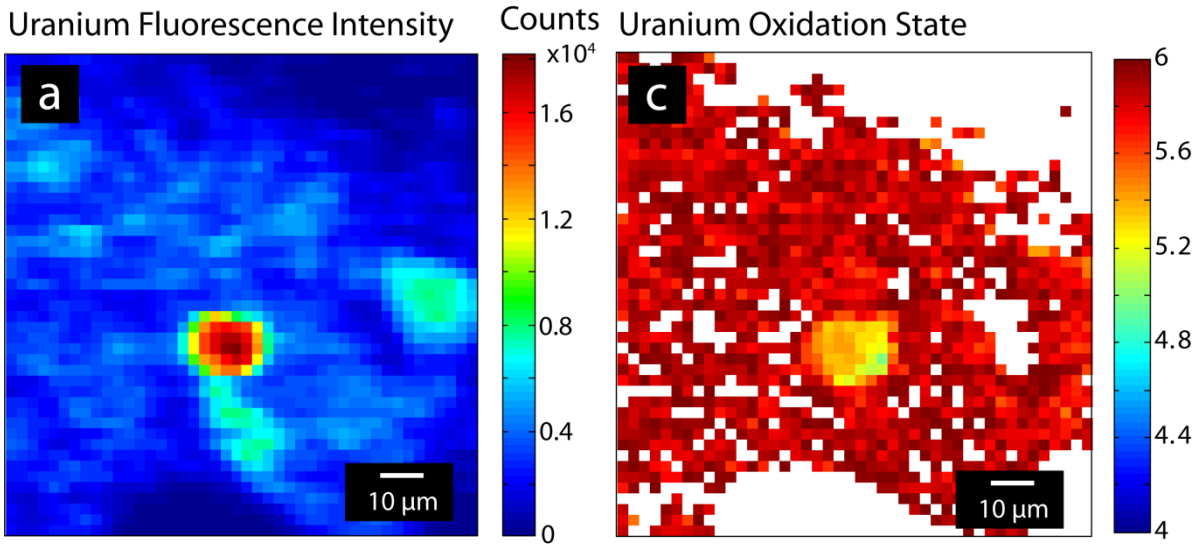

Figure 3.12 – Map of uranium oxidation state calculated from linear dependence of absorption on oxidation state. The corresponding U fluorescence map at E_n is also shown to highlight gradients in U concentration. This figure is taken from chapter 5.

3.5 Remediation of DU Contaminated Soils

3.5.1 - Batch Remediation Experiments

The efficiency of chemical extraction for decontamination of DU contaminated soils was evaluated using batch experiments. 1g of soil was contacted with 10 ml of leaching solution in 50 ml vials with an air headspace. Three lixivants were trialled for U extraction – 0.5M $(NH_4)HCO_3$, 0.1M citric Acid and 0.1M H_2SO_4. This experimental design was chosen for comparison with previous studies of DU decontamination using these extraction agents on other contaminated areas [26, 27]. Decontamination was calculated using two methodologies – bulk soil radioactivity and residual soil digestion.

Bulk soil radioactivity was measured by autoradiography of soil samples before and after extraction. The 1g soil samples were spread thinly on a 6 cm x 7 cm paper (~24 mg soil / cm^2) and exposed to a storage phosphor film for 21 hours. Soil radioactivity was evaluated by summing counts in a region of the digital image corresponding to the soil sample, minus background counts measured in an equivalent area of the film not exposed to the sample. This process was repeated following extraction to determine the total activity removed.

Decontamination efficiency was calculated by mass balance. Following extraction, the supernatant was separated from soil by filtration, acidified and U concentrations analysed by ICP-AES. The residual soil was then digested using the above described procedure for total U concentration (3.2.1). The ratio of mass U extracted to mass U remaining in residue was then calculated.

3.6 Remediation of Cr(VI) by Biogenic Magnetite

3.6.1 Chromate Column Reduction Experiments

Magnetite was produced for column reduction experiments by a biogenic route using late log phase cultures of *Geobacter sulfurreducens* and a ferrihydrite suspension [28]. Ferrihydrite is a hydrous ferric oxide mineral which was synthesised by alkaline hydrolysis of $Fe(III)Cl_3$

solution. Details of this procedure can be found in Chapter 7 and are described by Cutting *et. al* [28, 29]. The biogenic magnetite was produced as a slurry with a concentration of 0.45 mol/l Fe determined by microwave assisted digestion and ICP-AES. Functionalisation of the biogenic magnetite surface was performed by exposure to $NaPdCl_4$ to achieve a 5 wt% loading, as described previously [30].

Column experiments were conducted to test the efficiency of biogenic magnetite as a permeable reactive barrier. A layer of sand was impregnated with 2.5 ml of the magnetite slurry. Potassium chromate solution at 50µM was infiltrated into the columns at a rate of 0.13 cm^3/min. The Cr(VI) concentration in the outlet was determined using spectrophotometrically using the 1,5-diphenylcarbazide (DPC) assay [31], and column experiments halted when the effluent and influent Cr(VI) concentrations were equal. The magnetite layer was then recovered for analysis.

3.6.2 Magnetite Analyses

The characteristic diameter of biogenic magnetite particles is ~20 – 30 nm [30], and different analytical techniques are required to characterise these materials from those employed for DU particles discussed above. One analytical advantage when studying these materials is the use of techniques which would usually be considered surface sensitive, such as X-ray photoelectron spectroscopy (XPS) and total electron yield (TEY) XAS, can be used to provide quantitative information on the total composition as the available probing depth (~10nm for XPS, ~5nm for TEY XAS) encompasses a significant volume of the nanoparticle.

3.6.2.1 X-ray Photoelectron Spectroscopy (XPS)

XPS is a surface sensitive technique to quantitatively probe the chemical properties of a material including elemental composition and chemical speciation. The sample is bombarded with monochromatic X-rays which liberate electrons with binding energies below the incident photon energy. Under ultra-high vacuum (UHV) conditions, these emitted electrons can be collected and the kinetic energy measured. The measured kinetic energy can be related to the binding energy (BE) of the liberated electron, which is characteristic of the element present and its chemical state. Counting the number of electrons collected at different binding energies allows

quantitative information to be obtained on the presence of different elements and their chemical states. To extract this information from spectra of electron binding energies, fitting is performed to quantitatively assign electronic transitions to each of the observed peaks, which as discussed above are linked to the chemical state and elements present. In this thesis, XPS was used to investigate the speciation of Fe, Cr and Pd in reacted magnetites, using a VG Escalab 250 instrument at the University of Leeds, which employs a monochromatic Al *K*α X-ray source.

3.6.2.2 Scanning Transmission Electron Microscopy (STEM)

Transmission electron microscopy (TEM) probes the interactions of electrons which pass through a very thin specimen. TEM uses a higher accelerating voltage than SEM, which affords a higher spatial resolution due to the lower de Broglie wavelength of high energy electrons. In a Scanning TEM, the beam is focussed to a small spot and rastered across the sample using scan coils. This gives high spatial resolution for analytical signals such as X-ray emission (for EDX spectroscopy), allowing the combination of analytical methods available in the SEM with the higher resolution afforded by TEM. In this project, high resolution EDX mapping was used to probe the distribution of Fe, Cr and Pd in functionalised magnetite particles.

Bright field imaging and high angle annular dark field imaging (HAADF) were also used to investigate the magnetite particles. In bright field imaging, the image is composed of the incident beam modulated by interaction with the specimen, and contrast occurs by differences in electron absorption and scattering linked to variable thickness, local atomic number and crystallite orientation. High angle dark field imaging measures electrons scattered by large angles, and provides atomic number (Z) contrast in a similar manner to backscattered electron contrast in the SEM. STEM was performed at the University of Leeds using a FEI Tecnai TF20 instrument. The microscope was operated with an accelerating voltage of 200 kV.

3.6.2.3 X-ray Magnetic Circular Dichroism (XMCD) Spectroscopy

X-ray magnetic circular dichroism is an X-ray absorption (XAS) difference technique which can be used to probe magnetic structure of materials. The term ‘dichroism’ refers to a change in the absorption of photons with different polarisations by a material, and in XMCD this refers to

variations in absorption of left and right circularly polarised incident X-rays by a material in a magnetic field. For transition metals such as Fe, magnetism is linked to the properties of the *3d* electrons, and XMCD is performed at the $L_{2,3}$ edges which probe 2p – 3d transitions. The empty 3d states are strongly polarised and can exhibit a dichroism up to 20% of the total absorption [32].

For magnetite, XMCD is used to probe the abundance of different cations in the spinel structure. In magnetite, Fe^{2+} occupies octahedral sites, and Fe^{3+} is split between tetrahedral and octahedral co-ordination. The influence of the ions in each of these sites on the dichroism spectrum can be calculated by combination fitting with theoretically calculated spectra to resolve each component [33]. This is particularly important for evaluating the reactivity of magnetites, as the amount of structural Fe^{2+} available for reduction can be measured directly.

3.7 References

[1] Carter, T.; M., P.; C., T.; Comparison of Kirkcudbright and Eskmeals Environmental Monitoring Data with Generalised Derived Limits for Uranium, UK Defence Science and Technology Laboratory (DSTL) **2002**.

[2] Oliver, I. W.; Graham, M. C.; MacKenzie, A. B.; Ellam, R. M.; Farmer, J. G., Assessing depleted uranium (DU) contamination of soil, plants and earthworms at UK weapons testing sites. *Journal of Environmental Monitoring* **2007,** *9*, (7), 740-748.

[3] Handley-Sidhu, S.; Keith-Roach, M. J.; Lloyd, J. R.; Vaughan, D. J., A review of the environmental corrosion, fate and bioavailability of munitions grade depleted uranium. *Sci Total Environ* **2010,** *408*, (23), 5690-700.

[4] Oliver, I. W.; Graham, M. C.; MacKenzie, A. B.; Ellam, R. M.; Farmer, J. G., Distribution and partitioning of depleted uranium (DU) in soils at weapons test ranges - Investigations combining the BCR extraction scheme and isotopic analysis. *Chemosphere* **2008,** *72*, (6), 932-939.

[5] Crean, D. E.; Livens, F. R.; Sajih, M.; Stennett, M. C.; Grolimund, D.; Borca, C. N.; Hyatt, N. C., Remediation of soils contaminated with particulate depleted uranium by multi stage chemical extraction. *Journal of Hazardous Materials*, **2013**, In Press.

[6] Sajih, M.; Livens, F. R.; Alvarez, R.; Morgan, M., Physicochemical characterisation of depleted uranium (DU) particles at a UK firing test range. *Sci Total Environ* **2010,** *408*, (23), 5990-6.

[7] Toque, C. C. L.; Baker, A. C. MOD DU Programme - Report on the corrosion of depleted uranium in the Solway Firth, UK Defence Science and Technology Laboratory (DSTL): 8th August, **2005**.

[8] Ure, A. M.; Quevauviller, P.; Muntau, H.; Griepink, B., Speciation of heavy-metals in soils and sediments - an account of the improvement and harmonization of extraction techniques undertaken under the auspices of the BCR of the comission of the European communities. *International Journal of Environmental Analytical Chemistry* **1993,** *51*, (1-4), 135-151.

[9] Tessier, A.; Campbell, P. G. C.; Bisson, M., Sequentual extraction procedure for the speciation of particulate trace-metals. *Analytical Chemistry* **1979,** *51*, (7), 844-851.

[10] Howe, S. E.; Davidson, C. M.; McCartney, M., Determination of uranium concentration and isotopic composition by means of ICP-MS in sequential extracts of sediment from the vicinity of a uranium enrichment plant. *Journal of Analytical Atomic Spectrometry* **2002,** *17*, (5), 497-501.

[11] Nirel, P. M. V.; Morel, F. M. M., Pitfalls of sequential extractions. *Water Research* **1990,** *24*, (8), 1055-1056.

[12] Brittain, S. R.; Cox, A. G.; Tomos, A. D.; Paterson, E.; Siripinyanond, A.; McLeod, C. W., Chemical speciation studies on DU contaminated soils using flow field flow fractionation linked to inductively coupled plasma mass spectrometry (FlFFF-ICP-MS). *Journal of Environmental Monitoring* **2012,** *14*, (3), 782-790.

[13] Hunter, D. B.; Bertsch, P. M., In situ examination of uranium contaminated soil particles by micro-X-ray absorption and micro-fluorescence spectroscopies. *Journal of Radioanalytical and Nuclear Chemistry* **1998,** *234*, (1-2), 237-242.

[14] Kanekal, S.; Sahai, A.; Jones, R. E.; Brown, D., Storage-phoshor autoradiography – A rapid and sensitive method for spatial imaging and quantification of radioisotopes. *Journal of Pharmacological and Toxicological Methods* **1995,** *33*, (3), 171-178.

[15] Szrom, F.; Falo, G. A.; Parkhurst, M. A.; Whicker, J. J.; Alberth, D. P., Calculating Capstone Depleted Uranium aerosol concentrations from beta activity. *Health Physics* **2009,** *96*, (3), 238-250.

[16] Page, A. G.; Gedbole, S. V.; Hadraswala, K. H.; Kulkarni, M. J.; Mallapurkar, V. S.; Joshi, B. D., Determination of Ultra-Trace Amounts of Uranium by ICP-AES Technique. *Analytical Letters* **1983,** *16*, (13), 1005-1012.

[17] Borca, C. N.; Grolimund, D.; Willimann, M.; Meyer, B.; Jefimovs, K.; Vila-Comamala, J.; David, C., The microXAS beamline at the Swiss Light source: towards nano-scale imaging. In *9th International Conference on X-Ray Microscopy*, David, C.; Nolting, F.; Quitmann, C.; Stampanoni, M.; Pfeiffer, F., Eds. **2009**; Vol. 186.

[18] Bunker, G., *Introduction to XAFS*. Cambridge University Press: **2010**.

[19] Kirkpatrick, P.; Baez, A. V., Formation of Optical Images by X-Rays. *J. Opt. Soc. Am.* **1948,** *38*, (9), 766-773.

[20] Penner-Hahn, J. E., 2.13 - X-ray Absorption Spectroscopy. In *Comprehensive Coordination Chemistry II*, Editors-in-Chief: , J. A. M.; Meyer, T. J., Eds. Pergamon: Oxford, **2003**; pp 159-186.

[21] Kelly, S.; Hesterberg, D.; Ravel, B., Analysis of soils and minerals using X-ray absorption spectroscopy. *Methods of soil analysis.* **2008,** *5*, 387-463.

[22] Taguchi, T.; Broennimann, C.; Eikenberry, E. F., Next generation X-ray detectors for in-house XRD. *Powder Diffraction* **2008,** *23*, (2), 101-105.

[23] De Nolf, W.; Janssens, K., Micro X-ray diffraction and fluorescence tomography for the study of multilayered automotive paints. *Surface and Interface Analysis* **2010,** *42*, (5), 411-418.

[24] Grolimund, D.; Senn, M.; Trottmann, M.; Janousch, M.; Bonhoure, I.; Scheidegger, A. M.; Marcus, M., Shedding new light on historical metal samples using micro-focused synchrotron X-ray fluorescence and spectroscopy. *Spectrochimica Acta Part B: Atomic Spectroscopy* **2004,** *59*, (10–11), 1627-1635.

[25] Curti, E.; Grolimund, D.; Borca, C. N., A micro-XAS/XRF and thermodynamic study of CeIII/IV speciation after long-term aqueous alteration of simulated nuclear waste glass: Relevance for predicting Pu behavior? *Applied Geochemistry* **2012,** *27*, (1), 56-63.

[26] Choy, C. C.; Korfiatis, G. P.; Meng, X. G., Removal of depleted uranium from contaminated soils. *Journal of Hazardous Materials* **2006,** *136*, (1), 53-60.

[27] Mason, C. F. V.; Turney, W.; Thomson, B. M.; Lu, N.; Longmire, P. A.; ChisholmBrause, C. J., Carbonate leaching of uranium from contaminated soils. *Environmental Science & Technology* **1997,** *31*, (10), 2707-2711.

[28] Cutting, R. S.; Coker, V. S.; Fellowes, J. W.; Lloyd, J. R.; Vaughan, D. J., Mineralogical and morphological constraints on the reduction of Fe(III) minerals by Geobacter sulfurreducens. *Geochim. Cosmochim. Acta* **2009,** *73*, (14), 4004-4022.

[29] Cutting, R. S.; Coker, V. S.; Telling, N. D.; Kimber, R. L.; Pearce, C. I.; Ellis, B. L.; Lawson, R. S.; der Laan, G. V.; Pattrick, R. A. D.; Vaughan, D. J.; Arenholz, E.; Lloyd, J. R., Optimizing Cr(VI) and Tc(VII) remediation through nanoscale biomineral engineering. *Environmental Science & Technology* **2010,** *44*, (7), 2577-2584.

[30] Coker, V. S.; Bennett, J. A.; Telling, N. D.; Henkel, T.; Charnock, J. M.; van der Laan, G.; Pattrick, R. A. D.; Pearce, C. I.; Cutting, R. S.; Shannon, I. J.; Wood, J.; Arenholz, E.; Lyon, I.

C.; Lloyd, J. R., Microbial Engineering of Nanoheterostructures: Biological Synthesis of a Magnetically Recoverable Palladium Nanocatalyst. *ACS Nano* **2010,** *4*, (5), 2577-2584.

[31] Skougstad, M. W.; Fishman, M. J.; Friedman, L. C.; Erdman, D. E.; Duncan, S. S. *Method for determination of Inorganic Substances in Water and Fluvial Sediments*; U.S. Geological Survey: Washington DC: 1979.

[32] Chen, C. T.; Sette, F.; Ma, Y.; Modesti, S., Soft-x-ray magnetic circular dichroism at the $L_{2,3}$ edges of nickel. *Physical Review B* **1990,** *42*, (11), 7262-7265.

[33] Pattrick, R. A. D.; Van der Laan, G.; Henderson, C. M. B.; Kuiper, P.; Dudzik, E.; Vaughan, D. J., Cation site occupancy in spinel ferrites studied by X-ray magnetic circular dichroism: developing a method for mineralogists. *European Journal of Mineralogy* **2002,** *14*, (6), 1095-1102.

Chapter 4

Micro-analytical X-ray Imaging of Depleted Uranium Speciation in Environmentally Aged Munitions Residues[1]

4.1 Introduction

The testing and use of depleted uranium (DU) armour piercing munitions has caused contamination of soils at a number of sites worldwide [1, 2]. When a DU round strikes a hard target, typically 10 - 35% by mass is converted to fine particles which settle in the environment [3]. Due to high localised concentrations in near-surface environments and potential for resuspension, impact particles are considered a near-term hazard to health and the environment [4].

The physiochemical properties of DU particles have been characterised from a number of sources, including controlled test firing [5, 6], recovery from conflict zone [7-10] and firing range soils [11]. Particles arising from impact with hard targets are typically spherical in morphology with diameter smaller than 15 μm [12], and composed of uranium oxides of varying stoichiometry. The characteristics of field recovered particles are remarkably similar to those from controlled testing, suggesting a degree of environmental stability. DU particles resulting from an ammunition fire [8] and corrosion of metallic penetrators [11, 13] have been characterized as distinct from impact residues, composed of U(VI)-hydrate phases such as schoepite ($UO_3 \cdot 2H_2O$), with sizes up to 1500 μm.

Removal of these particles from soils is challenging [14] and where soil decontamination is impractical the long term environmental behaviour of impact residues will be a key control on

[1]This chapter has been prepared in the form of a manuscript and has been submitted to *Environmental Science and Technology* (September 2013). All research work, manuscript and figure preparation was performed by the author of this thesis. Co-authors Francis Livens and Neil Hyatt are acknowledged for supervision and advisory input to the content and structure of the manuscript, and Martin Stennett, Camelia Borca and Daniel Grolimund for assistance with performing synchrotron microanalysis experiments.

the hazard posed by DU contamination. However, as time between deposition and sampling is short in the majority of field studies [9, 10], there is uncertainty surrounding the evolution of impact particle properties with time in the environment. Variably moist, oxic conditions in the near surface would be expected to promote the oxidation and dissolution of uranium oxides to form mobile U(VI) species [15, 16]. This will change the behaviour of DU in these systems, and there is a lack of information on the behaviour of aged particles in the environment over years to decades.

The Eskmeals firing range (Cumbria, UK) offers an opportunity to study depleted uranium residues that have been exposed to the environment for at least 30 years. Testing at Eskmeals dates from the 1960s [17, 18], predating the first operational use of DU in the 1991 Gulf War. In this study, microfocus synchrotron X-ray analysis by X-ray fluorescence (μ-XRF), X-ray diffraction (μ-XRD) and X-ray absorption spectroscopy (μ-XAS) were used to investigate individual DU particles collected from two geochemically distinct areas at the Eskmeals site. Single point synchrotron X-ray microanalysis has previously been applied to DU particles [7-10], and here we advance on these techniques by employing spatially resolved chemical imaging [19, 20], allowing distinct domains of U speciation within particles to be identified and analysed. Such an approach is warranted both to explore the effects of heterogeneity on particle behaviour, and by the need to study minority species linked to the interaction of particles with the surface environment, for which single point measurement of speciation in particles [7-10] would not be appropriate. Understanding this interaction is critical to predicting and controlling the long term risks posed by surface DU contamination.

4.2 Experimental Methodology

4.2.1 Soil sampling and preparation

Soil containing DU particles was sampled from two locations at the VJ range, Ministry of Defence (MOD) Eskmeals in 2011. Sample point 1 was a burial area for contaminated timber used in target construction, and is located upwind of the target range. Sample point 2 was approximately 40m downwind from the target, in an area similar to that of previous studies [11,

17]. In both cases, surface vegetation was removed and the top 15-20 cm of soil from a 0.05 m^2 area was sampled. Soils were dried at 40°C, sieved to remove particles above 2mm and stored at ambient temperature. DU particles were localised by storage phosphor autoradiography [11], and mounted on carbon pads for analysis.

4.2.2 Scanning electron microscopy with energy dispersive X-ray analysis

SEM and EDX were performed on an FEI XL 30 ESEM with an accelerating voltage of 15 kV. Samples were not coated prior to analysis. The instrument was operated in high vacuum, using backscattered electron (BSE) imaging mode and EDX analysis to localise uranium particles.

4.2.3 μ-XRF, μ-XRD and μ-XANES

Synchrotron radiation microfocus X-ray analyses were conducted on the MicroXAS (X05LA) beamline at the Swiss Light Source, Paul Scherrer Institute, Switzerland [21]. In these experiments, the spot size was approximately 5 μm (h) x 2 μm (v). Samples were mounted on a motorised x-y-z stage which allows scanning in the beam for mapping. The stage was positioned at a 25° angle to the incident beam.

X-ray fluorescence (XRF) was measured using a Si(Li) detector (KETEK) mounted at 45° to the incident beam. 2D X-ray diffraction (XRD) patterns were measured using a PILATUS 100K hybrid pixel array detector [22] mounted 46 mm behind the sample, with a tungsten beamstop in place. Detector tilt and distance to the sample were calibrated by measurement of a silicon standard (NIST 640c), and the angular resolution was approximately 0.1° 2θ. The experimental setup was chosen such that XRF and XRD measurements could be made at the same time, with a monochromatic beam of energy 17.300 keV (λ = 0.71667 Å). XRD patterns were interpreted by matching with standards from the ICSD PDF-2 database.

Uranium L_{III} edge XANES (X-ray Absorption Near Edge Structure) spectra were recorded by monitoring the U Lα fluorescence intensity (13.614 keV) and tuning the photon energy from 16.900 to 17.500 keV, with the incident beam intensity I_0 measured by an ionization chamber. Energy calibration was performed with respect to the K-edge of a yttrium foil (17.038 keV).

Standards of UO_2 (average U oxidation state (OS) 4), $U_{0.5}Y_{0.5}Ti_2O_6$ (average OS 5 [23]), U_3O_8 (average OS 5.33 [24]), UO_3 (average OS 6) were recorded. The edge position was determined as the local maximum in the first derivative of the absorption spectrum, and is a linear function of average oxidation state (Appendix 1 - Figure A1.1) [25]. This relationship was used to determine U oxidation state in unknown samples.

4.2.4 Imaging

By scanning the beam across the sample, maps of XRF and XRD data were constructed. XRF maps were obtained by monitoring specific spectral regions corresponding to emission lines from elements of interest as the sample was rastered in the beam. For crystalline phase distribution (XRD) imaging, powder XRD data were first constructed by summing 2D patterns across a scanned area and applying azimuthal integration to produce a 1-D pattern for phase identification. Phases of interest were then mapped by tracking the intensity of Bragg reflections in the collected patterns across the scanned area using the software XRDUA [19].

X-ray absorption mapping [26] of uranium was performed by U fluorescence mapping at an energy on the absorption edge (17.1677 keV), a post-edge energy which corresponds to a specific UO_2^{2+} resonance (17.195 keV) and normalisation energy (17.5 keV). Maps were thresholded to remove areas of low counts and reduce noise, then normalised with respect to the 17.5 keV map to reveal areas of contrast in normalised X-ray absorption. This is a linear function of the average local oxidation state (Appendix 1 - Figure A1.1), and was used to calculate the average U oxidation state across the imaged area. Redox maps constructed at edge and post-edge energies showed excellent agreement and were averaged.

4.2.5 Soft X-ray Mapping

Beamline instrumentation is sufficient to resolve XRF spectra in the range 4 keV – 17.5 keV and a different system must be used to investigate the distribution of elements with $Z < 22$ (Ti). XRF spectroscopy and mapping for these low-Z elements (Na upwards) were carried out using an Orbis Micro-XRF analyser (EDAX Instruments) operating in low vacuum mode. The

instrument employs a rhodium X-ray tube, which was operated at a voltage of 40 kV and spot size of 30 μm.

4.3 Results and Discussion

4.3.1 'Surface Particles' - Sample Point 2

Due to the position of sample point 2 40m downwind of the target, particles from this sample site comprise settled aerosols and fragments produced on impact of DU with armour plate. This route of formation and deposition in near surface soils is a typical path by which DU impact particulate will enter the environment [2], and particles from this site are discussed first.

4.3.1.1 Morphology

The size and shape of whole particles and U rich regions were examined using backscattered SEM and U X-ray fluorescence imaging. A range of particle types was observed, including characteristic spherical features (Figure 4.1 and Appendix 1- Figure A1.2) which have been linked to the melting of metallic uranium under impact conditions [5]. Many U particles are found clustered together (Appendix 1 - Figure A1.2B and A1.2D), suggesting adhesion to and agglomeration with soil particles and other impact material, which serves to alter the effective particle size of impact residues in soils. The morphology of particles in these soil samples is consistent with other studies of DU impact material including controlled firing tests [5, 6] and particles recovered from conflict zones in the Balkans [8, 9] and Gulf Wars [8].

4.3.1.2 Phase Analysis

Powder diffraction patterns show that uranium in these soils is present mainly as uranium oxides with cubic-derived structures, particularly U_3O_7, with a minor fraction of U_3O_8 in some samples. In the transition between similarly structured UO_2 and U_3O_7, the XRD pattern is shifted to higher 2θ as the unit cell contracts [27, 28]. Shifts in some particle patterns with respect to the U_3O_7 standard pattern in Figure 1 can be interpreted as slight variations in U/O stoichiometry, reflecting the heterogeneous, non-equilibrium conditions of formation.

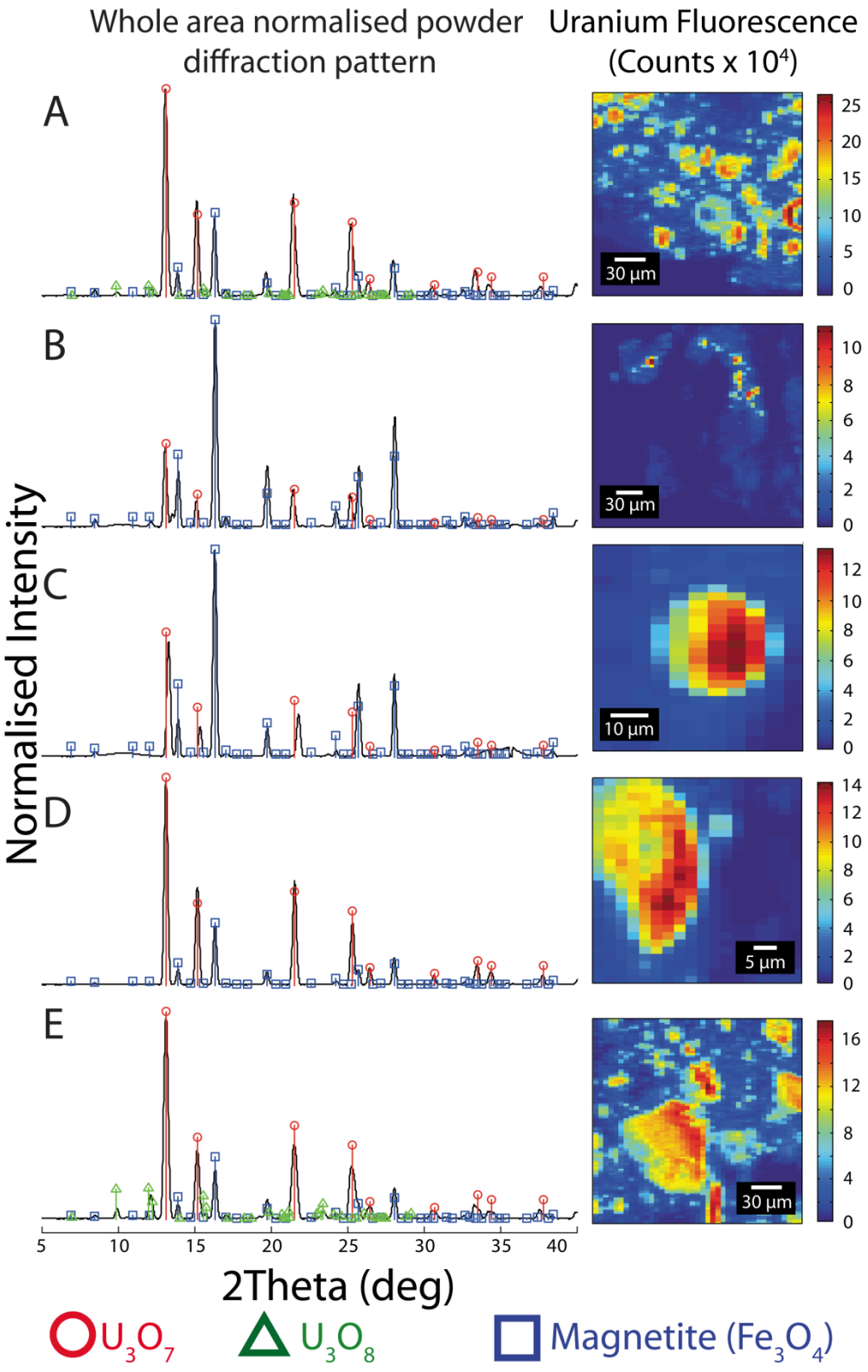

Figure 4.1 – Powder diffraction patterns and corresponding fluorescence maps for surface DU particles. Samples C and D are derived from single particles, whereas A, B and E include multiple particles in close proximity. Powder patterns are the superimposed sum of per pixel diffraction measurements made across the area mapped for fluorescence.

No metallic U, or previously observed non-oxide U phases such as UC or UFe_2 [10] were observed, showing that all particles were oxidised. Compared to previous studies of environmental material [7, 10, 11], no UO_2 was found, indicating that uranium in these soils has been further oxidised either during impact conditions or as a result of environmental aging. In particular, U_3O_7 can form as a long-lived intermediate in low temperature (< 250°C) oxidative transformation of UO_2 to U_3O_8 [29], which may suggest environmental formation of this species.

Fe oxide phases are also present in all surface particle samples. Although Fe has been previously observed as a major element in some DU particles [5, 11], and some U-Fe phases have been observed (UFe_2) [10], the close association of Fe oxide phases with DU particles has not been previously characterised. It has been hypothesised that the Fe in particles originates from high temperature interaction with armour materials, and although the close association of magnetite with U species hints at the incorporation of armour derived Fe, magnetite is known to occur in local soils [30], and could also reflect incorporation or agglomeration with environmental material.

4.3.1.3 Uranium Oxidation State

XANES spectroscopy can give direct measurements of the oxidation state of uranium and information on the co-ordination environment by comparison to well characterised standards. Spectra for surface particles are shown in Figure 4.2. The average oxidation state in these particles is 4.7, which is consistent with the majority presence of U_3O_7 determined by XRD. XANES spectra of samples S1 and S2 closely resemble that of the UO_2 standard, with an intense and broad white line (labelled A in figure 4.2), and prominent post edge oscillation at around 17210 eV (labelled C in figure 4.2). These spectra also lack the shoulder feature on the white line (B), a multiple scattering resonance which indicates the presence of uranyl (UO_2^{2+}) species. Spectrum S3 shows intermediate characteristics, particularly in white line (A) and shoulder (B) shapes, suggestive of mixed uranium speciation in this sample. This is consistent with the minor presence of some higher oxides of uranium, such as U_3O_8.

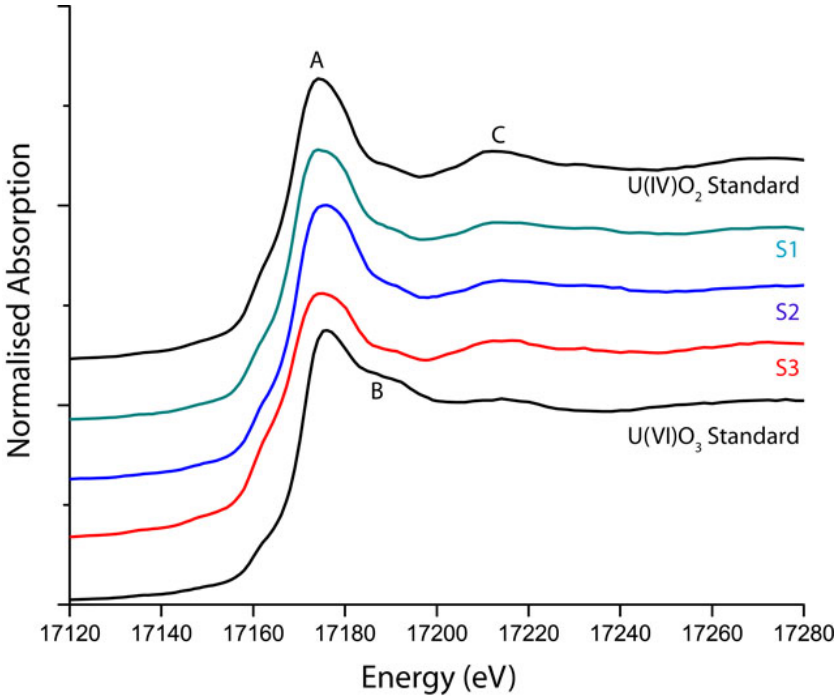

Figure 4.2 – Uranium L3 edge μ-XANES spectra of three surface particle areas (S1, S2 and S3) with UO_2 and UO_3 standards.

4.3.1.4 Phase and Oxidation State Imaging

Speciation mapping of a representative set of surface aerosol particles is shown in Figure 4.3. Phase identification from the whole image powder diffraction pattern (Appendix 1 - Figure A1.3) revealed reflections consistent with U_3O_7 and U_3O_8, with no other U phases detected. The distribution of these species was tracked across the sample to give a uranium phase map (Figure 4.3). Correlating fluorescence and diffraction maps in Figure 4.3, the particles appear to comprise distinct domains of the two species U_3O_7 and U_3O_8, probably reflecting high temperatures of formation, followed by rapid, heterogeneous quenching as the particles are scattered during impact [5]. XAS imaging agrees well with the U phase distribution, revealing areas of contrast in U oxidation state linked to the presence of different U oxide species.

This complementary set of analyses shows that speciation of uranium in particles from these surface soils is very similar to that determined for particles which have not been exposed to the environment [5, 6]. Although the surface environment at this site is both variably moist and oxic, conditions which would be expected to promote the oxidation of U(IV) to U(VI), no

substantial deviation in U speciation from primary oxide phases has occurred. This indicates that the potential for remobilisation and possible inhalation will persist, but with little associated risk of dissolution and transport of U(VI).

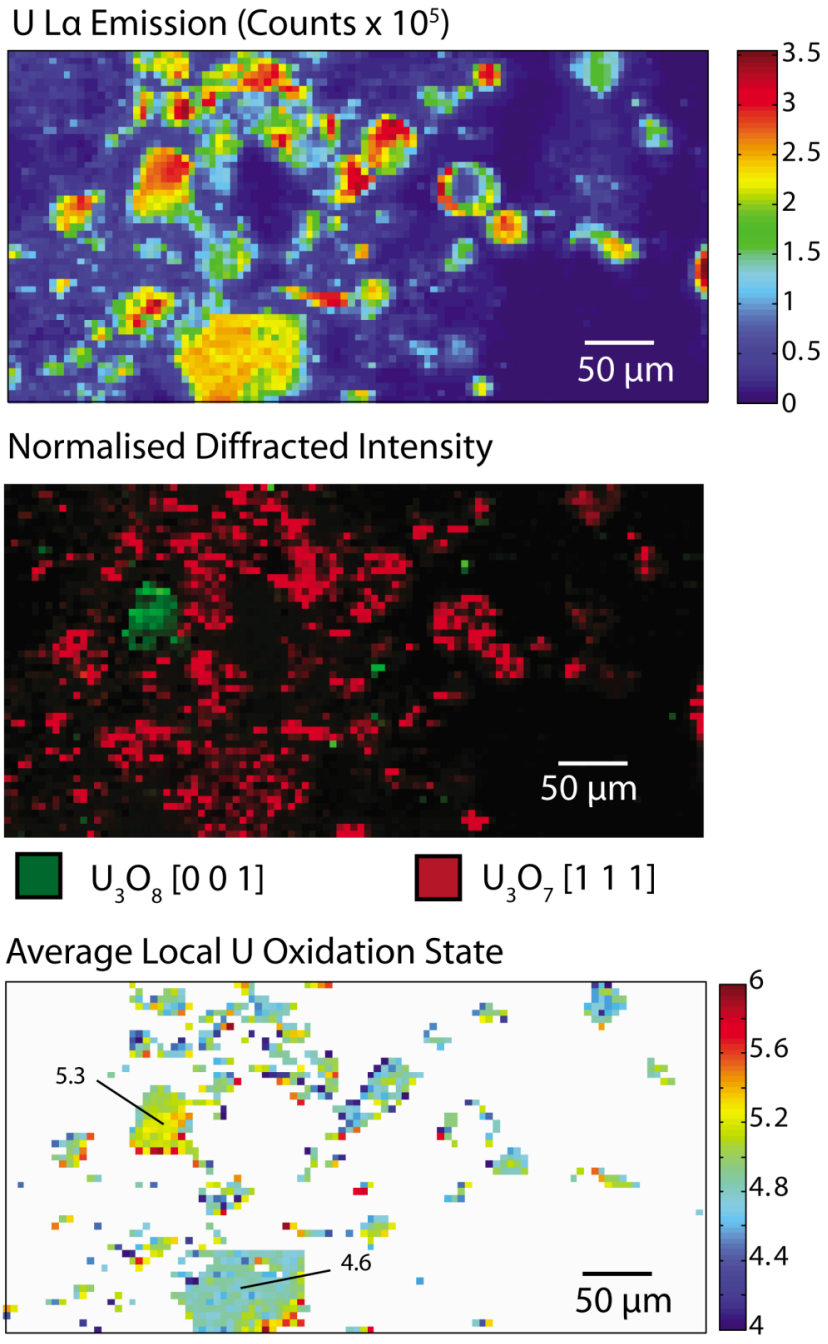

Figure 4.3 – Localised speciation imaging of DU particles from surface soils. Diffraction imaging reveals distinct domains of U_3O_8 and U_3O_7 species. Average oxidation state determined by thresholded XAS mapping is consistent with XRD results showing variation in local U oxidation state in different particles.

4.3.2 – 'Storage Pit Particles' - Sample Point 1

Samples from site 1 have a different environmental history to site 2. Due to their close proximity to impacts, timbers used in the construction of targets became heavily contaminated with DU aerosol and fragments during test firing. When the targets were dismantled, the contaminated wood was disposed on site in a burial pit.

4.3.2.1 Phase Identification

Particles in sample F (Figure 4.4) have similar phase composition to particles from surface soils, with U_3O_7 and magnetite present. As for particles imaged above, the dominance of these primary species in the composition of the particle indicates only minor alteration. In the other samples however (G – J, Figure 4.4), a marked change in U speciation has occurred, and the uranyl phosphate phase meta-ankoleite ($K(UO_2)(PO_4)\cdot 3H_2O$) is the dominant species present in all other diffraction patterns. XRF mapping presented in Figure 4.4 also indicates a change in length scale, with rather uniform uranium distributions observed over 100 – 1000 μm rather than the predominantly < 50 μm scale of particles imaged in Figure 4.1. There are also reflections for quartz, probably from sand grains which may be covered by secondary phases.

4.3.2.2 Morphologies and Compositions

Particles were analysed by SEM and low vacuum μ-XRF for morphology and low-Z elemental composition (Figure 4.5). Morphologies were distinct from both surface sample particles and previous studies of DU contamination. Few characteristic spherical aerosol derived particles were observed, and U deposits ranging in length scale 10 – 500 μm with a platy crystal habit were detected, comparable to U distributions imaged in Figure 4.4. Elemental mapping shows that the distribution of U and P is well correlated with the backscattered SEM image. These data support the identification of uranyl phosphate hydrate phases assigned from powder diffraction analysis.

Due to interference between K Kα (3313.8 eV) and U Mβ (3339.8 eV) lines, independent mapping of these elements is not possible using this instrument. Examination of individual particle spectra (figure 4.5) shows the intensity of the combined K Kα/U Mβ with respect to the

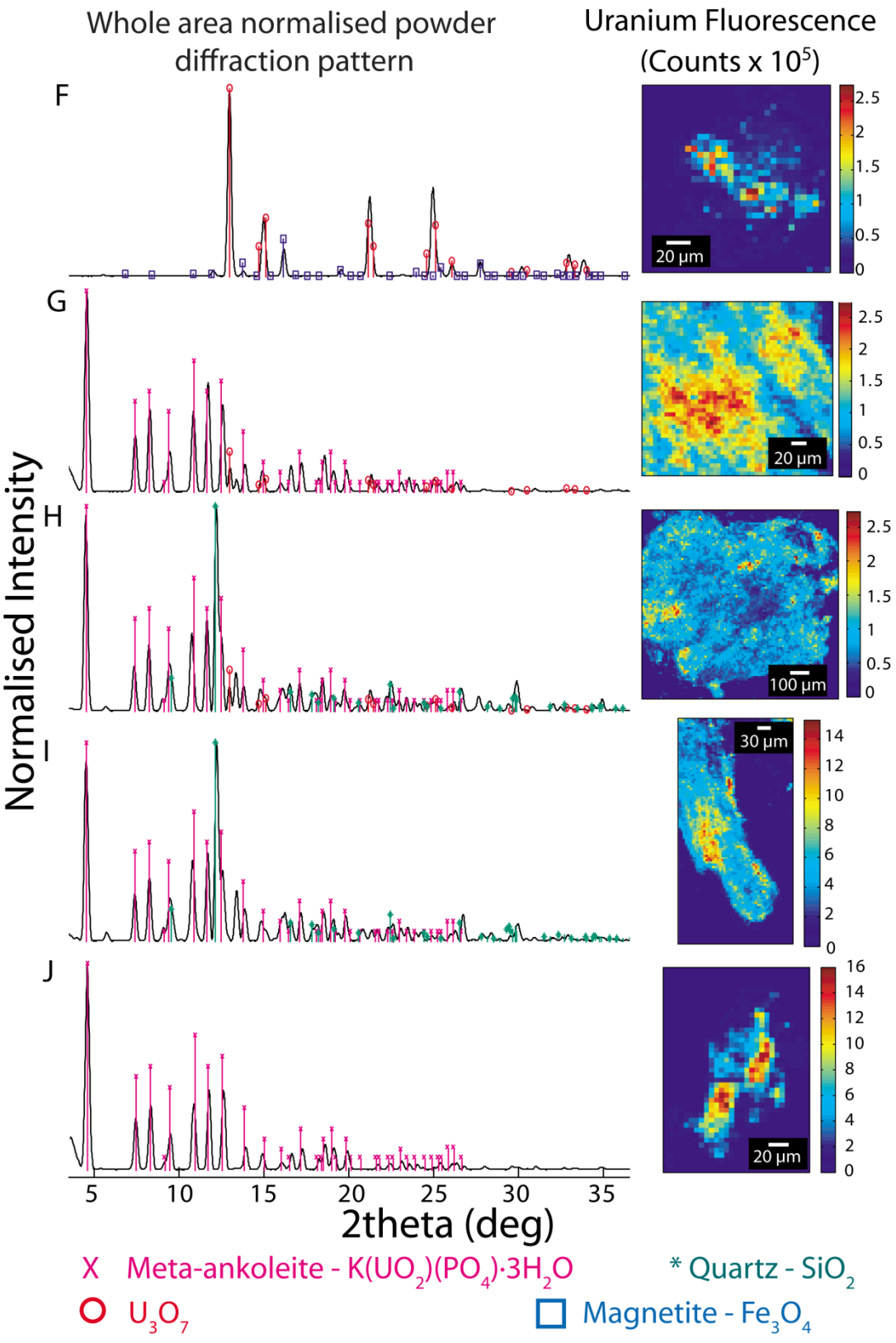

Figure 4.4 – Powder diffraction patterns and corresponding fluorescence maps for storage pit DU particles. Powder patterns are the superimposed sum of per pixel diffraction measurements made across the area mapped for fluorescence.

U Mα peak varies between samples. However, similar variation in diffraction patterns are not observed, which may suggest the presence of iso-structural mineral phases such as chernikovite ($(H_3O)_2(UO_2)_2(PO_4)_2 \cdot 6H_2O$) [31]. As these minerals have similar dissolution behaviour [31], the uncertainty in uranium speciation should not have a strong influence on the environmental source term of U in these soils.

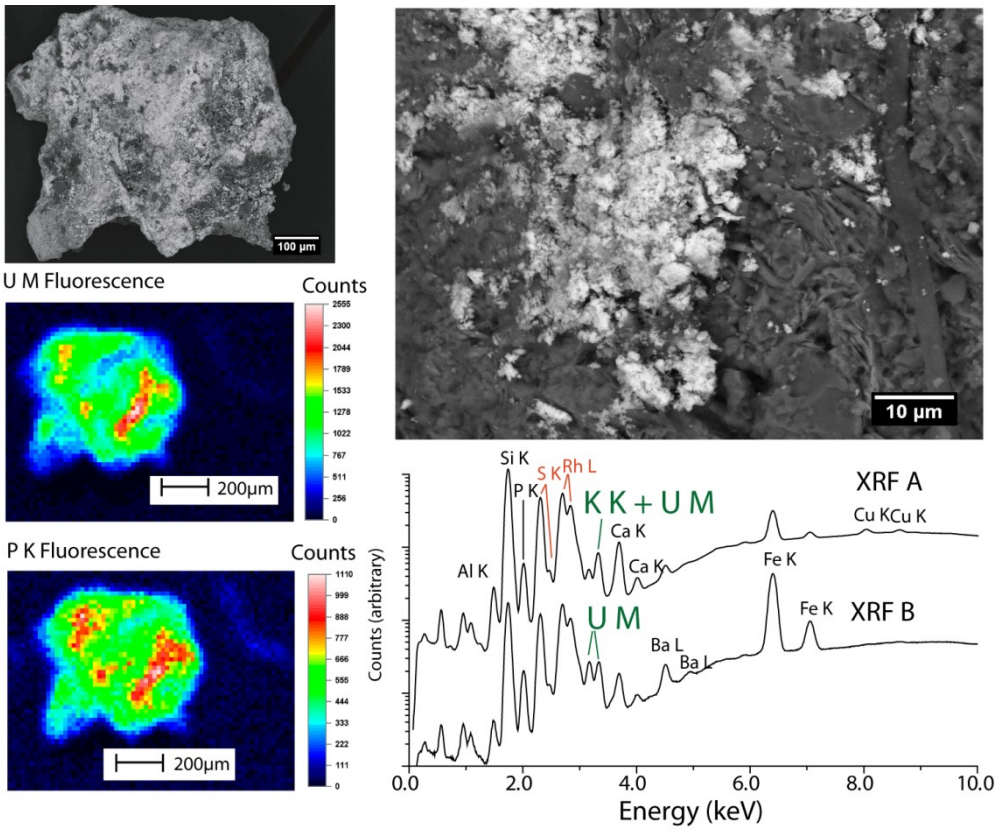

Figure 4.5 –SEM and scanning µ-XRF analyses of pit particles. Platy crystals and strongly correlated distributions of U and P are observed in pit samples, indicative of the formation of uranyl phosphate alteration products. Normalised and stacked XRF spectra show that the presence of K varies between particles. Rh and S lines marked in red are from the X-ray tube and sample mounting respectively.

4.3.2.3 Uranium Oxidation State

The oxidation state in particles was confirmed using XANES spectroscopy. In agreement with the results of phase identification, almost all XANES spectra give U(VI) as the majority oxidation state. The presence of a shoulder (feature B, Figure 4.6) on the white line (A)

confirms that U(VI) is present as uranyl (UO_2^{2+}) species, which is consistent with presence of uranyl phosphate hydrate species. Although U(IV) phases are present in some samples (Figure 4.6), almost all XANES spectra showed characteristic edge shifts and features consistent with only U(VI). As only a small area (approx. 2 µm x 5 µm) is probed by µ-XANES spectroscopy, this may indicate that residual U(IV) is highly localised in these samples, which would be consistent with the presence of few remaining primary particles.

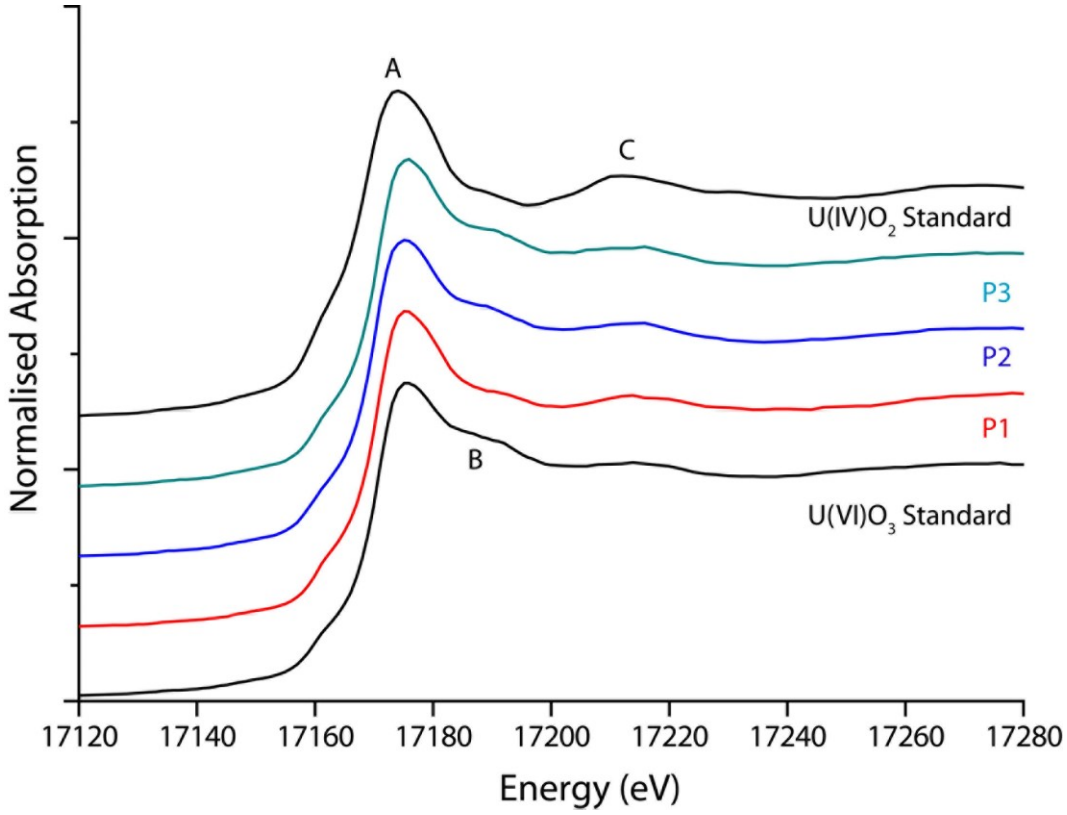

Figure 4.6 – Representative uranium L3 edge µ-XANES spectra of storage pit particles. Uranium in these soils is mainly in U(VI) oxidation state with small localised domains of U(IV), as seen in Figure 4.7.

4.3.2.4 Mapping

Figure 4.7 shows fluorescence, diffraction and XAS mapping for an area containing both U(IV) and U(VI) species. U_3O_7 distribution is correlated with high U fluorescence, particularly on the left of the image, and these concentrated domains probably represent primary particles. Phase distribution in the large particle is suggestive of a meta-ankoleite alteration layer which has

developed around a kernel of primary U_3O_7. XAS mapping of this particle reveals oxidation state distributions which agree with phase mapping. Average oxidation state in the central region is approximately 4.7 consistent with majority U_3O_7, and 6 in the rim area, consistent with the presence of uranyl phosphate species.

Point XANES measurements were used to confirm the results of oxidation state mapping, revealing contrast in speciation between the centre and outer rim (Figure 4.7). In particular, spectrum X2 has similar character to the UO_2 standard with a slight offset in edge position, indicating a minor contribution from U(VI) species in this central region. Both XANES measurements give very good agreement with the local oxidation state determined by imaging.

4.3.3 Environmental Behaviour

Taking these analyses together, a clear picture of U speciation is revealed in these aged residues, demonstrating a marked difference between the two sample sites studied, despite their close proximity.

Particles from site 2 are similar to those found in many other studies of DU particulate recovered from the environment [13]. The persistence of U oxide phases such as U_3O_7 and U_3O_8 reflects the low solubility and mobility of the primary species in surface soils at the Eskmeals site. However, the marked difference in U speciation observed in sample site 1 soil highlights the potential for alteration of U oxide species commonly found in primary DU particles to secondary minerals in some circumstances. At this site, the geochemical behaviour of U(VI)-phosphate-hydrate phases will probably be the main control on the environmental fate of DU.

Uranyl phosphate species have low aqueous solubility at circumneutral pH and, compared to reduced U oxide phases such as UO_2, U_3O_7 etc., are stable under oxic conditions [32]. These properties have made uranyl phosphates target phases for immobilisation and remediation of uranium in soils [32] and natural waters [33, 34]. In the near-surface, oxic conditions typically encountered by DU impact residues, it may be expected that U(VI) phosphate phases will persist in the environment for a long period of time.

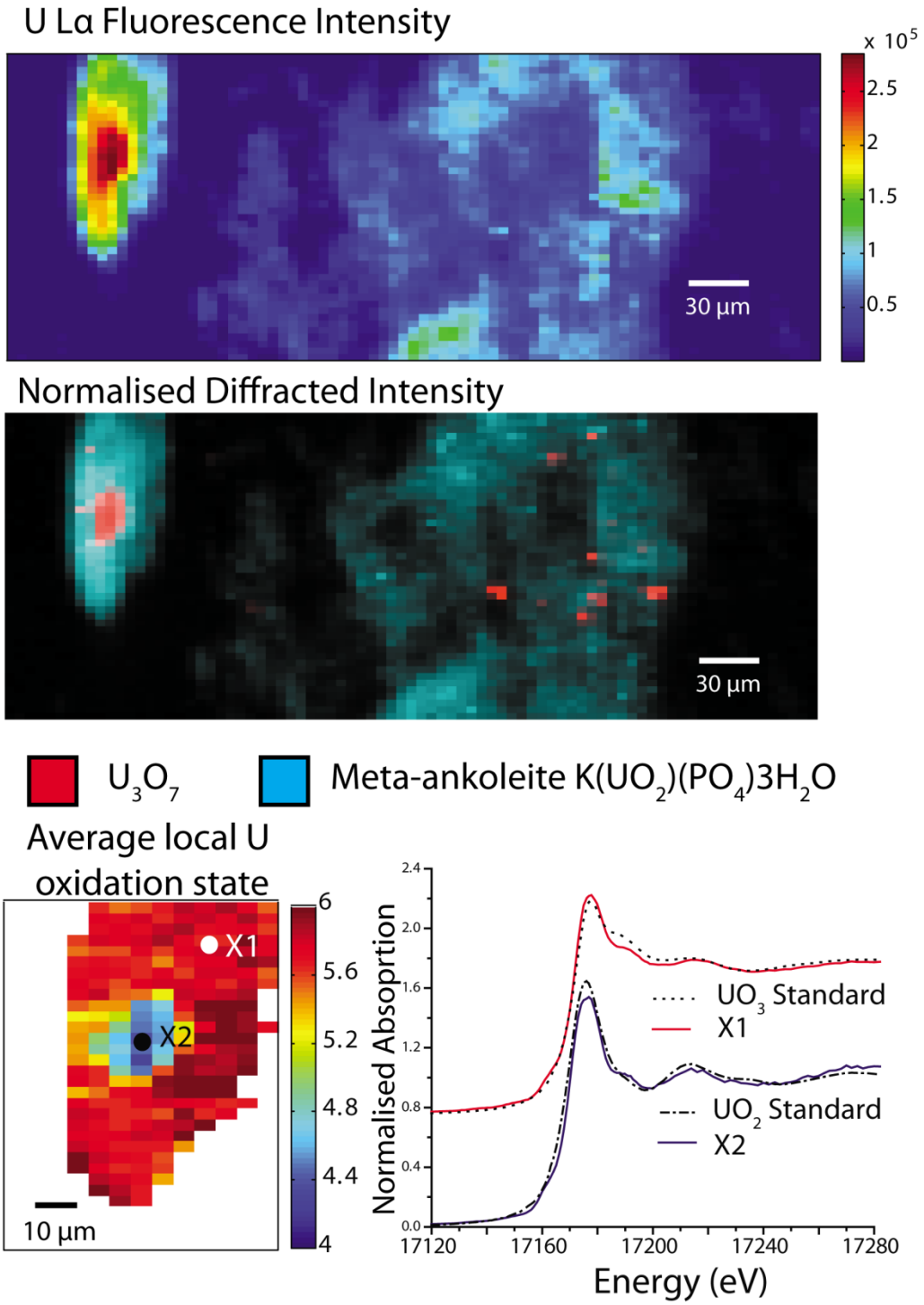

Figure 4.7 – Uranium phase imaging in timber storage area particles. Localised areas of primary U oxide phases are present, in addition to a hydrated uranyl phosphate phase which is not observed in surface samples. XAS mapping of a particle reveals contrast in oxidation state linked to phase distribution. Full XANES spectra of 'reduced' (X2) and 'oxidised' areas (X1) are plotted with U(IV) and U(VI) standards for comparison. The XAS map in this image was taken at 17.1677 keV only.

The size increase in U distribution from oxide particles (*ca* 5 - 20 μm, Figure 4.1 and Appendix 1 – Figure A1.2) to meta-ankoleite (*ca* 100-1000 μm, Figure 4.4 and 4.5) reduces the risk of resuspension and the associated inhalation hazard, and raises the prospect that alteration of primary U-O phases to low solubility secondary minerals may serve to reduce the immediate hazards posed by DU contamination at the Eskmeals site. However, it is not possible from this study to determine what fraction of the DU inventory is speciated in this way, and what fraction of the DU inventory is mobilised. This highlights that a more detailed knowledge of the conditions that promote alteration of DU particulate residues is required to understand fully the long term risk posed by DU munitions contamination.

4.4 Conclusions

DU particles exposed to the surface terrestrial environment for longer than 30 years at a UK firing range were characterised using synchrotron X-ray chemical imaging. Particles in a surface soil showed little extent of alteration, with U speciated as oxides U_3O_7 and U_3O_8. Uranium oxidation state and crystalline phase mapping revealed these oxides occur as separate particles, reflecting heterogeneous formation conditions. Particles recovered from the disposal area were substantially weathered, and U(VI) phosphate phases such as meta-ankoleite ($K(UO_2)(PO_4)•3H_2O$) were dominant. Chemical imaging revealed domains of contrasting U oxidation state linked to the presence of both U_3O_7 and meta-ankoleite, indicating growth of a particle alteration layer. The environmental behaviour of these species was discussed, and transformation to low solubility uranyl-phosphate phases may represent a stable chemical state in surface environmental conditions. More work on the leachability of these phases is required to understand the impact of this change in speciation on the hazard posed by DU contamination.

This study of DU particles by synchrotron X-ray chemical imaging also serves to demonstrate a comprehensive methodology for analysing uranium speciation in complex samples with little destructive sample preparation. The integration of diffraction, spectroscopy and fluorescence imaging and analysis presents a broad dataset from which to assess the interaction of DU munitions residues with the environment, which goes beyond bulk scale inference of speciation

from methods such as selective chemical extractions and improves on previous use of single point analysis of particles [7, 8, 10]. Such an approach may be useful in other systems where micron-scale resolution of speciation is critical to understanding the environmental behaviour of complex materials.

4.5 Acknowledgements

Paul Heath (University of Sheffield) assisted in collection of synchrotron microanalysis data. Tim Geer (QinetiQ) and Catherine Toque (DSTL) are thanked for assistance with gaining site access to Eskmeals and soil sampling.

4.6 References

[1] Bleise, A.; Danesi, P. R.; Burkart, W. Properties, use and health effects of depleted uranium (DU): a general overview. *J. Environ. Radioact.* **2003**, *64* (2-3), 93-112.

[2] The Royal Society, The health hazards of depleted uranium munitons - Part 1: Policy Document 6/01, **2002**.

[3] Papastefanou, C. Depleted Uranium in Military Conflicts and the Impact on the Environment. *Health Phys.* **2002**, *83* (2), 280-282.

[4] Briner, W. E. The evolution of depleted uranium as an environmental risk factor: lessons from other metals. *Int. J. Environ. Res. Public Health* **2006**, *3* (2), 129-135.

[5] Krupka, K. M.; Parkhurst, M. A.; Gold, K.; Arey, B. W.; Jenson, E. D.; Guilmette, R. A. Physicochemical characterization of capstone depleted uranium aerosols III: morphologic and chemical oxide analyses. *Health Phys*. **2009**, *96* (3), 276-291.

[6] Chazel, V.; Gerasimo, P.; Dabouis, V.; Laroche, P.; Paquet, F. Characterisation and dissolution of depleted uranium aerosols produced during impacts of kinetic energy penetrators against a tank. *Radiat. Prot. Dosimetry* **2003**, *105* (1-4), 163-166.

[7] Salbu, B.; Janssens, K.; Lind, O. C.; Proost, K.; Danesi, P. R. Oxidation states of uranium in DU particles from Kosovo. *J. Environ. Radioact*. **2003**, *64* (2-3), 167-173.

[8] Salbu, B.; Janssens, K.; Lind, O. C.; Proost, K.; Gijsels, L.; Danesi, P. R. Oxidation states of uranium in depleted uranium particles from Kuwait. *J. Environ. Radioact*. **2005**, *78* (2), 125-135.

[9] Torok, S.; Osan, J.; Vincze, L.; Kurunczi, S.; Tamborini, G.; Betti, M. Characterization and speciation of depleted uranium in individual soil particles using microanalytical methods. *Spectrochim. Acta. Part B At. Spectrosc.* **2004**, *59* (5), 689-699.

[10] Lind, O. C.; Salbu, B.; Skipperud, L.; Janssens, K.; Jaroszewicz, J.; De Nolf, W. Solid state speciation and potential bioavailability of depleted uranium particles from Kosovo and Kuwait. *J. Environ. Radioact*. **2009**, *100* (4), 301-307.

[11] Sajih, M.; Livens, F. R.; Alvarez, R.; Morgan, M. Physicochemical characterisation of depleted uranium (DU) particles at a UK firing test range. *Sci. Total Environ*. **2010**, *408* (23), 5990-5996.

[12] Cheng, Y. S.; Kenoyer, J. L.; Guilmette, R. A.; Parkhurst, M. A Physicochemical characterization of capstone depleted uranium aerosols II: particle size distributions as a function of time. *Health Phys*. **2009**, *96* (3), 266-275.

[13] Handley-Sidhu, S.; Keith-Roach, M. J.; Lloyd, J. R.; Vaughan, D. J. A review of the environmental corrosion, fate and bioavailability of munitions grade depleted uranium. *Sci. Total Environ.* **2010**, *408* (23), 5690-5700.

[14] Larson, S.; Ballard, J.; Medina, V.; Thompson, M.; O'Connor, G.; Griggs, C.; Nestler, C. Separation of depleted uranium from soil. *US Army Engineering Research and Development Centre, Vicksburg MS Environmental Labs*. **2009**

[15] Grenthe, I.; Drozdynski, J.; Fujino, T.; Buck, E. C.; Ablrecht-Schmitt, T. E.; Wolf, S. F., Uranium. In *The Chemistry of the Actinide and Transactinide Elements*, Morss, L. R.; Edelstein, N. M.; Fuger, J., Eds. Springer: **2010**; Vol. 1, pp 253.

[16] Choppin, G. R.; Stout, B. E., Actinide behavior in natural-waters. *Sci. Total Environ.* **1989**, *83* (3), 203-216.

[17] Oliver, I. W.; Graham, M. C.; MacKenzie, A. B.; Ellam, R. M.; Farmer, J. G. Assessing depleted uranium (DU) contamination of soil, plants and earthworms at UK weapons testing sites. *J. Environ. Monit.* **2007**, *9* (7), 740-748.

[18] Carter, T.; Phillips, M.; Toque, C. Comparison of Kirkcudbright and Eskmeals Environmental Monitoring Data with Generalised Derived Limits for Uranium. DSTL, **2002**.

[19] De Nolf, W.; Janssens, K. Micro X-ray diffraction and fluorescence tomography for the study of multilayered automotive paints. *Surf. Interface Anal*. **2010**, *42* (5), 411-418.

[20] Curti, E.; Grolimund, D.; Borca, C. N., A micro-XAS/XRF and thermodynamic study of CeIII/IV speciation after long-term aqueous alteration of simulated nuclear waste glass: Relevance for predicting Pu behavior? *Appl. Geochem.* **2012,** *27*, (1), 56-63.

[21] Borca, C. N.; Grolimund, D.; Willimann, M.; Meyer, B.; Jefimovs, K.; Vila-Comamala, J.; David, C. The microXAS beamline at the Swiss Light source: towards nano-scale imaging. *J. Phys.: Conf. Ser.* **2009**, 186, (1), 012003

[22] Taguchi, T.; Broennimann, C.; Eikenberry, E. F. Next generation X-ray detectors for in-house XRD. *Powder Diffr.* **2008**, *23* (2), 101-105.

[23] James, M.; Carter, M. L.; Watson, J. N. The synthesis, crystal chemistry and structures of Y-doped brannerite ($U_{1-x}Y_xTi_2O_6$) and thorutite ($Th_{1-x}Y_xTi_2O_{6-\delta}$) phases. *J. Solid State Chem.* **2003**, *174* (2), 329-333.

[24] Magnuson, M.; Butorin, S. M.; Werme, L.; Nordgren, J.; Ivanov, K. E.; Guo, J. H.; Shuh, D. K. Uranium oxides investigated by X-ray absorption and emission spectroscopies. *Appl. Surf. Sci.* **2006**, *252* (15), 5615-5618..

[25] Hunter, D. B.; Bertsch, P. M. In situ examination of uranium contaminated soil particles by micro-X-ray absorption and micro-fluorescence spectroscopies. *J. Radioanal. Nucl. Chem.* **1998**, *234* (1-2), 237-242.

[26] Grolimund, D.; Senn, M.; Trottmann, M.; Janousch, M.; Bonhoure, I.; Scheidegger, A. M.; Marcus, M. Shedding new light on historical metal samples using micro-focused synchrotron X-ray fluorescence and spectroscopy. *Spectrochim. Acta. Part B At. Spectrosc* **2004**, *59* (10–11), 1627-1635.

[27] He, H.; Shoesmith, D. Raman spectroscopic studies of defect structures and phase transition in hyper-stoichiometric UO(2+x). *Phys. Chem. Chem. Phys*. **2010**, *12* (28), 8108-8117.

[28] Teske, K.; Ullmann, H.; Rettig, D. Investigation of the oxygen activity of oxide fuels and fuel-fission product systems by solid electrolyte techniques. Part I: Qualification and limitations of the method. *J. Nucl. Mater.* **1983**, *116* (2–3), 260-266.

[29] McEachern, R. J.; Taylor, P. A review of the oxidation of uranium dioxide at temperatures below 400°C. *J. Nucl. Mater.* **1998**, *254* (2–3), 87-121.

[30] Hamilton, E. I., The role of near-shore industrial waste releases in the dispersion of radionuclides in the NE Irish Sea. *J. Environ. Radioact*. **1999**, *44* (2–3), 297-333.

[31] VanHaverbeke, L.; Vochten, R.; VanSpringel, K. Solubility and spectrochemical characteristics of synthetic chernikovite and meta-ankoleite. *Mineral. Mag.,* **1996**, *60* (402), 759-766.

[32] Fanizza, M. F.; Yoon, H.; Zhang, C.; Oostrom, M.; Wietsma, T. W.; Hess, N. J.; Bowden, M. E.; Strathmann, T. J.; Finneran, K. T.; Werth, C. J., Pore-scale evaluation of uranyl phosphate precipitation in a model groundwater system. *Water Resour. Res.* **2013,** *49*, (2), 874-890.

[33] Martinez, R. J.; Beazley, M. J.; Taillefert, M.; Arakaki, A. K.; Skolnick, J.; Sobecky, P. A., Aerobic uranium (VI) bioprecipitation by metal-resistant bacteria isolated from radionuclide- and metal-contaminated subsurface soils. *Environ. Microbiol.* **2007,** *9*, (12), 3122-3133.

[34] Seaman, J. C.; Hutchison, J. M.; Jackson, B. P.; Vulava, V. M., In situ treatment of metals in contaminated soils with phytate. *J. Environ. Qual.* **2003,** *32*, (1), 153-161.

Chapter 5

Determination of the uranium oxidation state in $UFeO_4$ by X-ray microanalysis of an environmental hot particle[2]

5.1 Introduction

Radioactive hot particles are introduced into the environment by a number of civil and military nuclear events, including nuclear power plant (NPP) accidents, effluent discharges from nuclear fuel reprocessing and nuclear weapons testing [1]. In order to understand the long term environmental behaviour and health risk posed by these particles, information on physiochemical characteristics is required such as morphology, radionuclide inventory and major element speciation. These data can also provide information on the formation and origin of hot particles [2].

In this study, information on the chemical speciation of U in a hot particle containing the ternary oxide $UFeO_4$ is obtained from multi-technique synchrotron X-ray microscopy. Ternary compounds in the U-Fe-O system are of interest in the interaction of uranium wastes with iron oxides [3] and as a component of 'corium', the melted residue of a nuclear reactor core produced in severe nuclear power plant accidents [4]. Iron is ubiquitous in structural components of nuclear reactor systems, and in particular, some modern nuclear reactor designs employ hematite as a sacrificial barrier in core catcher systems [5]. Compounds of Fe and U have also been previously described as minority phases in some hot particles [6].

In the U-Fe-O system two ternary oxides are known, $UFeO_4$ [7] and UFe_2O_6 [8], the latter suggested to be stable only at high pressure [3, 8]. $UFeO_4$ crystallises in an orthorhombic

[2] This chapter has been prepared in the form of a manuscript for submission as a paper. All research work, manuscript and figure preparation was performed by the author of this thesis. Co-authors Francis Livens and Neil Hyatt are acknowledged for supervision and advisory input to the content and structure of the manuscript, and Martin Stennett, Camelia Borca and Daniel Grolimund for assistance with performing synchrotron microanalysis experiments.

system with space group *Pbcn* [7], and a similarly structured ternary oxide in the U-Cr-O ternary system ($UCrO_4$) has also been synthesised and characterised [9]. The oxidation state of uranium in these compounds has been inferred as U(V) by measurement of a small magnetic moment on the U atom [9, 10]. Pentavalent uranium disproportionates to U(IV) and U(VI) in aqueous systems, and as such is rarely found in geologic materials [11]. However, many compounds of U(V) have been synthesised and characterised, including some examples of naturally occurring U(V) minerals, of which wyartite ($CaU^{5+}(UO_2)^2(CO_3)O_4(OH)(H_2O)_7$) was the first to be identified [12]. The most common co-ordination environment for U(V) is typically pentagonal bipyramidal [13], although some structures containing pentavalent U in 8-fold [14] and distorted octahedral environments are reported [11]. The U sites in $UFeO_4$ and $UCrO_4$ are octahedral with differing extents of distortion [7, 9].

The high X-ray photon flux and small spot size achievable with modern microfocus synchrotron X-ray beamlines [15] allows the use of localised X-ray absorption spectroscopy (XAS) techniques to probe the oxidation state and chemical environment of elements in hot particles, which may not be amenable to regular preparation or characterisation methods. The particle in this study was recovered from soils contaminated as a result of depleted uranium (DU) munitions test firing [16]. The use of these techniques provides a direct measure of the uranium oxidation state to resolve the ambiguity of U valence in $UFeO_4$, and provide evidence on the environmental behaviour of this compound. Coupled with refinement of micro X-ray diffraction data, and elemental analysis by microfocus X-ray fluorescence spectroscopy, these techniques provide an integrated methodology for non-destructive chemical characterisation of hot particles.

5.2 Experimental Methodology

5.2.1 Particle Collection

Particles containing DU were sampled from the UK Ministry of Defence Eskmeals firing range, Cumbria, UK in November 2011 and separated using autoradiography and sample splitting [17]. Soil sampling and preparation was described previously [18]. The particle recovered for this

study was from DU contaminated soil that has been exposed to the environment for at least 25 years, and comes from site 1 soils (Figure 3.1).

5.2.2 Synchrotron X-ray Micro-Analysis

Particles were mounted on Kapton tape for microfocus X-ray characterisation experiments performed at the microXAS (XL05A) beamline at the Swiss Light Source [15]. The source spot size was 2 μm (v) x 5 μm (h), and the samples were mounted on an x-y-z stage at 25° to the incident beam to allow localisation of different areas of interest in the beam. All data were collected at ambient conditions. X-ray fluorescence (μ-XRF) spectra were collected using a Si(Li) detector (KETEK instruments) placed at 90° to the incident beam. 2D X-ray diffraction (XRD) patterns were recorded using a PILATUS 100K hybrid pixel array detector [19] mounted 46 mm behind the sample with a tungsten beamstop in place. The μ-XRD setup was calibrated with respect to a silicon standard (NIST 640c), and the angular resolution was approximately 0.1° 2θ. Incident photon energy for μ-XRF and μ-XRD was 17.500 keV (λ = 0.70849 Å).

5.2.3 Micro-XANES and Micro-EXAFS

X-ray absorption near edge structure (μ-XANES) spectroscopy was performed in fluorescence mode across an energy range of 16.900 to 17.500 keV. Energy calibration was performed with respect to the K-edge of yttrium foil (17.038 keV). μ-XANES spectra of uranium compounds of different oxidation state were recorded to aid interpretation, including UO_2 (U^{4+}), $U_{0.5}Y_{0.5}Ti_2O_6$ (U^{5+}) [14], U_3O_8 ($U^{5.33+}$) [20] and UO_3 (U^{6+}). Standards were prepared as 3 mm diameter pellets of ceramic powders distributed in polyethylene glycol (PEG). The edge shift from U^{4+} to U^{6+} standards was 3.2 eV and the energy resolution across the edge region was 0.1 eV, resulting in an oxidation state uncertainty of approximately 3%.

Extended X-ray absorption fine structure (μ-EXAFS) spectroscopy was performed in fluorescence mode at the uranium L_3 edge. Data were collected across an energy range of 16.900 keV to 18.000 keV. Raw XAS data were processed using the program Athena [21] to remove the absorption edge background. EXAFS data were self-absorption corrected with an idealised composition of only $UFeO_4$ using the Troger algorithm implemented in Athena [21,

22]. Theoretical backscattering path phase and amplitude functions were calculated using FEFF 6 and fit to the data using the Artemis/IFEFFIT software package [21, 23]. Fits were performed to Fourier transformed R-space data with k-weights of 1, 2 and 3 to reduce parameter correlation.

5.2.4 Chemical Imaging

Rastering of a sample in the X-ray microbeam allows for maps of spatially resolved chemical information to be constructed. Elemental distributions were mapped by monitoring regions of the XRF spectrum corresponding to emission lines of interest whilst the sample was moved in the beam. Phase distributions were similarly mapped by monitoring the intensity of Bragg reflections corresponding to phases of interest, using the software XRDUA [24].

The spatial distribution of uranium oxidation state was determined using a μ-XAS mapping approach [16, 25, 26]. Maps of absorption co-efficient were constructed from μ-XRF maps at two energies in the U L_3 XANES region (17.168 keV and 17.185 keV). The maps were divided by the incident X-ray intensity (I_0) to give distributions of X-ray absorption. The maps were normalised to absorption at a post-edge energy (17.500 keV) where there is minimal contrast between different chemical states. The oxidation state was calculated from the per-pixel absorption coefficient with reference to a linear calibration relationship derived from uranium standard spectra. Maps of oxidation state at both energies showed good agreement and were averaged.

5.3 Results and Discussion

5.3.1 Synchrotron X-ray Chemical Imaging

X-ray chemical imaging was used to probe the distribution uranium species in a set of DU particles recovered from contaminated soil on a UK firing range [16]. Areas containing uranium were localised using XRF mapping (Figure 5.1a), and the distribution of U species analysed by oxidation state and XRD mapping (Figure 5.1c, 5.1d). In this study, a particle containing $UFeO_4$ was characterised after first being localised and identified by this chemical imaging approach.

Figure 5.1d shows an approximately circular domain of $UFeO_4$, with a similar shaped region of elevated fluorescence intensity observed in both uranium and iron elemental maps (Figure 5.1a, 5.1b). These distributions suggest a spherical particle, which is a common morphology for residues formed from the firing of DU munitions against hard targets, due to melting of metallic uranium [17]. Such particles have been observed previously in soils from this site [17, 18]. Reflections matching a mineral of the meta-autunite group with monovalent interlayer cations ($X^+(UO_2)(PO_4)\cdot 3H_2O$) were also present in diffraction data, and this phase appears to be a widespread alteration product formed from partial weathering of DU particles in the soil, as described in Chapter 4 (Figure 5.1d) [16]. Previous work (Chapter 4) has shown this to be either meta-ankoleite ($K(UO_2)(PO_4)\cdot 3H_2O$) or chernikovite ($H_3O(UO_2)(PO_4)\cdot 3H_2O$) by μ-XRD and μ-XRF.

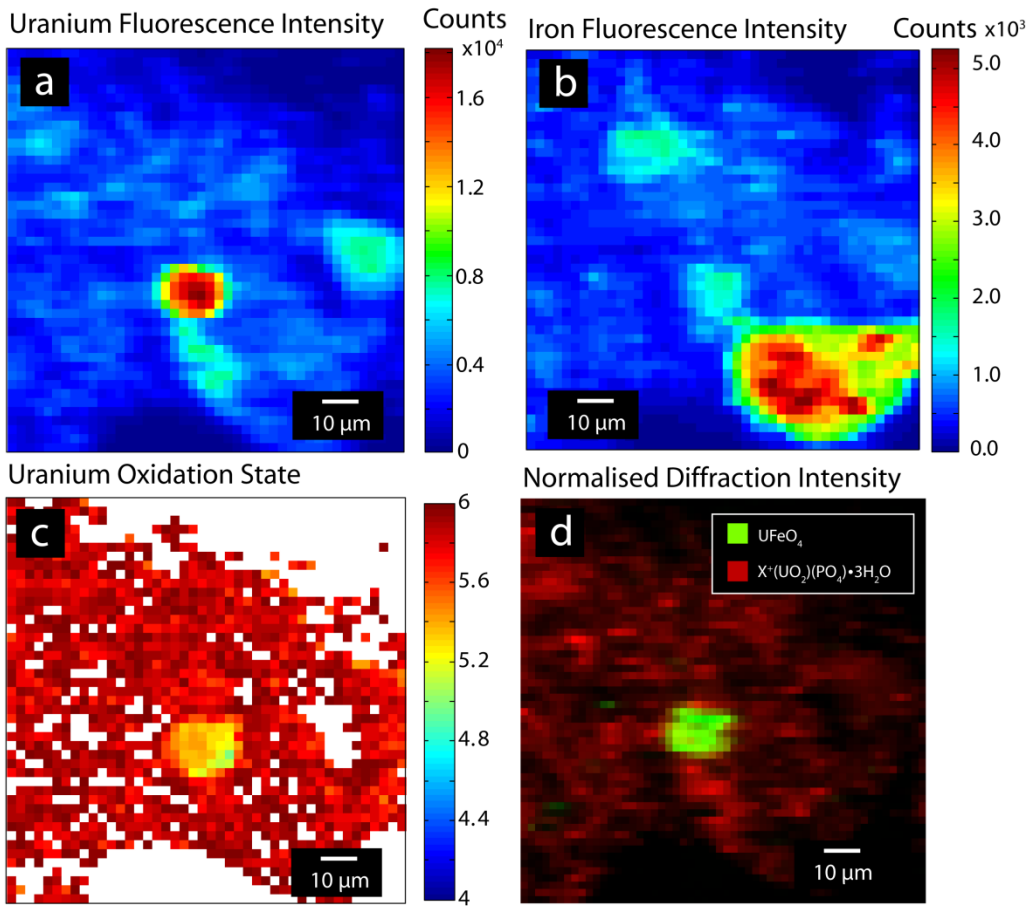

Figure 5.1 – U and Fe X-ray fluorescence (a,b), uranium redox (c) and crystalline uranium phase (d) chemical imaging of a DU particle containing $UFeO_4$. ($X^+(UO_2)(PO_4)\cdot 3H_2O$) is a mineral of the meta-autunite group, where X^+ is a monovalent cation.

Mapping of uranium oxidation state provides information on U speciation in the sample. Areas of U(VI) correspond well to the distribution of the meta autunite group phase in the sample, whereas the central region has a reduced composition which correlates well with the distribution of $UFeO_4$. The oxidation state varies in the range 5.15 – 5.4 in this domain, consistent with the presence of pentavalent U in $UFeO_4$ as suggested by Bacmann *et. al*. [10].

5.3.2 Microfocus X-ray Diffraction and X-ray Fluorescence Spectroscopy

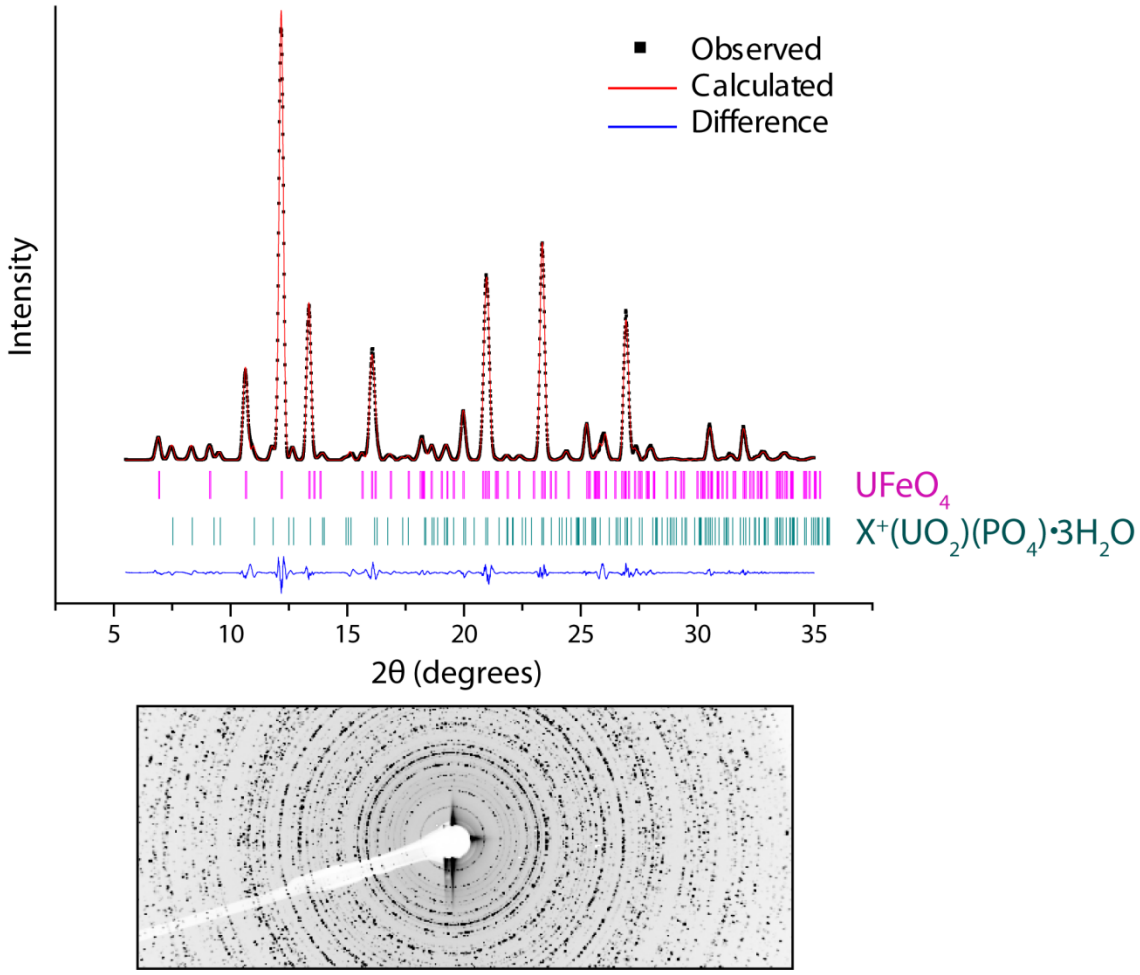

Figure 5.2 – Le Bail fit (solid line) to X-ray powder diffraction data (points) from a DU particle, with difference profile below (lower solid line). Tick marks show allowed reflections for the refined $UFeO_4$ and meta-autunite group mineral ($X^+(UO_2)(PO_4)\cdot 3H_2O$), which was initially modelled as meta-ankoleite ($X^+ = K^+$). The raw 2-D pattern shows incomplete rings due to low numbers of randomly oriented crystallites, which prevents a full analysis of the crystal structure.

Figure 5.2 shows powder diffraction data extracted from the DU particle in the centre of Figure 5.1a; the pattern was obtained by summing per-pixel XRD data over the particle area. These data show that the main phase present in this particle is $UFeO_4$, with a minor contribution from a secondary uranyl meta-autunite phase, which was modelled as meta-ankoleite [27].
U-Fe phases are thought to be produced by high temperature interactions (T ~ 3000°C [28]) which arise on impact of DU munitions with steels in armour plate. Laves phases such as UFe_2 have been observed in DU residues [6], and $UFeO_4$ can form as a minority high temperature oxidation product of this phase [29]. In this particle, however, the lack of other UFe_2 oxidation products (such as UO_2 or FeO [29]) suggests that $UFeO_4$ forms as a primary species. The presence of a $UFeO_4$ particle in these soils shows that this phase can persist in oxic, variably moist surface environment conditions, which may be expected to promote oxidation of uranium (V) phases to U(VI) species.

Quantitative analysis of powder diffraction data was performed using a Le Bail intensity extraction method [30]. A low number of randomly oriented crystallites in the particle was evident as 'spots' rather than full rings in the 2D diffraction pattern (Figure 5.2). Although the angular position of reflections is unaffected, this limits a full structural analysis (e.g. by Rietveld refinement) as the intensity of reflections in the pattern is distorted. This has been previously noted as a problem in the refinement of μ-XRD data [31].

The Le Bail method removes the link between the model structure and peak intensities, and allows unit cell parameters to be refined without a structural model, independent of preferred orientation effects. However for low symmetry systems this approach may incorrectly resolve closely spaced peaks, as intensities are not constrained by a structural model [32]. To overcome this, the results of Le Bail fitting are recommended to be compared with results from fitting to a structural model, even if this is imperfect [32]. In this study good agreement between Le-Bail refined unit cell parameters (Table 5.1) and a limited Rietveld analysis (data not shown) was observed.

Table 5.1 – LeBail refined unit cell parameters for the two uranium phases identified by powder diffraction. There is good agreement with the published unit cell values for $UFeO_4$. Unit cell parameters for the unknown meta-aunitite group mineral ($X^+(UO_2)(PO_4)\cdot 3H_2O$) suggest that it is Chernikovite, ($H_3O(UO_2)(PO_4)\cdot 3H_2O$). Uncertainty in the last figure of refined parameters is displayed in brackets.

Phase 1		**Fraction (wt. %)**	**a (Å)**	**b (Å)**	**c (Å)**	**Volume ($Å^3$)**
$UFeO_4$	Refined	95.91(4)	4.8930(5)	11.9065(8)	5.1086(5)	297.62(5)
$UFeO_4$	Bacmann et. al. [7]	_	4.888	11.937	5.11	298.15
Phase 2		**Fraction (wt.%)**	**a (Å)**	**b (Å)**	**c (Å)**	**Volume ($Å^3$)**
($X^+(UO_2)(PO_4)\cdot 3H_2O$)	Refined	4.10(5)	7.0265(6)	7.0265(6)	18.0275(4)	890.06(14)
Meta-ankoleite	Fitch et. al [27]	-	6.994	6.994	17.784	869.87
Chernikovite	Ross [33]	-	7.020	7.020	18.086	891.29

The pattern was adequately described ($\chi^2 = 6.48$, $R_{wp} = 13.7\%$, $R_p = 6.43\%$) with contributions from $UFeO_4$ as the majority phase (95.9 wt %) and a minority presence of a secondary phase (4.1 wt %) modelled initially as meta-ankoleite [27]. The good agreement of the refined and published unit cell values for $UFeO_4$ [7] gives quantitative identification of this species in the particle, and allows correlation of X-ray spectroscopy data with the published structure.

Refined unit cell parameters (Table 5.1) for the secondary phase show good agreement with the structure of chernikovite $(H_3O)(UO_2)(PO_4)\cdot 3H_2O$ [33], which has a larger unit cell than meta-ankoliete [27]. Meta-autunite group minerals ($X^+(UO_2)(PO_4)\cdot 3H_2O$) have layered uranyl and phosphate polyhedral chains with interlayers of water and different cations (X^+), which allows discrimination based on the unit cell size. The slight contraction in the *c* axis compared to the published structure of chernikovite may indicate a minority solid solution with meta-ankoleite.

As discussed in Chapter 4, although the interlayer cation composition is different, meta-ankoleite and chernikovite have similar dissolution characteristics, and their environmental behaviour will be similar. The co-location of minor amounts of chernikovite in this particle may suggest weathering of the $UFeO_4$ phase. However, the majority of the remaining particle (95.9 wt %) is still composed of $UFeO_4$, indicating environmental stability over the > 25 year period of exposure to the surface environment.

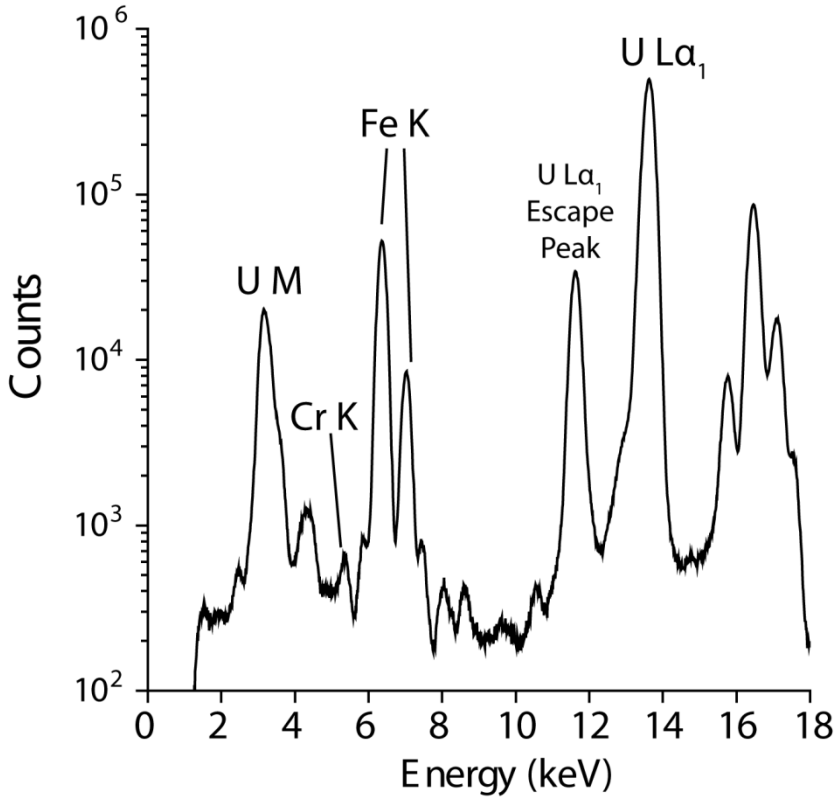

Figure 5.3 – Qualitative XRF spectrum of the particle from Figure 5.1 in which maximum counts for U $L\alpha_1$ (4.8×10^5) and Fe $K\alpha_1$ (5.2×10^4) compared to Cr $K\alpha_1$ (6.3×10^2) indicate that the U ternary oxide phase is $UFeO_4$ rather than $UCrO_4$. The excitation energy was 17.500 keV.

Due to the structural similarity between $UFeO_4$ and $UCrO_4$, qualitative XRF spectroscopy was performed to confirm the identity of the primary U species. Figure 5.3 shows that the particle is composed mainly of U and Fe, with only trace levels of Cr present. This result compares well

with the refined unit cell parameters which are in good agreement with the presence of $UFeO_4$ only.

This XRF data cannot be used to distinguish chernikovite from meta-ankoliete by because of interference between U M (U Mβ = 3339.8 eV) and K K (K Kα = 3313.8 eV) emission lines. To identify the presence of K, the ratio of peak intensities must be taken into account, as Kα/Kβ intensity ratios are higher for Mα/Mβ emissions. Figure 5.3 shows that the energy resolution of XRF spectroscopy using beamline instrumentation is not sufficient to resolve separate peaks in the 3.0 – 3.5 keV range, which prevents confirmation of secondary phase identity.

5.3.3 X-ray Absorption Spectroscopy

5.3.3.1 XANES

XANES spectra of the DU particle and U oxide standards are shown in Figure 5.4. The sample spectrum shows closest agreement with the U(V) ($U_{0.5}Y_{0.5}Ti_2O_6$) standard, although self absorption effects are evident, particularly in the dampening of white line and post-edge oscillation intensities. The 1st derivative of XANES spectra shows that the pre edge maximum (A) is of similar magnitude and the inflection point (B) is of similar position to that of $U_{0.5}Y_{0.5}Ti_2O_6$, which contains uranium in average oxidation state +5. A linear relationship between edge inflection energy and oxidation state was established from standard spectra, and interpolated to calculate a U oxidation state of +4.9 ± 0.15 (3%) in the sample.

Although damped by self-absorption, near edge structure suggests a U chemical environment distinct from that observed in UO_2 and UO_3 (Figure 5.4). In particular, the multiple scattering resonance at an energy 10-15 eV greater than the white line observed in the UO_3 spectrum, related to multiple scattering in the linear uranyl U(V/VI) structural unit ($O=U=O^{+/2+}$), was not observed in the sample spectrum [34]. The strongest post edge oscillation occurs at a similar energy (17230 eV) to that of the non-uranyl U(V) standard, and agrees well with other published XANES spectra of U(V) compounds [11, 35]. The use of XANES spectroscopy

provides direct evidence for the presence of U(V) in $UFeO_4$, supporting earlier inferences of Bacmann *et. al.* [10].

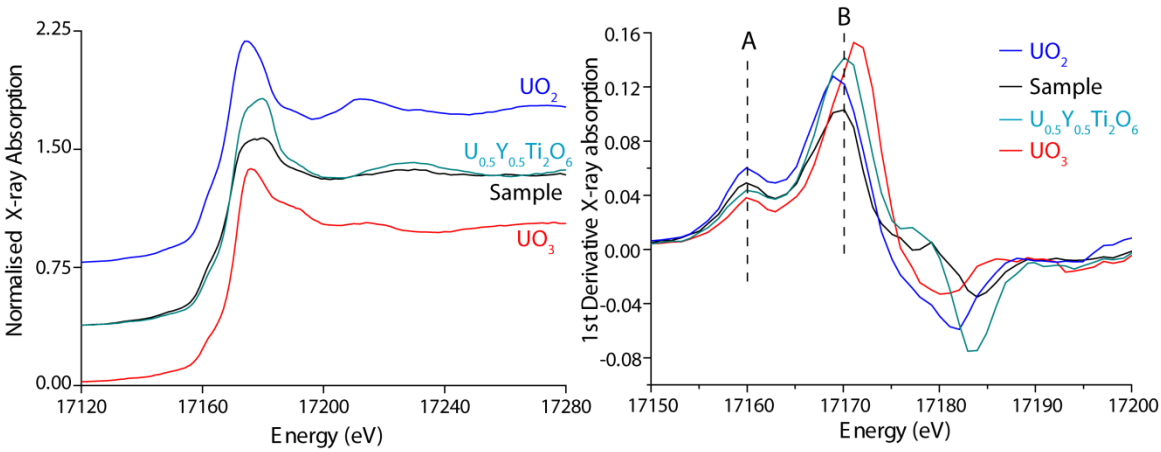

Figure 5.4 – U L_{III} XANES Spectrum of a $UFeO_4$ particle plotted with spectra of reference compounds UO_2, $U_{0.5}Y_{0.5}Ti_2O_6$ and UO_3. First inflection intensity (A) and edge inflection point position (B) indicate the average U oxidation state is close to+5 in the sample.

XAS mapping (Figure 5.1c) provides a more rapid method than XANES analysis to determine the spatial variation in oxidation state. Agreement between the oxidation state determined by XANES (+4.9 ± 0.15) and XAS redox mapping (particle average +5.2 ± 0.15) indicates a pentavalent U oxidation state throughout the particle. XAS mapping also reveals that the +5 oxidation state is homogeneous in the particle (Figure 5.1c), and agrees well with the distribution of $UFeO_4$ determined by XRD phase mapping (Figure 5.1d).

5.3.3.2 µ-EXAFS Analysis

Calculation of backscattering path amplitude and phase shift was based on the crystal structure of $UFeO_4$ determined by Bacmann [7]. The k-range used for analysis was limited by energy dependence of the microbeam position [36] to 2-8 $Å^{-1}$ (Δk =6 $Å^{-1}$), as at higher k movement of the beam across U concentration gradients in the sample introduces additional oscillations into the data. The Fourier transform R space resolution for distinguishing individual scattering paths is equivalent to 1 independent data point (1 idp = π / 2Δk) [37]. Using this criterion, 1 idp for this data is equivalent to 0.262Å, with a total of 9.73 independent data points (N_{idp}) in the R-

range of 1.2 – 3.75 Å (ΔR = 2.55 Å) used in fitting. No backscattering paths from chernikovite were included in the fit as the contribution of this phase to the composition of the particle was determined by XRD to be small (4.1%, Table 5.1).

Table 5.2 – Structural parameters determined by EXAFS analysis, uncertainty from fitting is shown in brackets. A total of 5 parameters were fit to 9.73 (N_{idp}) independent variables.

Shell	Path	N	R(Å)	σ^2 (Å^2)	Global Parameters	
1	O 2.1	6*	2.148(14)	0.0031 (11)	ΔE_0 (eV)	2.1 (1.3)
					S_0^2†	0.95
2	Fe 1.1	1	3.274(16)	0.0036(16)‡		
2	O 1.2	2	3.288(16)	0.0036(16)‡	**Goodness of Fit**	
2	O 2.3	2	3.667(18)	0.0036(16)‡	Red χ^2	6.72
2	Fe 1.3	6	3.735(19)	0.0036(16)‡	R (%)	1.45

*Co-ordination number increased from crystallographic value to account for averaging of multiple indistinguishable paths.

†S_0^2 fixed to 0.95

‡ Average σ^2 fit for all second shell paths.

Figure 5.5 shows the k^2 weighted EXAFS spectra and fits for k and R space from the $UFeO_4$ particle, with the fit detailed in Table 5.2. The intensity in R-space is consistent with the published structure of $UFeO_4$, with an intense and broad second peak arising from a number of scatterers in a complex second shell. Although the published structure of $UFeO_4$ indicates U in a distorted octahedral co-ordination, the R-space resolution offered by μ-EXAFS (ΔR = 0.262 Å) analysis shows this as a single intense peak in at 1.55 Å (Figure 5.5), corresponding to an average U-O distance of ~2.15 Å with phase correction. This shell was fitted using backscattering phase and amplitude terms calculated for the middle path length (R_0 = 2.155Å), with the path degeneracy (*N*) fixed at 6 instead of 2. The EXAFS path length for this shell was refined to 2.148 ± 0.012 Å (Table 1), representing an average of the U-O distances in the

distorted first shell geometry. This agrees well with the mean crystallographic (R_c) U-O distance calculated from the published structure of $UFeO_4$ (R = 2.149 Å) [7].

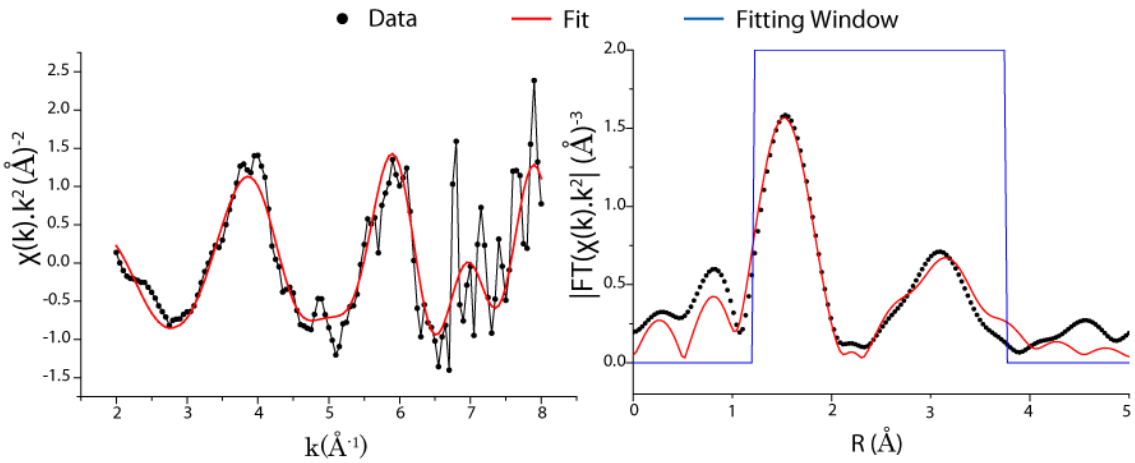

Figure 5.5 – Uranium L_{III} edge EXAFS spectra from a $UFeO_4$ particle. *Left* – background subtracted k^2-weighted EXAFS spectrum. *Right* – Fourier transform magnitude (k^2 weighted).

The second co-ordination shell in $UFeO_4$ is apparent as a broad peak in the μ-EXAFS data in the region 2.5 – 3.7 Å. The crystal structure shows this is expected to comprise 2 distinct O subshells and 3 Fe subshells. However, the close spatial relation of these paths and the limited number of available independent data points (N_{idp} = 9.53) mean it is not possible to resolve individual EXAFS parameters (σ^2, ΔR) for these paths. For the second shell paths in Table 5.2, changes in path length were described with a single scaling factor multiplied by the path length, and a single mean squared path length variation (σ^2) was used. This two parameter model for the second shell allows a reasonable fit to the data and extraction of useful chemical information from the first shell, in particular the average U-O distance as discussed above. This value can be used to confirm the oxidation state of U in $UFeO_4$ by bond valence sum analysis.

5.3.4 Bond Valence Sums

The bond valence sum method can be used to calculate element oxidation state [38], based on the principle that the bond length is a function of valence. The exponential parameterisation for cation bond valence (v_i) was used:

$$v_i = \sum_j \exp[(R_0 - R_{ij})/B],$$

where R_{ij} is the measured bond length, R_0 is a reference bond length for unity valence and B is a constant. Values for R_0 (2.051 Å) and B (0.57) were used from Burns *et. al.*[13], derived specifically for distinguishing valences of uranium. Using these parameters bond valence sums for well characterised pentavalent uranium compounds fall in the range of 4.82 – 5.26 [13]. In $UFeO_4$, the EXAFS refined bond length is 2.148 ± 0.012 Å, corresponding to a U valence of 4.96 ± 0.13. This is in close agreement with the value determined by XANES analysis (4.97 ± 0.15), consistent with U in the pentavalent oxidation state.

Bond valence sum analysis may also be applied to bond distances calculated from the published crystal structure. The uranium first shell distorted octahedral has 2 U-O bonds at 2.048 Å, 2 U-O bonds at 2.183 Å and 2 U-O bonds at 2.217Å, which give a bond valence sum of 5.00, in excellent agreement with the oxidation state of U determined by XANES and EXAFS for this particle. A corresponding Fe valence may also be calculated using the published structure – as the oxidation state of uranium has been determined as U(V), bond valence parameters for Fe(III)-O bonding were used (R_0 = 1.759 Å, B = 0.37) [38]. The bond lengths are 2 Fe-O at 1.992 Å, 2 Fe-O at 2.053 Å and 2 Fe-O 2.091 Å, which results in an Fe valence sum in $UFeO_4$ of 2.78 These analyses give indication that the cation pair in $UFeO_4$ is U(V)/Fe(III).

5.4 Conclusions

The presence of ternary U oxides in DU particles is indicative of extreme temperatures and pressures on impact with a hard target, and the absence of other Fe and U oxide species in this particle suggests a primary formation mechanism for $UFeO_4$.

The oxidation state of uranium in $UFeO_4$ was determined as U(V) by μ-focus synchrotron chemical imaging, μ-XANES and μ-EXAFS spectroscopies. Unit cell parameters of $UFeO_4$ were refined by Le Bail fitting of powder XRD data, revealing values consistent with the structure of $UFeO_4$ determined by Bacmann *et. al*. in 1967 [7]. This structure was used as an input to calculate EXAFS path amplitudes and phase shifts, which were found to fit well to the

data. Bond valence analysis of the EXFAS refined U-O bond and of the U and Fe sites in the original structure suggests a U^{5+}/Fe^{3+} couple, and confirms early studies of $UFeO_4$ in which U(V) was inferred [9, 10].

The occurrence of $UFeO_4$ in environmentally aged particles demonstrates the medium term (> 25 year) stability of this phase in an oxic and variably moist surface environment. This is a somewhat surprising result for species containing pentavalent uranium, and demonstrates that this oxidation state can be stabilised over long terms in oxic environments. The environmental stability of $UFeO_4$ is of interest in understanding the behaviour of uranium materials formed under extreme conditions, such corium melts formed in nuclear power plant accidents.

This study demonstrates the utility of microbeam X-ray experiments to extract chemical information from challenging samples by a range of complementary analyses, which may be of interest to characterisation of secondary minerals, alteration products and other materials for which bulk samples are not available for conventional characterisation regimes. This approach is particularly suitable for radioactive hot particles as and non-destructive, thereby preserving the limited sample for other analyses and allowing safe containment of the material.

5.5 Acknowledgements

Paul Heath (University of Sheffield) assisted in collection of synchrotron microanalysis data. Tim Geer (QinetiQ) and Catherine Toque (DSTL) are thanked for assistance with gaining site access to Eskmeals and soil sampling.

5.6 References

[1] Salbu, B., Radioactive Particles Released from Different Nuclear Sources. In *Radioactive Particles in the Environment*, Oughton, D. H.; Kashparov, V., Eds. Springer Netherlands: 2009; pp 3-13.

[2] Salbu, B., Source-related Characteristics of Radioactive Particles: A Review. *Radiat. Prot. Dosim.* **2000,** *92*, (1-3), 49-54.

[3] Nerikar, P.; Seifert, H. J.; Perrot, P., Iron - Oxygen - Uranium - Iron Systems: Phase Diagrams, Crystallographic and Thermodynamic Data. In *Selected Systems from Fe-N-V to Fe-Ti-Zr*, Effenberg, G., Ed. Springer 2009; Vol. 11.

[4] Almjashev, V. I.; Barrachin, M.; Bechta, S. V.; Bottomley, D.; Vitol, S. A.; Gusarov, V. V.; Defoort, F.; Krushinov, E. V.; Lopukh, D. B.; Lysenko, A. V.; Martynov, A. P.; Mezentseva, L. P.; Miassoedov, A.; Petrov, Y. B.; Fischer, M.; Khabensky, V. B.; Hellmann, S., Ternary eutectics in the systems FeO-UO_2-ZrO_2 and Fe_2O_3-U_3O_8-ZrO_2. *Radiochemistry* **2011,** *53*, (1), 13-18.

[5] Petrov, Y.; Udalov, Y.; Subrt, J.; Bakardjieva, S.; Sazavsky, P.; Kiselova, M.; Selucky, P.; Bezdicka, P.; Journeau, C.; Piluso, P., Phase equilibria during crystallization of melts in the uranium oxide-iron oxide system in air. *Glass Physics and Chemistry* **2009,** *35*, (3), 298-307.

[6] Lind, O. C.; Salbu, B.; Skipperud, L.; Janssens, K.; Jaroszewicz, J.; De Nolf, W., Solid state speciation and potential bioavailability of depleted uranium particles from Kosovo and Kuwait. *Journal of Environmental Radioactivity* **2009,** *100*, (4), 301-307.

[7] Bacmann, M.; Bertaut, E. F., Structure du nouveau compose $UFeO_4$. *Bulletin De La Societé Francaise Mineralogie Et De Cristallographie* **1967,** *90*, (2), 257.

[8] Collomb, A.; Capponi, J. J.; Gondrand, M.; Joubert, J. C., Synthèse de quelques oxydes mixtes de type $A^{6+}B_2^{3+}O_6$ en milieu hydrothermal sous tres haute pression. *Journal of Solid State Chemistry* **1978,** *23*, (3–4), 315-319.

[9] Bacmann, M.; Bertaut, E. F.; Bassi, G., Parameters atomiques et structure magnetique de $UCrO_4$. *Bulletin De La Societe Francaise Mineralogie Et De Cristallographie* **1965,** *88*, (2), 214.

[10] Bacmann, M.; Bertaut, E. F.; Blaise, A.; Chevalier, R.; Roult, G., Magnetic structures and properties of $UFeO_4$. *Journal of Applied Physics* **1969,** *40*, (3), 1131-1132.

[11] Fortner, J. A.; ropf, A. J.; Finch, R. J.; Bakel, A. J.; Hash, M. C.; Chamberlain, D. B., Crystal chemistry of uranium (V) and plutonium (IV) in a titanate ceramic for disposition of surplus fissile material. *J. Nucl. Mater.* **2002,** *304*, (1), 56-62.

[12] Burns, P. C.; Finch, R. J., Wyartite: Crystallographic evidence for the first pentavalent-uranium mineral. *American Mineralogist* **1999,** *84*, (9), 1456-1460.

[13] Burns, P. C.; Ewing, R. C.; Hawthorne, F. C., The crystal chemistry of hexavalent uranium; polyhedron geometries, bond-valence parameters, and polymerization of polyhedra. *The Canadian Mineralogist* **1997,** *35*, (6), 1551-1570.

[14] James, M.; Carter, M. L.; Watson, J. N., The synthesis, crystal chemistry and structures of Y-doped brannerite ($U_{1-x}Y_xTi_2O_6$) and thorutite ($Th_{1-x}Y_xTi_2O_{6-\delta}$) phases. *Journal of Solid State Chemistry* **2003,** *174*, (2), 329-333.

[15] Borca, C. N.; Grolimund, D.; Willimann, M.; Meyer, B.; Jefimovs, K.; Vila-Comamala, J.; David, C., The microXAS beamline at the Swiss Light source: towards nano-scale imaging. In *9th International Conference on X-Ray Microscopy*, David, C.; Nolting, F.; Quitmann, C.; Stampanoni, M.; Pfeiffer, F., Eds. 2009; Vol. 186.

[16] Crean, D. E.; Livens, F. R.; Stennett, M. C.; Grolimund, D.; Borca, C. N.; Hyatt, N. C., Micro-analytical Imaging of Depleted Uranium Speciation in Munitions Residues. *Paper under review* **2013**.

[17] Sajih, M.; Livens, F. R.; Alvarez, R.; Morgan, M., Physicochemical characterisation of depleted uranium (DU) particles at a UK firing test range. *Sci Total Environ* **2010,** *408*, (23), 5990-6.

[18] Crean, D. E.; Livens, F. R.; Sajih, M.; Stennett, M. C.; Grolimund, D.; Borca, C. N.; Hyatt, N. C., Remediation of soils contaminated with particulate depleted uranium by multi stage chemical extraction. *Journal of Hazardous Materials* **2013,** In press

[19] Taguchi, T.; Broennimann, C.; Eikenberry, E. F., Next generation X-ray detectors for in-house XRD. *Powder Diffraction* **2008,** *23*, (2), 101-105.

[20] Magnuson, M.; Butorin, S. M.; Werme, L.; Nordgren, J.; Ivanov, K. E.; Guo, J. H.; Shuh, D. K., Uranium oxides investigated by X-ray absorption and emission spectroscopies. *Applied Surface Science* **2006,** *252*, (15), 5615-5618.

[21] Ravel, B.; Newville, M., ATHENA, ARTEMIS, HEPHAESTUS: data analysis for X-ray absorption spectroscopy using IFEFFIT. *Journal of Synchrotron Radiation* **2005,** *12*, 537-541.

[22] Tröger, L.; Arvanitis, D.; Baberschke, K.; Michaelis, H.; Grimm, U.; Zschech, E., Full correction of the self-absorption in soft-fluorescence extended x-ray-absorption fine structure. *Physical Review B* **1992,** *46*, (6), 3283-3289.

[23] Newville, M., IFEFFIT: interactive XAFS analysis and FEFF fitting. *Journal of Synchrotron Radiation* **2001,** *8*, 322-324.

[24] De Nolf, W.; Janssens, K., Micro X-ray diffraction and fluorescence tomography for the study of multilayered automotive paints. *Surface and Interface Analysis* **2010,** *42*, (5), 411-418.

[25] Curti, E.; Grolimund, D.; Borca, C. N., A micro-XAS/XRF and thermodynamic study of CeIII/IV speciation after long-term aqueous alteration of simulated nuclear waste glass: Relevance for predicting Pu behavior? *Applied Geochemistry* **2012,** *27*, (1), 56-63.

[26] Grolimund, D.; Senn, M.; Trottmann, M.; Janousch, M.; Bonhoure, I.; Scheidegger, A. M.; Marcus, M., Shedding new light on historical metal samples using micro-focused synchrotron X-ray fluorescence and spectroscopy. *Spectrochimica Acta Part B: Atomic Spectroscopy* **2004,** *59*, (10–11), 1627-1635.

[27] Fitch, A. N.; Cole, M., The structure of $KUO_2PO_4 \cdot 3D_2O$ refined from neutron and synchrotron radiation powder diffraction data. *Materials Research Bulletin* **1991,** *26*, (5), 407-414.

[28] Krupka, K. M.; Parkhurst, M. A.; Gold, K.; Arey, B. W.; Jenson, E. D.; Guilmette, R. A., Physicochemical characterisation of capstone depleted uranium aerosols III: Morphological and chemical oxide analyses. *Health Physics* **2009,** *96*, (3), 276-291.

[29] Bonino, O.; Dugne, O.; Merlet, C.; Gat, E.; Holliger, P.; Lahaye, M., Study of surface modification of uranium and UFe_2 by various surface analysis techniques. *Journal of Nuclear Materials* **2001,** *294*, (3), 305-314.

[30] Le Bail, A.; Duroy, H.; Fourquet, J. L., Ab-initio structure determination of $LiSbWO_6$ by X-ray powder diffraction. *Materials Research Bulletin* **1988,** *23*, (3), 447-452.

[31] Meneghini, C.; Dalconi, M. C.; Nuzzo, S.; Mobilio, S.; Wenk, R. H., Rietveld Refinement on X-Ray Diffraction Patterns of Bioapatite in Human Fetal Bones. *Biophysical journal* **2003,** *84*, (3), 2021-2029.

[32] Peterson, V. K., Lattice parameter measurement using Le Bail versus structural (Rietveld) refinement: A caution for complex, low symmetry systems. *Powder Diffraction* **2005,** *20*, (01), 14-17.

[33] Ross, V., Studies of uranium minerals 21. Synthetic hydrogen-autunite. *American Mineralogist* **1955,** *40*, (9-10), 917-919.

[34] Hudson, E. A.; Rehr, J. J.; Bucher, J. J., Multiple-scattering calculations of the uranium L3 edge x-ray-absorption near-edge structure. *Physical Review B* **1995,** *52*, (19), 13815-13826.

[35] Farges, F.; Ponader, C. W.; Calas, G.; Brown, G. E., Structural environments of incomptabile elements in silicate glass melt systems 2. U^{IV}, U^{V} and U^{VI}. *Geochim. Cosmochim. Acta* **1992,** *56*, (12), 4205-4220.

[36] Frohlich, D. R.; Amayri, S.; Drebert, J.; Grolimund, D.; Huth, J.; Kaplan, U.; Krause, J.; Reich, T., Speciation of Np(V) uptake by Opalinus Clay using synchrotron microbeam techniques. *Analytical and Bioanalytical Chemistry* **2012,** *404*, (8), 2151-2162.

[37] Kelly, S.; Hesterberg, D.; Ravel, B., Analysis of soils and minerals using X-ray absorption spectroscopy. *Methods of soil analysis. Part* **2008,** *5*, 387-463.

[38] Brown, I. D.; Altermatt, D., Bond-valence parameters obtained from a systematic analysis of the Inorganic Crystal Structure Database. *Acta Crystallographica Section B* **1985,** *41*, (4), 244-247.

Chapter 6

Remediation of soils contaminated with particulate depleted uranium by multi stage chemical extraction[3]

6.1 Introduction

The development and deployment of armour piercing depleted uranium (DU) munitions has left a legacy of contaminated land in conflict areas and at test sites [1]. These areas may require long-term management and in some cases decontamination could be necessary to release the land for further use, or minimise risks to public health and environmental quality.

When a DU penetrator strikes an armoured target, 10-35% (maximum ~70%) of the mass is converted to aerosol [2] with median aerodynamic diameter of d < 15μm [3]. Uranium metal used in DU munitions is pyrophoric and oxidation of fragments and aerosols occurs on impact, typically producing UO_2 and U_3O_8 as the dominant species [4-7]. These oxidised particles settle in the surface environment close to DU impact sites, and have been observed in soils from Kosovo and Kuwait [8, 9] as well as at test firing ranges [7]. DU is also introduced into the environment as intact penetrators which undergo corrosion [10], and in accidents such as fires [6]. This study focuses on the remediation of soils contaminated with DU impact particles, which due to their prevalence in the near surface represent the most likely route of near-term exposure for populations [11].

The effective remediation of land contaminated with DU particles is an on-going challenge. If contamination is heavy, e.g. at US army firing ranges [12] and some accident sites in Kuwait [6], bulk soil is disposed of as radioactive waste. This involves considerable expense, and methods to decontaminate bulk soils and separate DU contamination into a smaller volume are

[3] This chapter has been prepared as a manuscript and accepted for publication in the *Journal of Hazardous Materials,* and is reproduced here under the creative commons attribution license (CC-BY). The published article can be found at http://dx.doi.org/10.1016/j.jhazmat.2013.08.013. All research work, manuscript and figure preparation was performed by the author of this thesis. Co-authors Francis Livens and Neil Hyatt are acknowledged for supervision and advisory input to the content and structure of the manuscript, Martin Stennett, Camelia Borca and Daniel Grolimund for assistance with performing synchrotron microanalysis experiments and Mustafa Sajih for assistance and discussions regarding autoradiography and SEM experimental design.

therefore attractive. Physical separation routes such as sieving have shown to be ineffective due to redistribution of U from weathering processes and agglomeration of DU aerosols [12]. Separation systems based on radioactivity are only useful for large fragments of penetrators due to the low specific activity of DU [13, 14]. Chemical extraction could overcome these limitations for aerosol contamination by leaching DU phases from the soil. There are reports of effective chemical leaching of DU munitions contamination [15-17] – however, this has only been applied to a small number of sites and more comprehensive data on the effectiveness of chemical extraction to DU dusts across a range of environments is required. In this study chemical extraction is evaluated as a decontamination approach for two DU laden soils from a UK firing range at Eskmeals [7, 18].

Decontamination by soil leaching has its basis in extraction of U from ores, where sulfuric acid or bicarbonate are common leaching agents [17, 19]. Additionally, citric acid has been studied due to its strong aqueous complexation of uranyl (UO_2^{2+}) [20], low toxicity, low cost compared to other organic extractants [21], and potential for controlled degradation [22, 23]. Under alkaline conditions, bicarbonate is modestly selective for uranium and causes less mobilization of other metals (e.g. Fe, Zn, Mn) from soils than under acidic conditions [17, 22]. Reported efficiencies for carbonate extraction range from 20 – 95% of total soil DU [15, 24] depending on the site, demonstrating that local geochemical conditions influence the leaching performance. Site specific DU extraction by citric acid has a comparably wide range in efficiency (25 - 99% total soil U) [15, 22], and sulphuric acid has also shown to be effective across a small number of sites [17].

In this study, the efficiency of chemical extraction for decontamination of DU munitions particulate at two sample sites from a UK firing range was evaluated. The aim was to use microscopic techniques for particle characterisation alongside bulk scale extraction experiments to provide a basis for improving the efficiency of extraction by process modifications. Particles from these sites were characterised prior to treatment by scanning electron microscopy (SEM) and sequential extraction to provide information on the initial geochemical disposition of U at

these sites. Following batch extraction, remaining particles were non-destructively characterised by SEM and synchrotron X-ray micro-spectroscopy and micro-diffraction. These techniques were used probe U behaviour in residues, and thus link residue particle properties with extraction efficiency. These data were then used to develop a more effective extraction methodology.

6.2 Experimental Methodology

6.2.1. Site and Soil Sampling

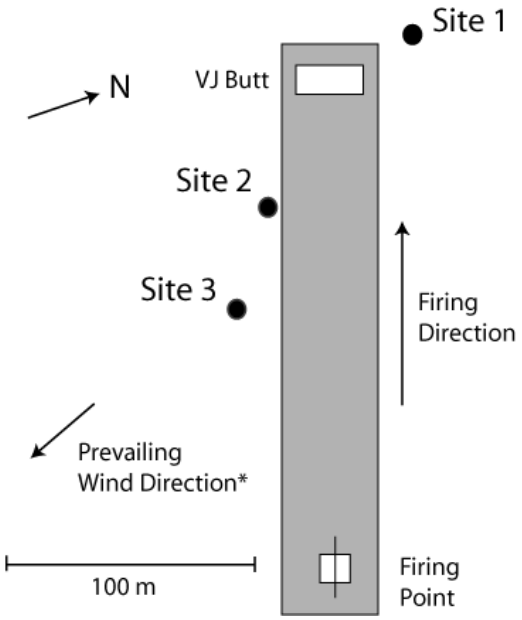

Figure 6.1 – Schematic of sampling locations within the VJ facility at MOD Eskmeals. The target and firing point are on a concrete apron. *Prevailing wind direction adapted from Oliver *et al*. [18].

Eskmeals in Cumbria, NW England, is a UK Ministry of Defence (MOD) firing range that was used in the development and testing of DU weapons from the 1960s to 1995. The area around the DU firing range (named the VJ facility) was exposed to fragments and aerosols from impacts, and approximately 3 ha is designated as a Controlled Radiation Area [18]. Soils from the site are useful for a remediation case study as contamination at the site has been well

characterised, is relatively undisturbed due to the restricted access and results from a constant, controlled firing direction [7, 18, 25].

Samples of soils from within the VJ radiation control area at MOD Eskmeals were collected in November 2011. Sampling was conducted in three areas (Figure 6.1); Site 1 is a storage area for contaminated timbers used in the construction of targets, Site 2 is adjacent to a concrete apron area downwind from the target, and Site 3 comprises a spoil heap of disturbed sub-soil from post operational construction at the site. In all cases surface vegetation was removed and soil to a depth of 0.15 m from an area of approximately 0.05 m^2 (total soil volume ~3 L) was sampled into plastic bags, which were sealed for transfer to the laboratory.

All samples were air dried at 40 °C and sieved to remove particles above 2 mm. The remaining soil was homogenised by hand, divided into representative portions using the cone and quarter method, and dry stored in sealed containers under ambient conditions. DU particles were localised for spectroscopy and microscopy using a sample splitting technique and autoradiography [7]. Soil pH was measured in 1:5 soil:water extracts shaken for 2 hours [18] using a WTW pH 315i (Expotech).

6.2.2. Sequential Extraction

The sequential extraction procedure follows the BCR scheme [26] as it has been previously applied to uranium speciation in soils [25-27]. The BCR scheme has three steps in which the speciation of the element of interest is defined as exchangeable, reducible and oxidisable [26]. The residual material is then analysed by total digestion or aggressive acid leaching to determine the mass balance.

Here the residual phase was evaluated by repeated digestion in hot nitric acid. Triplicate 1 g samples of dried soil from site 1 and site 2 were studied for U partitioning (Table 6.1). After each extraction step, the sample was centrifuged for 40 mins at 4000*g,* the supernatant taken to dryness and then made up to 5ml in 2% HNO_3. Total DU soil concentration was evaluated by

subjecting triplicate 1 g samples of fresh soil to step 4 only, as described previously [7, 28]. All extraction phase U concentrations were determined by ICP-AES.

Table 6.1 – Sequential extraction reagents and conditions. For more detail, see the BCR extraction scheme as described by Ure *et. al.* [26].

Step	Extraction Procedure
1 – Exchangeable	40 ml 0.11 mol/l acetic acid, 5 h.
2 - Fe/Mn Bound	40 ml 0.1 mol/l $NH_2OH{\cdot}HCl$ acidified to pH = 2 with conc. HNO_3, 16 h.
3 – Oxidisible	10 ml 30% w/v H_2O_2, 1 h at room temperature and 1h at 85^{o}C. Solution taken to dryness and repeated. Residue reacted overnight with 50 ml ammonium acetate, acidified to pH = 5 with conc. acetic acid.
4 – Residual	10 ml 8M HNO_3 at 80^{o}C for 4 h. Residue taken to dryness and repeated.

6.2.3. Batch leaching

Dried soil was subsampled using the cone and quarter method and a mass of 1 g taken for each leaching experiment. Initial soil activity was determined by autoradiography. Triplicate 10ml leaching experiments were prepared with solutions of 0.5M NH_4HCO_3, 0.1M citric acid and 0.1M H_2SO_4, conducted in sealed 50 ml vials with an air headspace. Samples were left to react for one week at ambient temperature with agitation on a shaker table. After reaction, the supernatant was separated from bulk soil by filtration, followed by acidification to pH 2 with concentrated nitric acid and analysis by ICP-AES. Residual soils were dried and remaining soil activity was determined by autoradiography. For site 1 samples, the residue from batch extraction was subject to step 4 (Residual) as described above.

6.2.4. Solid and Liquid Uranium Concentration Analyses

Bulk soil activity was determined non-destructively by autoradiography. 1 g soil samples were spread onto 8 cm diameter filter papers and exposed to a phosphor storage screen for 21 h, and the screen read using a phosphor imager (Typhoon Imager, GE Healthcare). The pixel intensity across each sample was summed, along with an equivalent background region of the plate, allowing estimation of total radioactivity. This process was repeated before and after remediation experiments. The decontamination factor, as used here, is defined as the amount of radioactivity (determined by autoradiography) removed from soil divided by the initial activity, and is equal to 1 for complete decontamination, and zero for no decontamination. The decontamination factor was also calculated using extracted U mass in the leachate and residual U mass by acid digestion (Step 4, Table 6.1) for site 1 samples. Good agreement between yields measured by these two techniques was observed.

Leachate uranium concentrations were analysed by inductively coupled plasma atomic emission spectroscopy (ICP-AES) on a Perkin-Elmer Optima 5300 dual view ICP-AES. Standards were analysed at 0.1, 0.5, 1 and 10 ppm U, prepared by dilution of a 1000 ppm standard solution (Sigma Aldrich, UK). Matrix matched samples for each remediation experiment were analysed at 1, 5 and 10ppm. Analysed U standards were within 3% of the expected value.

6.2.5. Environmental Scanning Electron Microscopy (ESEM)

Scanning electron microscopy was used to investigate particle morphology and composition. Samples were mounted on adhesive carbon pads and were not coated prior to analysis. The ESEM (FEI XL30) was used in high vacuum with accelerating voltage of 15kV with back-scattered electron (BSE) imaging to identify areas of high atomic number elements. The composition of high-Z particles identified by BSE imaging was investigated using Energy Dispersive X-Ray (EDX) analysis.

6.2.6. μ-XRF, μ-XRD and μ-XANES

Synchrotron radiation microfocus X-ray analyses were conducted at the MicroXAS (X05LA) beamline at the Swiss Light Source (SLS). The photon energy range is 4 – 23 keV, and the

beam line can deliver monochromatic X-rays by means of a Si (1 1 1) double crystal monochromator. In these experiments, the spot size was approximately 5 μm (h) x 2 μm (v). Samples were mounted on a motorised x-y-z stage which allows scanning in the beam for mapping. The stage was positioned at a 25° angle to the incident beam. Samples were mounted on carbon pads or Kapton tape.

X-ray fluorescence (XRF) was measured using a Si(Li) detector (KETEK) mounted at 45° to the sample stage. XRF spectra were monitored to localise particles containing U in the beam for analysis. X-ray diffraction (XRD) was measured using a PILATUS 100K hybrid pixel array detector [29] mounted 46 mm behind the sample, with a tungsten beamstop in place. The detector tilt and distance to the sample were calibrated by measurement of a silicon standard (NIST 640c). Phases were identified with reference to the ICSD PDF-2 database records, and the record numbers are given in the corresponding figures. The experimental setup was chosen such that XRF and XRD measurements could be made concurrently, with a monochromatic beam of energy 17.300 keV (λ = 0.7167 Å). Uranium L_{III} edge (E_0 = 17.166 keV) XANES (X-ray absorption near edge structure) spectra were recorded in fluorescence mode by recording the U Lα emission (13.614 keV) and tuning the monochromator energy from 16.900 to 17.500 keV. Energy calibration was performed with respect to the K-edge of a yttrium foil (17.038 keV) and fluorescence XANES spectra of standards of UO_2, U_3O_8 and UO_3 were also recorded.

6.3. Results and Discussion

6.3.1. Soil Characterisation

6.3.1.1 Bulk Soil Properties

A soil sample from a nearby soil horizon was characterised for local bulk soil characteristics including mass particle size distribution, cation exchange capacity, and total organic carbon using standard techniques (Table 6.2) [30]. Soils from the area are characterised as raw dune

sands [7, 18]. Site 1 soil pH was 5.5, Site 2 was 7.6 and Site 3 was 6.5. These agree well with previously published soil pH data in the range 5.6 - 7.8 [18] for the Eskmeals site.

Table 6.2 – Bulk soil particle size distribution and organic carbon for Eskmeals area soil. The soil total bulk organic carbon was 0.2%, and cation exchange capacity (CEC) was determined as 0.6 Meq / 100 g.

Size Fraction (μm)	% Mass Abundance	% Organic Carbon
250-2000	2.1	1.5
125-250	87.7	0.03
63 – 125	7.8	0.2
32-63	0.7	1.1
2 – 32	1.4	6.4
< 2	0.2	10.6

6.3.1.2. Total Uranium

Soils from sample site 1 have the highest level of contamination (320 ± 40 mg U/kg), with approximately an order of magnitude greater uranium burden than sample site 2 (37 ± 4 mg U/kg). Background concentrations of U around the site are reported between 0.2 – 1.7 mg U/kg [25], close to that measured at site 3 (2.2 ± 0.5 mg U/kg). The higher concentration in site 1 soils is probably linked to the storage of heavily contaminated timbers from the target hutch, whereas site 2, located downwind from the target, is more typical of DU contamination arising from settling and scattering of impact particles [9].

Site 2 is in a similar location to "Pad Edge" samples studied previously [18], and the U concentration is of similar magnitude to the reported concentrations in the range 60.8 – 72 mg U/kg [18, 25, 31]. Higher concentrations and large variation reported in some sample sites close to the firing Pad Edge ("Pad Edge A" – 282 ± 142 mg U/kg [18]) were not observed in this study, which suggests that the pattern of contamination at the site is highly spatially heterogeneous, with localised "hot-spots" of elevated DU concentration.

6.3.1.3. Scanning Electron Microscopy

Electron microscopy was used to study the morphology, microstructure and elemental composition of DU aerosol particles in the soil samples. Features which appeared bright in back-scattered electron (BSE) imaging were examined for elemental composition by EDX analysis.

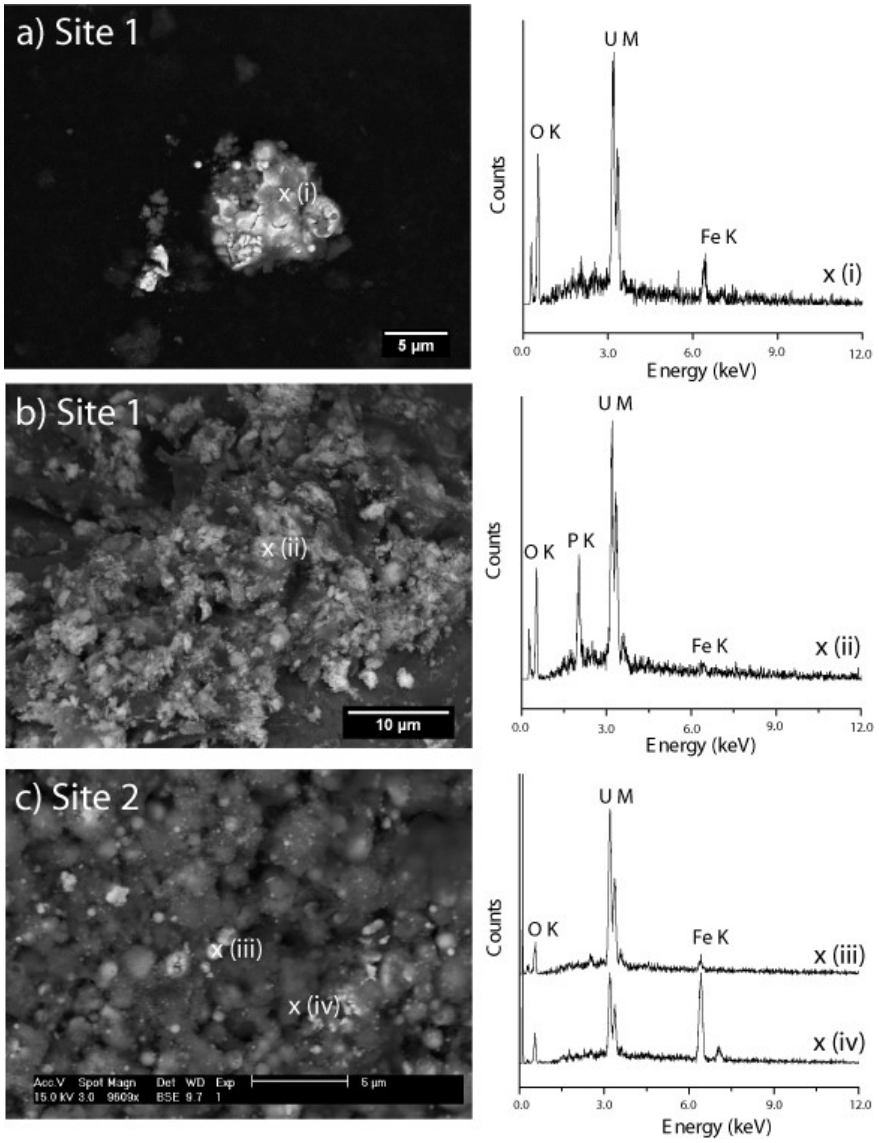

Figure 6.2 – Backscattered micrographs and EDX spectra of DU particles present in Eskmeals soil from sample site 1 (a,b) and sample site 2 (c). DU rich particles appear brightly in BSE imaging, and the presence of U in these areas was verified by spot EDX analysis. The X in micrographs shows the position of the electron probe during EDX data collection.

Aerosol particles produced by U impact often have a characteristic spherical primary morphology linked to melting of metallic U during high temperature impact events [4]. Particles with this characteristic morphology were observed in soils from both sample sites (Figure 6.2). The size range, morphology and elemental composition of particles observed in this study are broadly similar to those observed in live firing tests [4, 32] and from conflict zones [5, 6, 33]. In addition, U-rich areas with platy crystal habit were observed in soils from site 1 (Figure 6.2b) suggesting formation of secondary phases as a result of particle weathering, consistent with characterisation of these soils in Chapter 4.

In some cases, large numbers of DU particles were observed adhered to larger (< 200 μm) silicon-rich particles, probably sand grains, the surface of which is shown in Figure 6.2c. This is a complicating factor for remediation by physical separations such as sieving – although DU particles have a characteristic size range (<15 μm, [3]), adhesion processes make it impossible to effectively separate these particles in soil fines fractions, which may explain the poor reported performance of particle size based physical separation processes for DU decontamination [12].

6.3.1.4. Sequential Extraction

The fraction of U extracted in each step of the sequential BCR scheme is similar in both soils (Figure 6.3), despite an order of magnitude difference in the total U concentration. This indicates that at both sites the bulk geochemical behaviour of the DU contamination is similar; with most of the inventory partitioning into BCR defined oxidisable and residual phases. These phases require aggressive extraction conditions for solubilisation, indicating that the majority (~75%) of the U inventory is chemically resistant to dissolution.

Although the BCR oxidisable soil fraction is normally interpreted as species bound to sulphides or organic matter [26], this interpretation is not valid for samples containing U(IV)-oxide phases, which are readily solubilised by H_2O_2 [19]. As primary particle morphologies are observed in both site soil samples (Figure 6.2), it would be expected that a substantial fraction

of primary U(IV) phases persists in these soils, consistent with the abundance of oxidisable uranium at both sample sites.

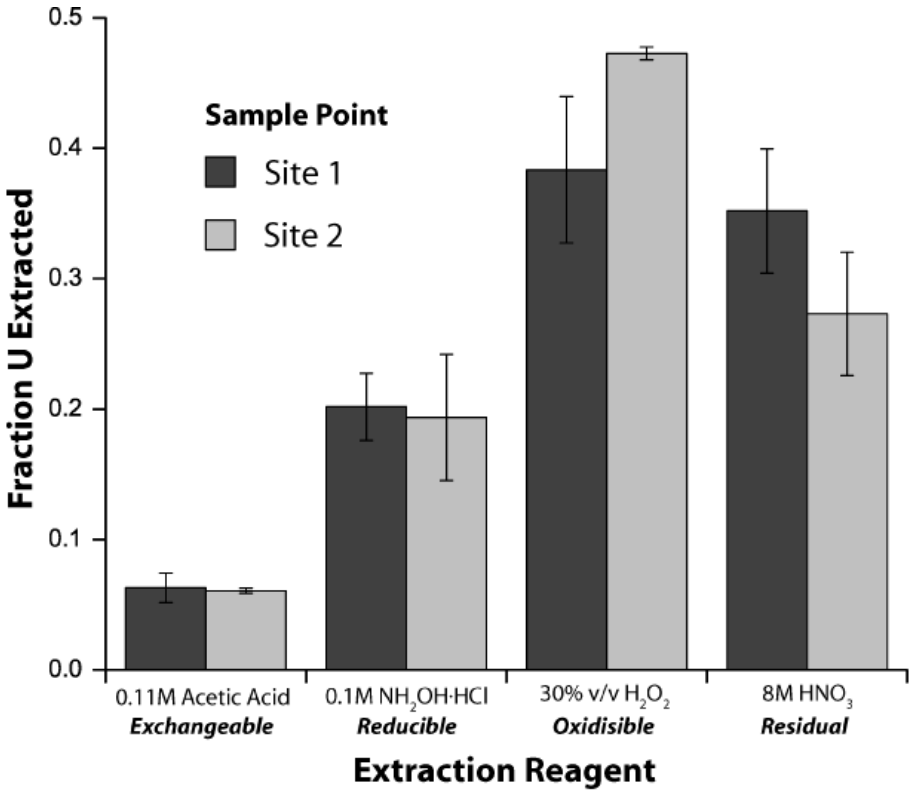

Figure 6.3 – U fractionation between operationally defined speciation classifications for two soils at the Eskmeals site. Total U is 320 ± 40 mg / kg for Site 1, and 37 ± 4 mg / kg for Site 2. Error bars are one standard deviation of triplicate analyses.

The presence of U extracted in exchangeable and reducible fractions suggests that some U(VI) alteration products are present, as U(IV) oxides exhibit low solubility in non-oxidising acids such as acetic acid and with reducing agents such as $NH_2OH{\cdot}HCl$. U(VI) oxy-hydroxide species are a typical corrosion product of DU(IV) phases in oxic surface moist environments [34] and are readily solubilised by acetic acid [35], and may account for the minor (6%) exchangeable fraction of the U inventory. The reducible soil fraction accounts for U bound to poorly crystalline Fe/Mn phases, and comprises approximately 20% of the total U at both sites. Processes such as sorption and co-precipitation of U(VI) with Fe(III) hydrous oxides, which can occur in U contaminated environments, would produce a 'reducible' extraction inventory of U in these soils [36]. Although there are uncertainties in the selectivity of BCR extraction

reagents, the results for the exchangeable and reducible fractions give a first order estimate of the extent of labile U(VI) species as approximately 25%.

6.3.2. Remediation of Contaminated Soils by Chemical Extraction

6.3.2.1. Batch Extraction

Table 6.3 – Remediation extraction data for DU in sample site 1 and sample site 2 soils exposed to 0.1M Citric Acid, 0.1M H_2SO_4 and 0.5M NH_4HCO_3. The decontamination factor is defined as the amount of net radioactivity (for autoradiography data) or uranium mass (for ICP-AES data) removed as a fraction of the total net radioactivity or uranium mass. Error estimates are ± 1 standard deviation of triplicate analyses.

		Extraction Reagent		
		0.1M Citric Acid	0.1M H_2SO_4	0.5M NH_4HCO_3
Sample Site 1	Decontamination Factor[a]	0.30 ± 0.1	0.2 ± 0.05	0.4 ± 0.1
	U extracted[b] (µg)	135 ± 28	80 ± 31	173 ± 35
	U remaining[c] (µg)	172 ± 27	286 ± 37	165 ± 29
	Decontamination Factor[c]	0.4 ± 0.1	0.2 ± 0.1	0.5 ± 0.1
Sample Site 2	Decontamination Factor [a]	0.4 ± 0.1	0.1 ± 0.1	0.5 ± 0.2
	U extracted[b] (µg)	23 ± 3.9	7.5 ± 2.8	29 ± 12

a – Determined by autoradiography

b – Determined by ICP-AES measurement of the leachate

c – Determined by nitric acid digestion of the residual soil.

Batch remediation data for sample site 1 and sample site 2 are shown in Table 6.3. The mass of U extracted from 1g soil samples is measured from the leachate U concentration, determined by ICP-AES. The trend in U mass (μg) extracted agrees well with the autoradiography decontamination factor.

The data indicate that ammonium bicarbonate is the most effective extractant. Extraction in citric acid is somewhat less effective (~20%), and dilute sulfuric acid has the lowest extraction efficiency. Extraction efficiencies are similar across both sample sites, which is consistent with similarities in sequential extraction data (Figure 3). Reasonable agreement was also observed between decontamination factor determined by autoradiography and dissolution of residual soils (Table 6.3), with the same trend in extraction efficiencies observed in both data.

These data show that chemical extraction can remove substantial portions of munitions DU from soils, but that additional optimisation would be required to achieve complete decontamination. The amount of DU removed is comparable to similar extractions performed on contaminated soils from a US military site, in which decontamination factors for citric acid range from 0.35 to 0.6 and from 0.3 to 0.6 for bicarbonate, with ambient dissolved oxygen as the oxidising agent [15]. The good agreement with previously reported extraction efficiency suggests that this approach may be applicable to other instances of depleted uranium contamination.

6.3.2.2. Residual particle analysis

The decontamination factor is determined non-destructively by autoradiography, allowing the treated soil to be recovered for analysis. In order to optimise and improve the process, information on the U phases which remain after extraction is required.

A repeat set of dried bicarbonate treated soil samples from site 1 were examined by autoradiography, which revealed that particulate residues were still present. Particles from this test were selected as bicarbonate offers the most effective U extraction, and site 1 had the highest U concentration and lower decontamination factors than site 2. The separated particles

were analysed by electron microscopy, microfocus-XRD and microfocus-XANES at the U-L_{III} edge.

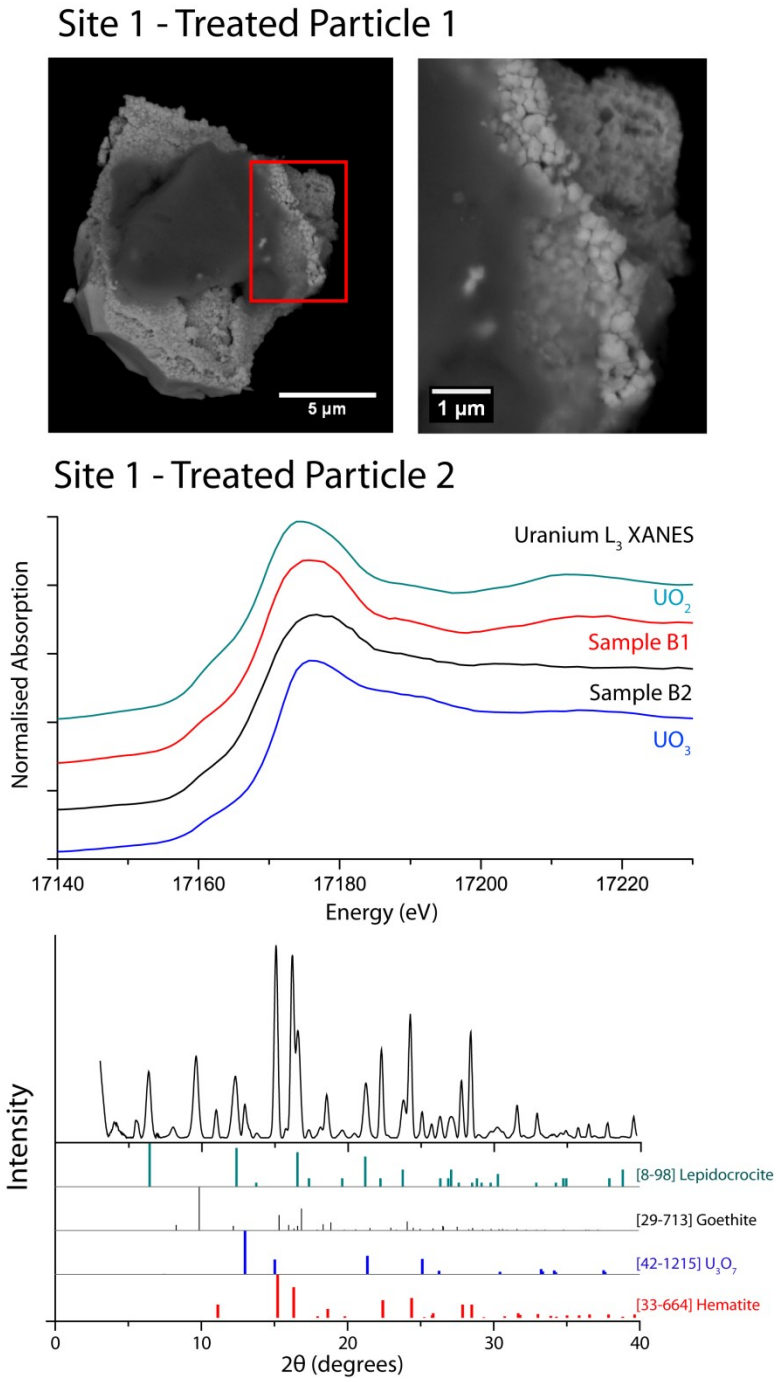

Figure 6.4 – Backscattered electron micrographs (treated particle 1), XANES spectra and XRD pattern with corresponding ICSD PDF-2 database numbers (treated particle 2) of residual primary particles. The micrographs show morphology suggestive of a partially leached oxide particle, including grain boundary etching. This is supported by XRD and XANES analyses showing the presence of U_3O_7 and U(IV) in some soil residues.

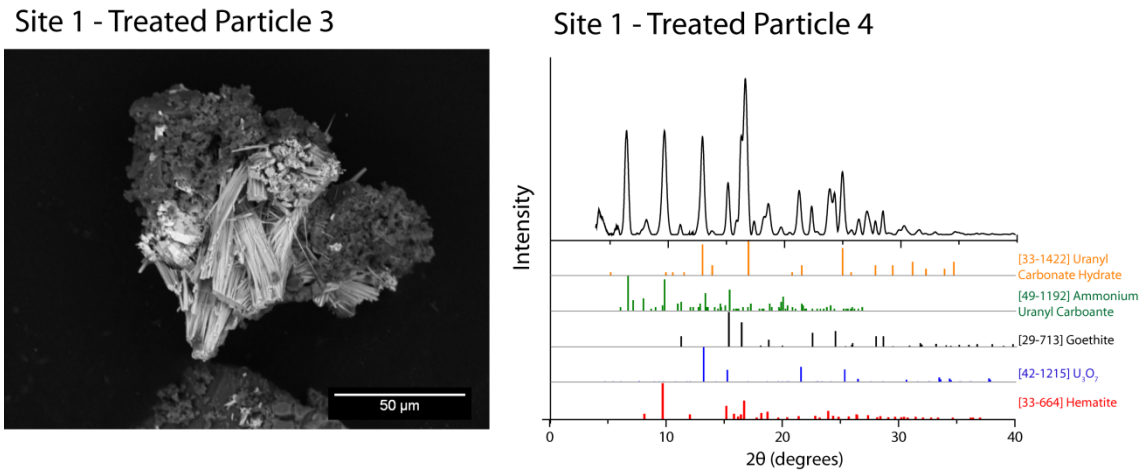

Figure 6.5 – Electron micrograph of particle showing acicular crystal habit (treated particle 3) consistent with uranyl-carbonate species, and powder XRD pattern with corresponding ICSD PDF-2 database numbers from a different particle (treated particle 4), showing the presence of two uranyl carbonate phases.

Electron micrographs reveal two distinct particle morphologies, one group consistent with primary aerosol particles (Figure 6.4), and a second group which has a structure suggestive of secondary phase formation (Figure 6.5). Indications of dissolution are observed in primary particles, in particular preferential grain boundary dissolution evident in the etched grain structure in Figure 6.4. This phenomenon is also observed in the oxidative dissolution of unburnt civil nuclear fuel grade UO_2 [37]. The modification of the particle microstructure indicates that some dissolution occurs, but not to completion on the timescale of these batch experiments. XRD data are also consistent with the presence of unreacted primary species, as U is present as U_3O_7 which agrees well with comparable data from untreated particles at the Eskmeals site [7].

Micro-XANES data show that the predominant oxidation state in the samples is U(IV), as spectra edge shifts, white line positions and post edge oscillations are similar in character to the UO_2 standard (Figure 6.4). This is consistent with XRD data showing U_3O_7, and previous studies of DU particulate which show U to be present as U(IV) in untreated particles [5, 6]. The conservation of primary oxide species and evidence of partially leached microstructure suggests

that although these phases are amenable to carbonate extraction, they are dissolved slowly, requiring longer than the experimental timescale for complete dissolution.

The second morphology is not observed in untreated material. U-rich particles with an acicular habit (Figure 6.5) are consistent with the formation of uranyl-carbonate secondary phases [38]. XRD analysis confirms the presence of uranyl carbonate hydrate phases and ammonium uranyl carbonate, the latter presumably due to the high concentration of ammonium in the 0.5M NH_4HCO_3 primary leaching solution.The formation of secondary phases may explain the slightly reduced extraction efficiency in site A soils (Table 6.3), and it is probable that this process will be an important control on extraction efficiency in highly contaminated soils.

6.3.3. Alternating Batch Extraction

The presence of secondary uranyl carbonate hydrate phases suggests that a single batch extraction is not the best approach for removing as much DU as possible from Eskmeals soils, and an alternating basic/acid washing procedure could improve extraction by rapidly dissolving secondary phases.

The results of a three-step bicarbonate/citric acid/bicarbonate leaching process are presented in Figure 6.6. The first step extraction in NH_4HCO_3 removes around 50% of the uranium inventory at both sites, as expected from the single step bicarbonate leaching tests. For the second extraction in 0.1M citric acid, additional uranium is removed from site 1 samples, but negligible uranium is released from site 2 soils. This may reflect a larger mass of secondary uranyl carbonate hydrate phases in site 1 samples, which are then dissolved by step 2 acidic conditions.

An additional bicarbonate step was trialled to test the susceptibility of residual particles to further leaching. In both sites, a second bicarbonate extraction resulted in the removal of additional uranium from the soils. This suggests that different fractions of the DU inventory are accessible to different leaching reagents, and that bicarbonate extraction is more effective at removing residual phases from both site soils. The total uranium removed as a percentage of the

initial activity in the three step leaching process was 68 ± 14% for site 1 and 87 ± 7% for site 2, which represents a substantial improvement on single step leaching.

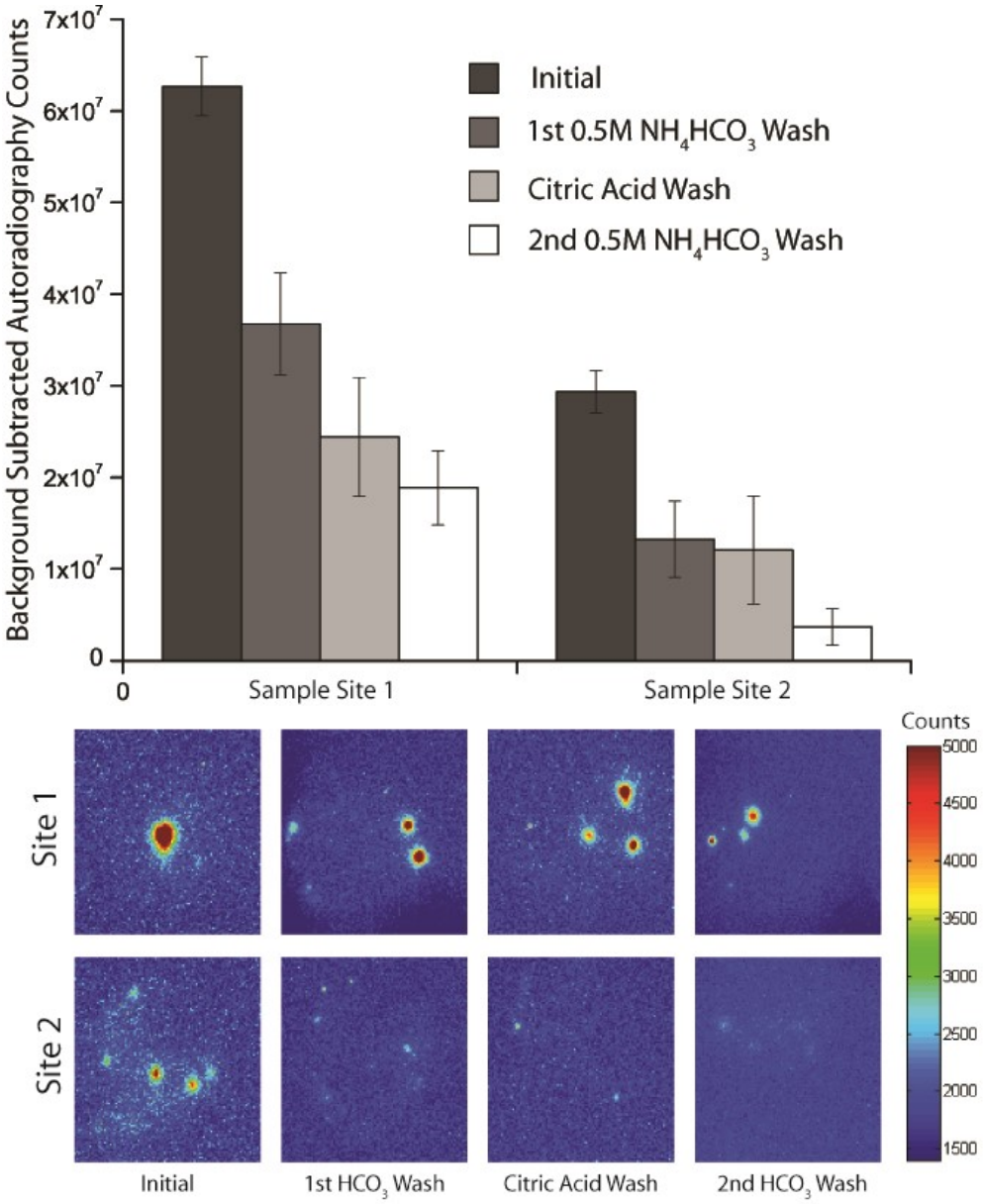

Figure 6.6 – Net soil radioactivity and representative autoradiographs of soils extracted in a three step sequential batch extraction scheme.

Representative autoradiographs of soil samples from each site are presented in Figure 6.6. This technique allows the dissolution of particles to be tracked across each extraction stage. The autoradiographs of site 1 soils show that large agglomerate particles are readily broken down and slowly leached during multi-stage extraction, whereas smaller particles in site 2 soil are

dissolved more rapidly. The decreasing activity of the fragments in sample 1 between washes suggests that these particles would eventually be completely dissolved. These results demonstrate that enhanced recovery of uranium from these firing range soils can be achieved in batch systems by applying a multi-stage leaching approach.

6.4. Conclusions

Characterisation of depleted uranium in firing range soils through a combination of microscopic and bulk chemical techniques demonstrates that much of the material persists in primary forms which partition into chemically resistant soil fractions. These findings are consistent with other studies of particles from DU munitions firing, and indicate that this site is a reasonable case study for remediation of DU contaminated soils.

Single step batch extraction demonstrated that low cost, environmentally compatible reagents such as ammonium bicarbonate and citric acid could be applied to effect 40-50% decontamination in small batches of firing range soils, although it remains to be seen if this efficiency carries through to a larger scale. In some cases, this extent of decontamination may be sufficient to allow alternative, less costly management options for contaminated sites, and hence the investigation of larger scales of operation will be of interest. However, this approach still leaves residual particulate material behind and there is long term uncertainty over the geochemical behaviour and fate of residual DU particles in soil.

Secondary phase formation was observed in NH_4HCO_3 extracted soils, and an extended batch washing procedure was trialled involving alternate washes with bicarbonate and citric acid reagents. This approach successfully removes additional DU from soils, leading to improved (up to 87% removal) efficiency in decontamination. Additional repeat washing in this way begins to approximate an alternating continuous flow system in which the contaminated soil is continually treated with fresh extraction reagent. Such a system may prove more flexible for engineering scale application than alternate batch washing, and future work to improve DU extraction efficiency should investigate continuous flow systems.

6.5 Acknowledgements

Paul Lythgoe (University of Manchester) is thanked for collection of ICP-AES data. Tim Geer (QinetiQ) and Catherine Toque (DSTL) are thanked for assistance with gaining site access to Eskmeals and soil sampling.

6.6 References

[1] The Royal Society, The health hazards of depleted uranium munitons - Part 1: Policy Document 6/01, **2002.**

[2] N. Harley, E. Foulkes, L.H. Hilborne, A. Hudson, C.R. Anthony, A review of the scientific literature as it pertains to gulf war illnesses: volume 7: depleted uranium, RAND Corporation, **1999.**

[3] Y.S. Cheng, J.L. Kenoyer, R.A. Guilmette, M.A. Parkhurst, Physicochemical characterization of capstone depleted uranium aerosols II: particle size distributions as a function of time, *Health Phys.* **2009**, *96*, 266-275.

[4] K.M. Krupka, M.A. Parkhurst, K. Gold, B.W. Arey, E.D. Jenson, R.A. Guilmette, Physicochemical characterization of capstone depleted uranium aerosols III: morphologic and chemical oxide analyses, *Health Phys.* **2009**, *96,* 276-291.

[5] B. Salbu, K. Janssens, O.C. Lind, K. Proost, P.R. Danesi, Oxidation states of uranium in DU particles from Kosovo, *J. Environ. Radioact.* **2003**, *64,* 167-173.

[6] B. Salbu, K. Janssens, O.C. Lind, K. Proost, L. Gijsels, P.R. Danesi, Oxidation states of uranium in depleted uranium particles from Kuwait, *J. Environ. Radioact.* **2005***, 78,* 125-135.

[7] M. Sajih, F.R. Livens, R. Alvarez, M. Morgan, Physicochemical characterisation of depleted uranium (DU) particles at a UK firing test range, *Sci. Total. Environ.* **2010**, *408,* 5990-5996.

[8] O.C. Lind, B. Salbu, L. Skipperud, K. Janssens, J. Jaroszewicz, W. De Nolf, Solid state speciation and potential bioavailability of depleted uranium particles from Kosovo and Kuwait, *J. Environ. Radioact.* **2009***, 100,* 301-307.

[9] A. Bleise, P.R. Danesi, W. Burkart, Properties, use and health effects of depleted uranium (DU): a general overview, *J. Environ. Radioact.,* **2003**, *64,* 93-112.

[10] S. Handley-Sidhu, M.J. Keith-Roach, J.R. Lloyd, D.J. Vaughan, A review of the environmental corrosion, fate and bioavailability of munitions grade depleted uranium, *Sci. Total. Environ.* **2010***, 408,* 5690-5700.

[11] W.E. Briner, The evolution of depleted uranium as an environmental risk factor: lessons from other metals, *Int. J. Environ. Res. Public Health,* **2006**, *3,* 129-135.

[12] S. Larson, J. Ballard, V. Medina, M. Thompson, G. O'Connor, C. Griggs, C. Nestler, Separation of Depleted Uranium From Soil, *US Army Engineering Research and Development Centre, Vicksburg MS Environmental Labs*, **2009**.

[13] M. Miller, B. Galloway, G. VanDerpoel, E. Johnson, J. Copland, M. Salazar, An Alternative for Cost-Effective Remediation of Depleted Uranium (DU) at Certain Environmental Restoration Sites, *Health Phys.* **2000***, 78,* S9-S12.

[14] C.P. Farr, T.J. Alecksen, R.S. Heronimus, M.H. Simonds, D.R. Farrar, M.L. Miller, K.R. Baker, Recovery of Depleted Uranium Fragments from Soil, *Health Phys.* **2010***, 98,* S6-S11

[15] C.C. Choy, G.P. Korfiatis, X.G. Meng, Removal of depleted uranium from contaminated soils, *J. Hazard. Mater.* **2006***, 136,* 53-60.

[16] C.F.V. Mason, W. Turney, B.M. Thomson, N. Lu, P.A. Longmire, C.J. ChisholmBrause, Carbonate leaching of uranium from contaminated soils, *Environ. Sci. Technol.* **1997***, 31*, 2707-2711.

[17] M.C. Duff, C.F.V. Mason, D.B. Hunter, Comparison of acid and base leach for the removal of uranium from contaminated soil and catch-box media, *Can. J. Soil Sci.* **1998***, 78,* 675-683.

[18] I.W. Oliver, M.C. Graham, A.B. MacKenzie, R.M. Ellam, J.G. Farmer, Assessing depleted uranium (DU) contamination of soil, plants and earthworms at UK weapons testing sites, *J. Environ. Monit.* **2007**, *9*,740-748.

[19] M. Gavrilescu, L.V. Pavel, I. Cretescu, Characterization and remediation of soils contaminated with uranium, *J. Hazard. Mater.* **2009***, 163,* 475-510.

[20] J.J. Lenhart, S.E. Cabaniss, P. MacCarthy, B.D. Honeyman, Uranium(VI) complexation with citric, humic and fulvic acids, *Radiochim. Acta* **2000***, 88,* 345-353.

[21] N. Lu, K.S. Kung, C.F.V. Mason, I.R. Triay, C.R. Cotter, A.J. Pappas, M.E.G. Pappas, Removal of plutonium-239 and americium-241 from rocky flats soil by leaching, *Environ. Sci. Technol.* **1998***, 32,* 370-374.

[22] A.J. Francis, C.J. Dodge, Remediation of soils and wastes contaminated with uranium and toxic metals, *Environ. Sci. Technol.* **1998***, 32,* 3993-3998.

[23] C.W. Francis, M.E. Timpson, J.H. Wilson, Bench- and pilot-scale studies relating to the removal of uranium from uranium-contaminated soils using carbonate and citrate lixiviants, *J. Hazard. Mater.* **1999***, 66,* 67-87.

[24] E.J.P. Phillips, E.R. Landa, D.R. Lovley, Remediation of uranium contaminated soils with bicarbonate extraction and microbial U(VI) reduction, *J. Indust. Microbiol.* **1995***, 14,* 203-207.

[25] I.W. Oliver, M.C. Graham, A.B. MacKenzie, R.M. Ellam, J.G. Farmer, Distribution and partitioning of depleted uranium (DU) in soils at weapons test ranges - Investigations combining the BCR extraction scheme and isotopic analysis, *Chemosphere* **2008***, 72*, 932-939.

[26] A.M. Ure, P. Quevauviller, H. Muntau, B. Griepink, Speciation of heavy-metals in soils and sediments - an account of the improvement and harmonization of extraction techniques

undertaken under the auspices of the BCR of the comission of the European communities, *Int. J. Environ. Anal. Chem.* **1993***, 51,* 135-151.

[27] S.E. Howe, C.M. Davidson, M. McCartney, Determination of uranium concentration and isotopic composition by means of ICP-MS in sequential extracts of sediment from the vicinity of a uranium enrichment plant, *J. Anal. At. Spectrom.* **2002***, 17,* 497-501.

[28] C.C.L. Toque, A.C. Baker, MOD DU Programme - Report on the corrosion of depleted uranium in the Solway Firth, *UK Defence Science and Technology Laboratory (DSTL)*, 8th August **2005** CR 11679 V2.0

[29] T. Taguchi, C. Broennimann, E.F. Eikenberry, Next generation X-ray detectors for in-house XRD, *Powder Diffr.* **2008***, 23,* 101-105.

[30] S.E. Allen, Chemical analysis of ecolgocial materials, *Wiley*, **1974**.

[31] S.R. Brittain, A.G. Cox, A.D. Tomos, E. Paterson, A. Siripinyanond, C.W. McLeod, Chemical speciation studies on DU contaminated soils using flow field flow fractionation linked to inductively coupled plasma mass spectrometry (FLFFF-ICP-MS), *J. Environ. Monit.* **2012**, 14, 782-790.

[32] V. Chazel, P. Gerasimo, V. Dabouis, P. Laroche, F. Paquet, Characterisation and dissolution of depleted uranium aerosols produced during impacts of kinetic energy penetrators against a tank, *Radiat. Prot. Dosim*. **2003**, 105, 163-166.

[33] P.R. Danesi, A. Markowicz, E. Chinea-Cano, W. Burkart, B. Salbu, D. Donohue, F. Ruedenauer, M. Hedberg, S. Vogt, P. Zahradnik, A. Ciurapinski, Depleted uranium particles in selected Kosovo samples, *J. Environ. Radioact.* **2003***, 64,* 143-154.

[34] S. Handley-Sidhu, P.J. Worsfold, F.R. Livens, D.J. Vaughan, J.R. Lloyd, C. Boothman, M. Sajih, R. Alvarez, M.J. Keith-Roach, Biogeochemical Controls on the Corrosion of Depleted Uranium Alloy in Subsurface Soils, *Environ. Sci. Technol.* **2009***, 43*, 6177-6182.

[35] W.H. Johnson, B.J. Buck, H. Brogonia, A.L. Brock, Variations in Depleted Uranium Sorption and Solubility with Depth in Arid Soils, *Soil and Sediment Contamination: An International Journal* **2004***, 13,* 533-544.

[36] M.C. Duff, J.U. Coughlin, D.B. Hunter, Uranium co-precipitation with iron oxide minerals, *Geochim. Cosmochim. Acta* **2002***, 66,* 3533-3547.

[37] D.J. Wronkiewicz, E.C. Buck, J.K. Bates, Grain boundary corrosion and alteration phase formation during the oxidative dissolution of UO_2 pellets, *MRS Proceedings* **1996,** *465*.

[38] R. Vochten, M. Deliens, O. Medenbach, Oswaldpeetersite, $(UO_2)_2CO_3(OH)_2 \cdot 4H_2O$, a new basic uranyl carbonate mineral from the jomac uranium mine, San Juan County, Utah, USA, *Can. Mineral.* **2001***, 39,* 1685-1689.

Chapter 7

Engineering biogenic magnetite for sustained Cr(VI) remediation in flow-through systems[4]

7.1 Introduction

Chromium contamination of waters and sediments is a worldwide problem arising from its widespread use in industrial processes including metal plating, alloying, leather tanning, and wood treatment. Chromium in the environment mainly exists in the Cr(III) or Cr(VI) oxidation states which exhibit different bioavailability, toxicity, and transport characteristics [1]. Trivalent chromium is relatively nontoxic [2] and considered an essential trace nutrient [3], whereas hexavalent chromium is a strong oxidizing agent, recognized as highly toxic and carcinogenic [4]. The risk from Cr(VI) toxicity is increased due to its typical speciation as weakly sorbing anionic chromate (CrO_4^{2-}) or dichromate ($Cr_2O_7^{2-}$), making it highly mobile in the environment [1, 5]. In contrast, Cr(III) is considered immobile due to the formation of insoluble oxyhydroxides and strong sorption to mineral surfaces [1]. The reduction of chromium from Cr(VI) to Cr(III) is an important reaction in reducing risk to environmental quality and human health posed by chromium contamination.

Iron(II)-bearing minerals have been shown to be effective at reducing a range of contaminants including Cr(VI) [5]. Magnetite [$Fe(II)Fe(III)_2O_4$] is a common mineral in the geosphere which has received significant attention as a natural reductant for chromium [6-10]. Biogenic magnetite can be synthesized by dissimilatory iron(III)-reducing bacteria (DIRB) respiring Fe(III) minerals [11]. From a remediation perspective, a key feature of biologically produced magnetite is its small particle size (20 to 30 nm) [12], which results in a large surface area for

[4]This chapter has been prepared as a manuscript and accepted for publication. Reprinted (adapted) with permission from *Environmental Science and Technology* **2012** 46 (6), 3352-3359. Copyright 2012 American Chemical Society. The research work was performed and manuscript prepared by the author of this thesis with co-authors Victoria Coker, who assisted with column experiments, fitting XPS and XMCD data, collection of STEM data and drafting of the manuscript, Gerrit Van der Laan, who performed Cr $L_{2,3}$ edge XAS calculations shown in Appendix 2 and Jonathan Lloyd, who supervised this project and provided advice to the structure and content of the manuscript.

sorption and subsequent reduction of contaminants. Biogenic magnetite can have greater than stoichiometric amounts of Fe(II) associated with a near surface layer [12, 13], and the amount of Fe(II) in magnetite greatly influences the rate and total amount of contaminant reduction [14, 15]. Harnessing biosynthetic routes for magnetite production has been considered more efficient and economical than conventional chemical techniques and results in a more effective material for reductive remediation than commercially available magnetite [16].

Recent developments in biogenic magnetite production have focused on optimizing the reductive capacity of biogenic magnetite by selection of Fe(III) starting materials [16] and precipitating precious metal particles, e.g. palladium, onto the surface to create magnetic nanocatalysts [12]. Biogenic magnetite is particularly attractive for functionalization due to the presence of an organic layer which facilitates attachment [12]. Although magnetite has been studied extensively as a remediation material [17], there have been limited attempts to understand the effect of co-contaminants which influence solution pH, redox potential and ionic strength. Chromate reduction by magnetite is governed by a sorption stage of Cr(VI) followed by reductive transformation to Cr(III) by Fe(II) [7, 18]. Modelling results suggest that Cr(VI) has intermediate affinity for oxide surfaces, and the influence of ionic strength will not be as dramatic as for weaker anions [19]. Previous studies have also found the ability of magnetite to remove Cr(VI) from solution reduces with increasing pH, related to passivation of the mineral surface [6, 18, 20]. In aerobic solutions the ability of magnetite to remove Cr(VI) from solution is impaired by oxidation of Fe(II) by dissolved oxygen [16].

Nitrate is a common co-contaminant in industrial environments which has the potential to effect chromate remediation both as an oxidizing species and competing oxyanion. The presence of co-contaminants such as nitrate has been shown to impair the amount of Cr(VI) reduced by zero-valent iron by approximately three orders of magnitude [21]. Palladium catalysed reduction of nitrate has been shown to be minimal [22, 23], and the application of palladium-functionalized magnetite could provide a route to nitrate-resistant chromate treatment. The

ability of palladium to promote oxidation of formate also allows potential recharging of magnetite reactivity through the supply of additional electrons [24, 25].

Here we develop the application of biogenic magnetite for Cr(VI) remediation by moving from batch experiments [16, 26] towards "real world" systems involving continuous flow and co-contaminants. We report continuous removal of chromate in column systems, comparing the relative removal and retention abilities of magnetite and palladized-magnetite under oxic, anoxic and nitrate-amended conditions. High resolution microscopy and spectroscopic analyses of reacted magnetite allows understanding of the relevant reaction mechanisms to be developed and comparisons made with previous data on chromate reduction by magnetite [16].

7.2 Experimental Methodology

7.2.1 Magnetite Production

Biogenic magnetite was produced by reduction of a ferrihydrite suspension (Fe(III)-oxyhydroxide) using late log phase cultures of *Geobacter sulfurreducens* under a 80:20 N_2-CO_2 atmosphere, as described previously [16]. Stock 50 mmol/l Fe ferrihydrite suspensions were prepared with 20 mM sodium acetate as an electron donor, 30 mM sodium hydrogen carbonate and an electron shuttle to accelerate the reductive transformation [10 μM; 9,10-anthraquinone-2,6-disulfonate (AQDS)] [27]. Three times washed suspensions of cells of *Geobacter sulfurreducens* (100 ml) were prepared at a cell concentration of 0.6 mg/ml protein. Bottles were incubated overnight at 30 ºC, and the resulting magnetite washed three times in anaerobic deionized water before storage anoxically as a slurry in the dark at ambient temperature until required.

The magnetite surface was functionalized with Pd(0) by exposure of washed suspensions to a 2.5 mM $NaPdCl_4$ (Sigma Aldrich, CAS no. 13820-53-6) solution overnight to achieve a 5% loading, as described previously [12]. Manipulations involving Pd compounds were performed under an argon atmosphere.

7.2.2 Column Reduction Experiments

Continuous Cr(VI) removal experiments were performed in glass columns of 30 mm diameter, 300 mm length. Columns were filled with acid-purified sand (Sigma Aldrich, UK; CAS no. 60676-86-0) on top of a cotton wool bung to a height of 3 cm. A 2.5 ml aliquot of 0.5 mol/l magnetite slurry was transferred to the column to create a biogenic magnetite impregnated sand layer. The remainder of the column was filled with sand leaving a 1 cm deep headspace to collect effluent from. A sand only control column was also evaluated for chromate removal.

Solutions were supplied to the column using a peristaltic pump (Watson Marlow 205S) at a flow rate of 0.13 cm^3/min, creating an effective residence time of 6 h. In all columns the flow direction was from bottom to top. Chromate was added as an inlet aqueous solution of 50 μM K_2CrO_4 with pH 7.4. Three solution redox conditions were investigated: anaerobic, nitrate-amended and aerobic. Anaerobic conditions were achieved by sparging inlet reservoirs with N_2, nitrate-amended conditions by the addition of 10 mM $NaNO_3$ to an anaerobic reservoir and aerobic conditions were maintained by sparging with air. Additions of sodium formate at a concentration of 20 mM were made to three additional reservoirs under the redox conditions described above. Column experiments were ended when the effluent Cr(VI) concentration equalled the influent value (50 μM) and did not change over a period of one day, or after 340 h.

7.2.3 Liquid Phase Analyses

The concentration of chromate in column effluents was determined using a spectrophotometric assay after reaction with 1,5-diphenylcarbazide (DPC) [28]. Triplicate aliquots of 100 μl were added to 1.4 ml of DPC solution and allowed to react for 10 min; absorbance at 540 nm was then measured using a Camspec M501 single beam scanning UV/visible spectrophotometer (%RSD = 5.0 at 10 μM [Cr(VI)]). Columns were run in duplicate and representative data are presented and results were reproducible. Calibration curves of absorbance to concentration were obtained daily by assay of stock solutions of known chromate concentrations. These data, which only measure Cr(VI), were correlated with Cr ICP-AES analysis of column effluent (Cr_{TOT}).

Redox potentials of chromate reservoirs were measured using an InLab redox micro (Mettler Toledo) electrode that has a combination of a platinum ring indicator electrode and a silver/silver chloride reference electrode. The electrolyte is 3M KCl. A standard solution with a redox potential of 200 mV was used to ensure accurate measurements.

Effluent nitrate and formate concentrations were determined by ion chromatography (IC). Formate analyses were performed on a Dionex DX120 system with a Dionex AS40 autosampler using a conductivity detector with an injection loop of 100 μl. The mobile phase was 1 mM octane sulfonic acid (OSA) with a flow rate of 0.15 ml/min. The system backpressure was typically 1,400 psi. A calibration standard of 1.0g/l formic acid was used with an accuracy of ~3% and minimum detection limit of 0.1 mg/l. Nitrate analyses were performed on a Metrohm 761 Compact IC with a Metrohm 813 autosampler using a conductivity detector, with an injection loop of 100 μl. The mobile phase was 9 mM Na_2CO_3 with a flow rate of 1.4 ml/min and chemical suppression was 100 mM H_2SO_4. The system backpressure was typically 17 MPa. A calibration standard of 1.0 g/l sodium nitrate was used with an accuracy of ~3% and minimum detection limit of 0.1 mg/l.

7.2.4 Solid Phase Analyses

Total iron concentration in the ferrihydrite slurry was determined by digestion in 0.5 M HCl and 0.25 M hydroxylamine hydrochloride followed by ferrozine assay of the resulting solution [29, 30]. The total concentration of Fe in the prepared biogenic magnetite was verified (0.45±2 mol/l Fe) by inductively coupled plasma atomic emission spectroscopy (ICP-AES) on a Perkin-Elmer Optima 5300 dual view ICP-AES following microwave assisted digestion in concentrated nitric acid.

Following column reduction experiments, the magnetite layer was collected and stored for further analysis. X-ray photoelectron spectroscopy (XPS) data were recorded using a VG Escalab 250 instrument employing a monochromatic Al *K*α X-ray source and an analyser pass energy of 20 eV, resulting in a total energy resolution of ~0.9 eV. Uniform charge neutralization

of the photoemitting surface was achieved by exposing the surface to low energy electrons using a flood gun. The system base pressure was 5 x 10^{-10} mbar. All samples were dried in an argon glove box and loaded into the spectrometer while it was flushed with nitrogen to minimize air exposure. Photoelectron binding energies (BE) were referenced to C 1*s* adventitious contamination peaks at 285 eV BE. Fitting of XPS data was carried out by fitting an appropriate (Shirley) background [31]. Components (70% Lorentzian:30% Gaussian) were then assigned to the Fe 2*p* region based on multiplet splitting calculations for free Fe ions [32, 33]. The Fe $2p^{3/2}$ peak was fitted using three multiplet peaks to account for the Fe(II) contribution, and four multiplet peaks to account for the Fe(III) contribution. Two further components, a high-BE surface peak and a low-BE pre-peak, were required to improve the fit (see Appendix 2 for details).

X-ray adsorption (XA) spectra were obtained on beamline 4.0.2 at the Advanced Light Source (Berkeley, CA, U.S.A.), using the octopole magnet end station [34]. Samples of magnetite were analysed at both the Cr and Fe $L_{2,3}$-edges. XA was monitored in total-electron-yield (TEY) mode, which gives an effective probing depth of ~4.5 nm. At successive photon energies the XA was measured with circularly polarized X-rays for the two opposite magnetization directions by reversing the 0.6 T applied field with respect to the helicity vector of the X-rays. The spectra for the two magnetization directions were normalized to the incident beam intensity and subtracted to give the X-ray magnetic circular dichroism (XMCD) spectrum [35]. The measured Fe $L_{2,3}$-edge XMCD was used to obtain the site occupancies of the Fe cations in the spinel structure of the biogenic magnetite precipitates [36-38].

Transmission electron microscopy (TEM) was conducted using a FEI Tecnai TF20 microscope equipped with a field emission gun (FEG), high angle annular dark field (HAADF) detector, energy dispersive X-ray analysis (EDX) system (Oxford Instruments INCA 350/80mm X-Max SDD detector) and a Gatan Orius SC600A CCD camera. TEM images reported are both bright-field and dark-field obtained using an operating beam voltage of 200 keV. A droplet of each

sample was placed on a carbon grid (Agar Scientific, Stansted, UK) and allowed to dry before imaging.

7.3 Results and Discussion

7.3.1 Chromate Reduction in Columns

Continuous removal of 50 μM potassium chromate was performed in column systems with a biogenic magnetite barrier under anoxic, nitrate-amended and oxic conditions alongside a no magnetite control column. Redox potentials of influent 50 μM Cr(VI) solutions relative to the standard hydrogen electrode (SHE) were measured as +108 mV for anaerobic, +149 mV nitrate amended and +236 mV for the aerobic condition. Effluent Cr(VI) concentrations measured using a colorimetric assay were used to construct breakthrough curves (Appendix 2 - Figure A2.1a), which were integrated to produce curves of cumulative Cr(VI) removal (Figure 7.1a). The control column containing no magnetite removed a negligible quantity of Cr(VI) (average ~5.7%, Figure 7.1a), and the addition of a biogenic magnetite barrier layer resulted in a substantial (2.8 – 6.0 times) increase in removal of Cr(VI) (Figure 7.1a). However, for all solution redox conditions much less than 100% removal was evident, and the capacity of the biogenic magnetite was exhausted after ~40 h, reaching a total Cr(VI) removal between 5.9 and 12 μmol (16-35% of the total Cr(VI) influent over this time period). The influence of redox conditions was minor, although the pattern of total Cr(VI) removed in this system followed the redox trend, with the largest quantity of Cr(VI) retained in a column with lowest redox potential, while the air-sparged "aerobic" condition retained the least Cr(VI). Columns containing Pd-functionalized magnetite as the reactive barrier gave a similar removal capacity to the unmodified magnetite barriers (Appendix 2 - Figure A2.3), reaching Cr(VI) saturation in a comparable period of time. Although Pd-functionalization increases the near surface Fe(II) content of biomagnetite (Table 7.1) [12], this has no effect on reactivity. Again, there was little difference between the retention ability of columns under the three different redox conditions.

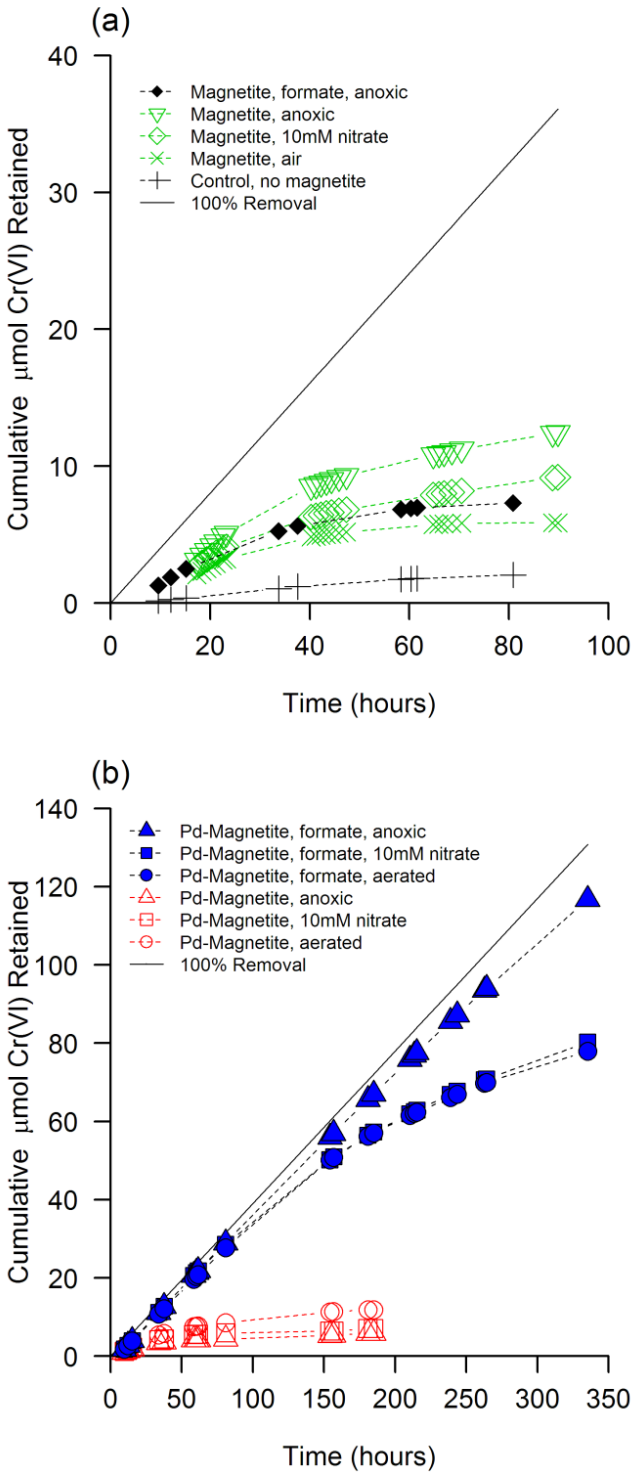

Figure 7.1 – Cumulative Cr(VI) removed from solution in (a) magnetite loaded columns and (b) Pd-functionalized magnetite columns. Curves are formed by integration of column outlet Cr(VI) concentrations (see Appendix 2 - Figure A2.1), measured by colorimetric assay. Supplementary plots of this data are available (Appendix 2 - Figure A2.2 and Figure A2.3).

The addition of 20 mM formate to the influent for columns with Pd-functionalized magnetite resulted in a substantial increase in the amount of chromate removed from solution, with between 83 – 93% removal sustained for ~150 h under all redox conditions (Figure 7.1b). Saturation of the reductive capacity after 300 hours was apparent for the nitrate and air treated systems, whereas the anoxic column still maintained 80% Cr(VI) removal (Appendix 2 - Figure A2.1b). A control column containing unmodified magnetite charged with a formate-supplemented influent under anoxic conditions (Figure 7.1a) had similar characteristics to both the magnetite and Pd-magnetite columns performed without formate. This result indicates that it is the combination of Pd-magnetite and formate that allows for an enhanced level of sustained Cr(VI) removal, with total Cr(VI) removed from solution increased by over an order of magnitude when compared to systems in which either formate or Pd is absent. Analysis of effluent formate concentrations suggest 20 mM was added to excess, as an initial drop of ~20% during the first 24 hours then stabilized to negligible consumption for the remainder of the experiment (Appendix 2 - Figure A2.4); suggestive of initial saturation of Pd-magnetite surface with H• from heterolytic fission of formate [24].

The cumulative removal of Cr(VI) (Figure 7.1) demonstrates that solution redox conditions have limited effect on the capacity of all magnetite systems to remove Cr(VI). Although the presence of oxidizing species such as nitrate or dissolved oxygen was sufficient to diminish the total Cr removed from solution, in the best performing of these systems (combining Pd-magnetite with formate), around 70% of the equivalent anaerobic retention capacity was maintained (Figure 7.1b). Effluent analysis of nitrate concentrations showed no significant removal by any magnetite system (Appendix 2 - Figure A2.5), demonstrating the selectivity of this approach for chromate reduction and remediation.

7.3.2 Characterization of post reaction magnetite

The reactive magnetite layer from columns treated with anoxic and nitrate solutions was retained for analysis to investigate the mechanism of enhanced Cr(VI) retention by Pd-magnetite systems with formate, and to assess for solid phase interaction with nitrate co-

Table 7.1 – Summary of post reaction analyses on magnetite layer from anaerobically treated columns supplemented with formate and nitrate.

	DPC Assay	XAS	Individual peaks XPS		XPS	XPS	XMCD	XPS	XMCD
	Cumulative Cr(VI), µmol[#]	%Cr cf Fe[†]	%Cr cf Fe[†]	%Pd cf Fe[†]	Pd metal : Pd oxide[†]	Cr(III) : Cr(VI) [†]	Fe^{2+} / Fe total‡	Fe^{2+} / Fe total[†]	$T_d : O_h$‡
Pd-Magnetite, formate, anoxic	116.7	39.3	49.7	12.0	47:53	100:0	0.31	0.35	0.48
Pd-Magnetite, formate, nitrate	80.3	37.4	39.0	6.2	44:56	100:0	0.32	0.34	0.49
Pd-Magnetite, anoxic	5.9	3.7	28.3	11.2	82:18	100:0	0.38	0.40	0.42
Pd-Magnetite, nitrate	7.1	4.9	7.1	8.6	92:8	57:43	0.37	0.44	0.42
Magnetite, formate, anoxic	8.9	14.6	16.9	N/A	N/A	49:51	0.51	0.35	0.45
Magnetite*							0.38		0.44
Pd-magnetite*							0.41		0.41

*from Coker et al. (2010) [12] [#]error ~±5% [†]error ~±10% ‡error ±0.02

contamination which may not be evident in column effluent data. Initial XPS and XAS (Table 7.1) analyses of the magnetite layers exposed to Cr(VI) in the columns reveal accumulation of Cr in all samples. This is indicative of Cr retention by the reactive barrier rather than sorption to sand in the column or release back into solution as Cr(III). Confirmation that Cr(III) was not released to solution was obtained by ICP-AES analyses of the effluent, which gave good agreement with the concentration of Cr measured by colorimetric assay for Cr(VI) (data not shown). These results are in agreement with previous data of Cr(VI) interactions with magnetite [16], consistent with retention of Cr(III) by the mineral.

The quantity of Cr associated with the surface of the magnetite samples was assessed using both XPS and XAS. Both these techniques give surface rather than bulk values for materials, however as these measurements are on nanoparticles (~20 nm - Figure 7.2) with a high surface to bulk ratio, there is a high proportion of the nanoparticle examined, >83% and 100% respectively, if an analytical probing depth of 4.5 nm (XAS/XMCD) and 5-10 nm (XPS) is assumed [39]. From XPS relative peak height analysis there is 39-50% Cr relative to Fe associated with Pd-magnetite supplemented with formate (Table 7.1), which compares well with relative peak heights from XAS that give values between 37-39% Cr compared to Fe for the same samples (Figure 7.3a, Table 7.1). Analysis of material from columns not supplemented with formate gave a much lower average value of 11% Cr relative to Fe associated with the samples (Table 7.1), and all these data relate well to the trend of cumulative Cr removal from the effluent.

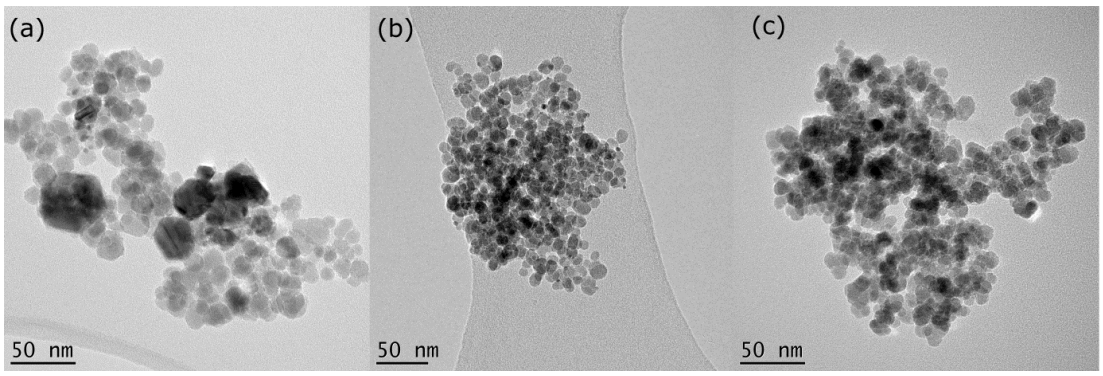

Figure 7.2 – Transmission electron micrographs of magnetites from anoxic conditioned columns with (a) Pd treated magnetite exposed to formate, (b) Pd treated magnetite and (c) untreated magnetite exposed to formate.

In magnetite samples both with and without Pd-functionalization the shape of Cr $L_{2,3}$-edge XAS spectra are typical of Cr(III) when compared to calculated spectra for Cr(III) and Cr(VI) [37] (Appendix 2 - Figure A2.6, Figure 7.3a). For samples containing low concentrations of Cr the presence of some Cr(VI) by XAS cannot be ruled out as the signal-noise ratio is low. Fitting of Cr 2*p* XPS data (Appendix 2 - Figure A2.7) indicate Cr(III) exclusively in Pd-functionalized formate treated samples, in agreement with qualitative XAS analysis, however there is an

indication of up to 50% Cr(VI) in samples which retained only a small quantity of Cr. (Table 7.1, Figure A2.7). These data demonstrate that magnetite systems remove chromate from solution by a two-step process; first sorption of the oxyanionic Cr(VI) to the surface followed by reduction to Cr(III), but under more oxic conditions (without the addition of formate and Pd) there is incomplete reduction of Cr(VI). This has implications for Cr retention, as sorption of oxyanionic Cr(VI) may be more easily reversed.

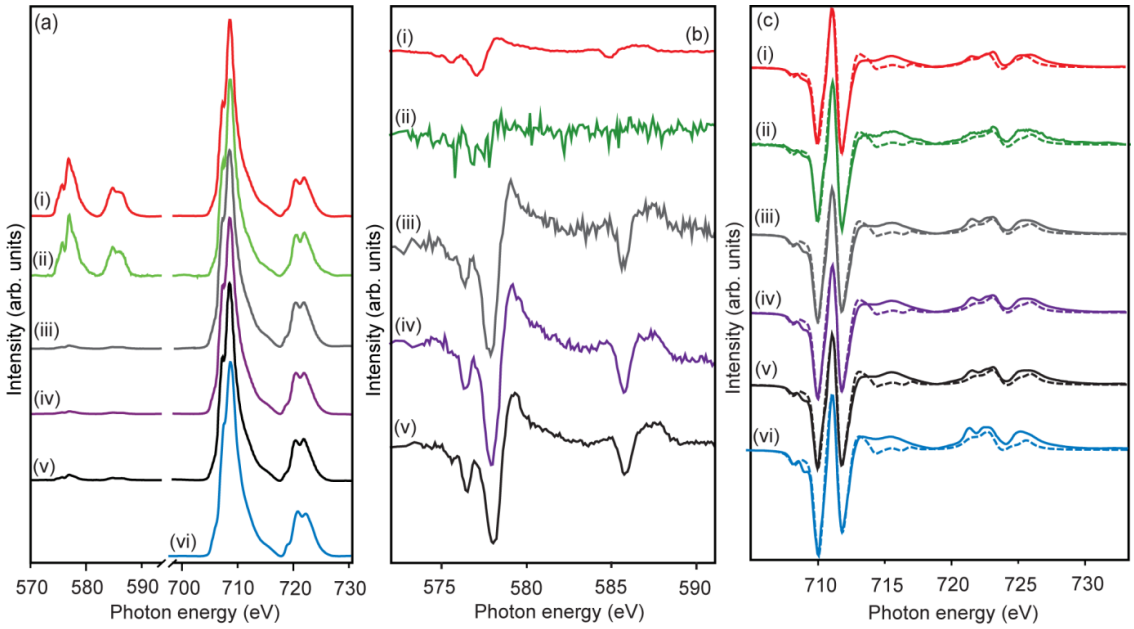

Figure 7.3 – (a) Cr and Fe $L_{2,3}$-edge background subtracted XA spectra obtained by normalizing the Fe L_3 maximum to unity and scaling the Cr $L_{2,3}$-edge accordingly, (b) Cr $L_{2,3}$–edge XMCD spectra obtained after first normalizing the background subtracted XA spectra to unity at the L_3 maximum and (c) Fe $L_{2,3}$-edge XMCD spectra (solid line) and fit (dotted line) for (i) Pd-magnetite with formate anoxic; (ii) Pd-magnetite with formate anoxic and nitrate; (iii) Pd magnetite without formate anoxic and (iv) anoxic with nitrate; (v) magnetite with formate under anoxic conditions, (vi) unreacted magnetite (Fe $L_{2,3}$ XAS and XMCD only), from Coker et al. [12].

XMCD spectra at the Cr $L_{2,3}$-edge were observed for all samples, indicating partial incorporation of Cr(III) into the spinel structure of magnetite, as sorbed Cr(III) or Cr(VI) would not give a "magnetic" Cr signal [26]. The XMCD for the Cr $L_{2,3}$-edge in Figure 7.3(b) are

derived from XAS spectra that have each been normalized to 1 in order to reveal that the Cr $L_{2,3}$-edge XMCD response is strongest in systems with the lightest Cr loading. Attenuation of magnetic signals in systems with greater Cr concentrations would occur as substitution of Cr(III) into magnetite spinels reaches saturation, resulting in precipitation of a surface layer which is not magnetic and would shroud the XMCD signal from this surface sensitive technique. In addition, the shape of the Cr $L_{2,3}$-edge XMCD spectra are typical of Cr(III) when compared with calculated XMCD spectra for Cr(III) (Appendix 2 - Figure A2.6) [38]. Any Cr(VI) identified by XPS is therefore most likely present as a surface sorbed layer.

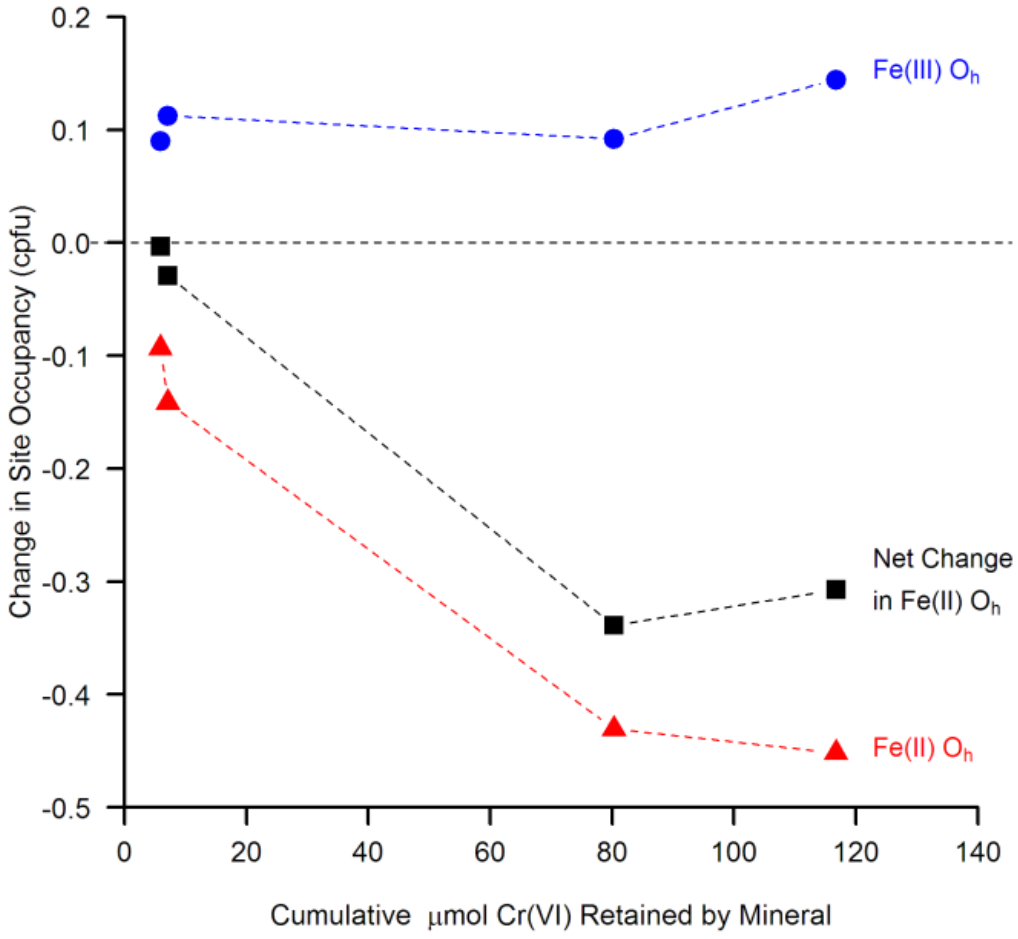

Figure 7.4 – Change in Fe(II) and Fe(III) occupancy in Pd-functionalized magnetite octahedral spinel sites as a function of total Cr(VI) removed in columns. Occupancy values are relative to untreated magnetite, determined by component fitting of Fe $L_{2,3}$-edge XMCD data (Figure 7.3c). Tetrahedral site occupancy is fixed at 1.00 Fe(III).

Further investigation of Cr(III) substitution into the structure of the biogenic magnetite was achieved by analysing the Fe $L_{2,3}$-edge XMCD data using the weighted sum of theoretically calculated spectra to give the relative amounts of the three Fe components within magnetite: Fe(II) octahedral (O_h), Fe(III) tetrahedral (T_d) and Fe(III) O_h (see Pattrick *et al.* [27] for details). Fitting of the Fe $L_{2,3}$-edge XMCD (Figure 7.3c) revealed some variation in the quantity of Fe(II) at the end of the experiment between samples (Table 7.1). These differences are due to the interplay of two factors which reduce the amount of Fe(II) in the magnetite structure; substitution of Cr(III) for Fe(II) and oxidation of Fe(II) O_h to Fe(III) O_h connected to the reduction of Cr(VI).

Detailed examination of the spectra show that T_d/O_h ratios are relatively constant among samples (0.42 – 0.49, Table 7.1) and therefore it is possible to examine O_h site occupancies of Fe(II) and Fe(III) in detail (Figure 7.4). As the amount of total cumulative Cr(VI) removed from solution between samples increases, the amount of Fe(II) decreases, reaching a minimum of ~0.45 cations per formula unit (cpfu) despite further increases in Cr(VI) removal, and the amount of Fe(III) O_h increases but by a lesser degree to a maximum of ~0.15 cpfu (Table 7.1; Figure 7.4). The shape of the Fe(II) O_h cpfu curve (Figure 7.4) indicates saturation of the magnetite structure at high Cr loadings, approaching 100 μmol total Cr(VI) loading. The difference between the amount of Fe^{2+} lost and the amount gained as Fe^{3+} on O_h sites due to oxidation is equivalent to the amount of Cr^{3+} substituting for Fe in octahedral sites (0.3 cpfu) as shown previously [26]. Both oxidation and substitution processes are active in all systems including nitrate and anoxic treatments, and in the presence of Pd and formate.

TEM images of reacted magnetite subjected to anoxic treatments (Figure 7.2) show that for functionalized magnetite the Pd particle size was altered in the presence of formate. Non-functionalized magnetite (Figure 7.2c) consists of particles 15-20 nm in size, consistent with nanoparticulate biogenic magnetite [12]. The sample of Pd-magnetite not exposed to formate (Figure 7.2b) shows smaller particles ~5 nm encrusting larger particles (15-20 nm), most likely Pd(0)-nanoparticles held on larger magnetite nanoparticles as shown previously [12]. The

sample of Pd-magnetite exposed to formate (Figure 7.2a) shows a similar array of particles as the non-formate system, with the addition of some larger (25-50 nm) electron dense particles. Elemental maps of the region displayed in Figure 7.2a for Fe, Cr and Pd generated by STEM-EDX (Figure 7.5) indicate that the large particles in Figure 7.2a correlate well with the distribution of Pd in the sample, while Fe and Cr are distributed together throughout the sample and correlate with the arrays of smaller particles in Figure 7.2a. The redistribution of Pd into larger particles occurs only with the addition of formate to the column, and no aggregation was observed in systems without Pd (Figure 7.2b) or without formate (Figure 7.2c).

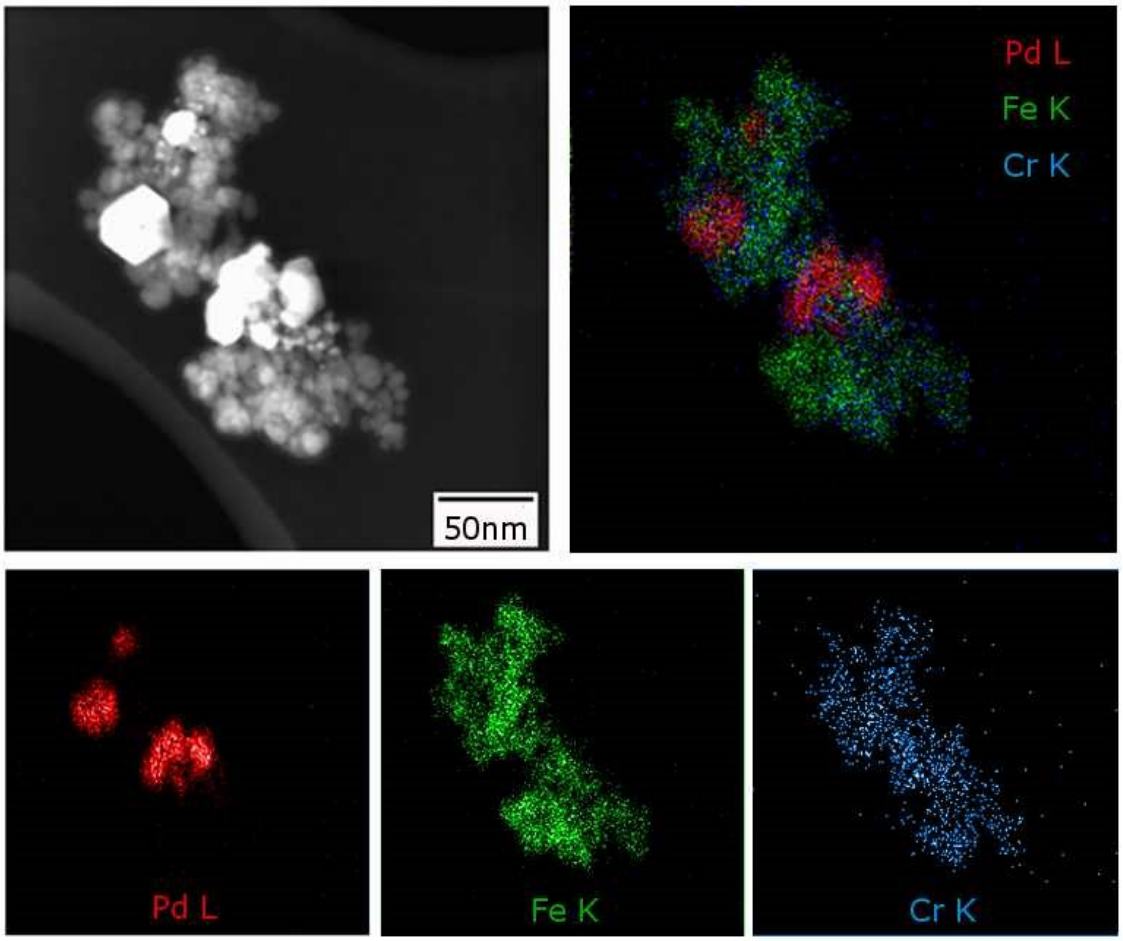

Figure 7.5 – Backscattered electron image (top left) and elemental spot maps measured by STEM-EDX of Cr, Fe and Pd for Pd treated magnetite supplemented with formate under anoxic conditions (Figure 7.2a).

Fitting of the Pd 3*d* XPS spectra (Appendix 2 - Figure A2.7) indicate that two Pd species are present in all the samples to varying extent, one at 335.1-335.9 eV BE, typical of metallic Pd, and a second at a higher BE of between 336.3-337.9 eV, most likely Pd(II)-oxide [40]. Results suggest oxidation of Pd is greater in formate treated systems, up to 53% of the total Pd (Table 7.1, Appendix 2 - Figure A2.7b). However, in the formate treated system with Pd-magnetite, the recrystallization of Pd into larger particles of 25-50nm reduces the percentage bulk probed by XPS to >78% of the particle, and the Pd(0):Pd(II) ratio in these samples is more representative of the surface composition than the true bulk value.

The redistribution and substantial surface oxidation of Pd(0) only in formate amended systems is an indication that formate-Pd interactions are involved in enhancing removal of Cr(VI). The correlated distribution of Fe and Cr (Figure 7.5) could suggest that Pd-formate interactions serve to regenerate the reductive capacity of the magnetite. This would be indicative of the magnetite serving as an active component in the formate enhanced reduction of Cr(VI) and not simply as a support for a Pd catalyst. Further work on the precise mechanism of Cr(VI) reduction in these highly effective hybrid systems is clearly warranted.

7.4 Conclusions

Comparison of the suite of data obtained for the different redox treatments reveals similar characteristics for each of the magnetite samples (Table 1). Cr concentrations from XPS and XAS analyses vary in accordance with variation in amount of Cr(VI) removed from solution as determined by colorimetric assays, whereas the ratio of Cr(III):Cr(VI), Pd(0):Pd(II)oxide and Fe(II):Fe(III) do not alter with the addition of nitrate when compared to the equivalent anoxic sample. As with the total Cr(VI) removed from solution, influence of nitrate on the characteristics of the final material appears slight, suggesting no mechanistic interference in the presence of nitrate.

Our results demonstrate that the addition of Pd(0) to magnetite in the presence of formate enhances the removal of chromate from solution by more than an order of magnitude. The co-

occurrence of Cr and Fe on the surface of the reacted magnetite suggests that the Pd activated oxidation of formate causes enhancement of the reductive capacity of the Pd-magnetite material. These experiments indicate that although remediation performance is optimized in anoxic conditions, the presence of nitrate or dissolved oxygen results in only a modest loss of reductive capacity. The selective remediation of chromate in the presence of other oxidizing species is an important goal as co-contaminants such as nitrate are commonly present in the environment. The demonstration of a formate-Pd coupled magnetite system to achieve chromate removal under nitrate-supplemented and oxic conditions comparable to that under anoxic conditions offers the prospect of a robust and effective remediation approach which is selective for chromate against competing oxidants and oxyanions. The testing and performance assessment of this system under a wider range of environmentally relevant conditions is now necessary to bring this technology forward from the lab to the field application.

7.5 Acknowledgements

James Byrne, Richard Pattrick and Elke Arenholz are acknowledged for collection of XAS and XMCD data. Dr A Walton and Dr M Ward are thanked for their assistance with TEM and XPS analyses through the Leeds EPSRC Nanoscience and Nanotechnology Research Equipment Facility. Mr P Lythgoe and Mr A Bewsher are thanked for their assistance with data collection using IC and ICP-AES.

This chapter is reprinted (adapted) with permission from *Environmental Science and Technology* **2012** 46 (6), 3352-3359, and can be found online at http://pubs.acs.org/doi/abs/10.1021/es2037146

7.6 References

[1] Richard, F. C.; Bourg, A. C. M., Aqueous geochemistry of chromium - a review. *Water Res.* **1991,** *25*, 807-816.

[2] Anderson, R. A.; Bryden, N. A.; Polansky, M. M., Lack of toxicity of chromium chloride and chromium picolinate in rats. *J. Am. Coll. Nutr.* **1997,** *16*, 273-279.

[3] Lytle, C. M.; Lytle, F. W.; Yang, N.; Qian, J.-H.; Hansen, D.; Zayed, A.; Terry, N., Reduction of Cr(VI) to Cr(III) by wetland plants: potential for in situ heavy metal detoxification. *Environ. Sci. Technol.* **1998,** *32*, 3087-3093.

[4] Costa, M.; Klein, C. B., Toxicity and carcinogenicity of chromium compounds in humans. *Crit. Rev. Toxicol.* **2006,** *36*, 155-163.

[5] Fendorf, S.; Wielinga, B. W.; Hansel, C. M., Chromium transformations in natural environments: The role of biological and abiological. processes in chromium(VI] reduction. *Int. Geol. Rev.* **2000,** *42*, 691-701.

[6] He, Y. T.; Traina, S. J., Cr(VI) reduction and immobilization by magnetite under alkaline pH conditions: The role of passivation. *Environ. Sci. Technol.* **2005,** *39*, 4499-4504.

[7] Jung, Y.; Choi, J.; Lee, W., Spectroscopic investigation of magnetite surface for the reduction of hexavalent chromium. *Chemosphere* **2007,** *68*, 1968-1975.

[8] Peterson, M. L.; Brown, G. E.; Parks, G. A., Direct XAFS evidence for heterogeneous redox reaction at the aqueous chromium/magnetite interface. *Colloids Surf., A* **1996,** *107*, 77-88.

[9] Lee, W.; Batchelor, B., Reductive capacity of natural reductants. *Environ. Sci. Technol.* **2002,** *37*, 535-541.

[10] Kendelewicz, T.; Liu, P.; Doyle, C. S.; Brown, G. E., Spectroscopic study of the reaction of aqueous Cr(VI) with Fe3O4(111) surfaces. *Surf. Sci.* **2000,** *469*, 144-163.

[11] Lovley, D. R.; Stolz, J. F.; Nord, G. L.; Phillips, E. J. P., Anaerobic production of magnetite by a dissimilatory iron-reducing microorganism. *Nature* **1987,** *330*, 252-254.

[12] Coker, V. S.; Bennett, J. A.; Telling, N. D.; Henkel, T.; Charnock, J. M.; van der Laan, G.; Pattrick, R. A. D.; Pearce, C. I.; Cutting, R. S.; Shannon, I. J.; Wood, J.; Arenholz, E.; Lyon, I. C.; Lloyd, J. R., Microbial engineering of nanoheterostructures: biological synthesis of a magnetically recoverable palladium nanocatalyst. *ACS Nano* **2010,** *4*, 2577-2584.

[13] Cutting, R. S.; Coker, V. S.; Fellowes, J. W.; Lloyd, J. R.; Vaughan, D. J., Mineralogical and morphological constraints on the reduction of Fe(III) minerals by Geobacter sulfurreducens. *Geochim. Cosmochim. Acta* **2009,** *73*, 4004-4022.

[14] Gorski, C. A.; Nurmi, J. T.; Tratnyek, P. G.; Hofstetter, T. B.; Scherer, M. M., Redox behavior of magnetite: implications for contaminant reduction. *Environ. Sci. Technol.* **2010,** *44*, 55-60.

[15] Gorski, C. A.; Scherer, M. M., Influence of magnetite stoichiometry on Fe-II uptake and nitrobenzene reduction. *Environ. Sci. Technol.* **2009,** *43*, 3675-3680.

[16] Cutting, R. S.; Coker, V. S.; Telling, N. D.; Kimber, R. L.; Pearce, C. I.; Ellis, B. L.; Lawson, R. S.; der Laan, G. V.; Pattrick, R. A. D.; Vaughan, D. J.; Arenholz, E.; Lloyd, J. R., Optimizing Cr(VI) and Tc(VII) remediation through nanoscale biomineral engineering. *Environ. Sci. Technol.* **2010,** *44*, 2577-2584.

[17] Ngomsik, A.-F.; Bee, A.; Draye, M.; Cote, G.; Cabuil, V., Magnetic nano- and microparticles for metal removal and environmental applications: a review. *C. R. Chim.* **2005,** *8*, 963-970.

[18] Gallios, G. P.; Vaclavikova, M., Removal of chromium (VI) from water streams: a thermodynamic study. *Environ. Chem. Lett.* **2008,** *6*, 235-240.

[19] Hayes, K. F.; Papelis, C.; Leckie, J. O., Modeling ionic-strength effects on anion adsorption at hydrous oxide solution interfaces. *J. Colloid Interface Sci.* **1988,** *125*, 717-726.

[20] He, Y. T.; Traina, S. J., Transformation of magnetite to goethite under alkaline pH conditions. *Clay Miner.* **2007,** *42*, 13-19.

[21] Rivero-Huguet, M.; Marshall, W. D., Impact of various inorganic oxyanions on the removal rates of hexavalent chromium mediated by zero-valent iron. *Environ. Chem.* **2010,** *7*, 250-258.

[22] Soares, O.; Órfão, J.; Pereira, M., Activated carbon supported metal catalysts for nitrate and nitrite reduction in water. *Catal. Lett.* **2008,** *126*, 253-260.

[23] Prüsse, U.; Hähnlein, M.; Daum, J.; Vorlop, K.-D., Improving the catalytic nitrate reduction. *Catal. Today* **2000,** *55*, 79-90.

[24] Mabbett, A. N.; Yong, P.; Farr, J. P. G.; Macaskie, L. E., Reduction of Cr(VI) by "palladized" biomass of Desulfovibrio desulfuricans ATCC 29577. *Biotechnol. Bioeng.* **2004,** *87*, 104-109.

[25] Garron, A.; Epron, F., Use of formic acid as reducing agent for application in catalytic reduction of nitrate in water. *Water Res.* **2005,** *39*, 3073-3081.

[26] Telling, N. D.; Coker, V. S.; Cutting, R. S.; van der Laan, G.; Pearce, C. I.; Pattrick, R. A. D.; Arenholz, E.; Lloyd, J. R., Remediation of Cr(VI) by biogenic magnetic nanoparticles: an x-ray magnetic circular dichroism study. *Appl. Phys. Lett.* **2009,** *95*, 163701.

[27] Coker, V. S.; Bell, A. M. T.; Pearce, C. I.; Pattrick, R. A. D.; van der Laan, G.; Lloyd, J. R., Time-resolved synchrotron powder X-ray diffraction study of magnetite formation by the Fe(III)-reducing bacterium Geobacter sulfurreducens. *Am. Mineral.* **2008,** *93*, 540-547.

[28] Skougstad, M. W.; Fishman, M. J.; Friedman, L. C.; Erdman, D. E.; Duncan, S. S., Method for determination of inorganic substances in water and fluvial sediments. US Geological Survey: Washington DC, **1979**; Vol 5.

[29] Stookey, L. L., Ferrozine - a new spectrophotometric reagent for iron. *Anal. Chem.* **1970,** *42*, 779.

[30] Lovley, D. R.; Phillips, E. J. P., Availability of ferric iron for microbial reduction in bottom sediments of the fresh-water tidal potomac river. *Appl. Environ. Microbiol.* **1986,** *52*, 751-757.

[31] Shirley, D. A., High-resolution X-ray photoemission spectrum of valence bands of gold. *Phys. Rev. B: Condens. Matter Mater. Phys.* **1972,** *5*, 4709-4714.

[32] Gupta R. P.; Sen S. K. (1975) Calculation of multiplet structure of core p-vacancy levels II. Phys. Rev. B 12(1), 15–19.

[33] McIntyre, N. S.; Zetaruk, D. C. X-ray photoelectron spectroscopic studies of iron oxides. *Anal. Chem.* **1977**, 49, 1521-1529.

[34] Arenholz, E.; Prestemon, S. O., Design and performance of an eight-pole resistive magnet for soft x-ray magnetic dichroism measurements. *Rev. Sci. Instrum.* **2005,** *76*.

[35] Pattrick, R. A. D.; Van der Laan, G.; Henderson, C. M. B.; Kuiper, P.; Dudzik, E.; Vaughan, D. J., Cation site occupancy in spinel ferrites studied by X-ray magnetic circular dichroism: developing a method for mineralogists. *Eur. J. Mineral.* **2002,** *14*, 1095-1102.

[36] Coker, V. S.; Pearce, C. I.; Pattrick, R. A. D.; Van der Laan, G.; Telling, N. D.; Charnock, J. M.; Arenholz, E.; Lloyd, J. R., Probing the site occupancies of Co-, Ni-, and Mn-substituted biogenic magnetite using XAS and XMCD. *Am. Mineral.* **2008,** *93*, 1119-1132.

[37] van der Laan, G.; Thole, B. T., Strong magnetic X-ray dichroism in 2p absorption spectra of 3d transition metal ions. *Appl. Phys. Lett.***1991,** *43*, 13401-13411.

[38] van der Laan, G.; Kirkman, I. W., The 2p absorption spectra of 3d transition metal compounds in tetrahedral and octahedral symmetry. *J. Phys.: Condens. Matter* **1992,** *4*, 4189-4204.

[39] Coker, V. S.; Pearce, C. I.; Lang, C.; van der Laan, G.; Pattrick, R. A. D.; Telling, N. D.; Schuler, D.; Arenholz, E.; Lloyd, J. R., Cation site occupancy of biogenic magnetite compared to polygenic ferrite spinels determined by X-ray magnetic circular dichroism. *Eur. J. Mineral.* **2007,** *19*, 707-716.

[40] Kim, K. S.; Gossmann, A. F.; Winograd, N., X-ray photoelectron spectroscopic studies of palladium oxides and palladium-oxygen electrode. *Anal. Chem.* **1974,** *46*, 197-200.

Chapter 8

Conclusions and Recommendations

8.1 Conclusions

8.1.1 Environmental Behaviour of DU Munitions

The morphology, elemental composition, crystalline phase assemblage and uranium speciation were characterised in a suite of environmentally aged DU particles from the Eskmeals firing range. This was performed using a novel application of synchrotron X-ray chemical imaging and microfocus X-ray spectroscopy. In this study the first evidence of major environmentally mediated alteration of DU residues was observed, which has implications for understanding the long term stability of these materials in the surface environment. A key aspect of this work was a comparison of particle characteristics between two sampling areas from the Eskmeals firing range, a surface soil and a waste storage pit, in which U speciation was found to be different. This demonstrates that local geochemical conditions have a substantial influence on the fate of DU particles, and highlights the need to consider site specific variation in soil characteristics when assessing the long term fate of these materials.

As shown in Chapter 2, previous studies of environmentally aged DU contamination have noted the persistence of reduced U oxide particles at firing ranges [1] and in soils contaminated with incinerator residues [2]. The characterisation of aged particles in a surface soil presented in this investigation appears to support these observations, revealing that U was speciated as oxides of varying stoichiometry, with the majority composition of U_3O_7. Coupled with a predominant spherical particle morphology linked to high temperature formation, this suggested a limited interaction of DU impact residues with the surface environment in this soil sample. Images of phase distribution showed localised compositional variations in the particles consistent with

heterogeneous high temperature formation conditions rather than generation of weathering or alteration products.

These results are in contrast to the speciation of U measured in particles recovered from a waste disposal pit for contaminated construction timbers. In these soils the predominant spherical morphology was replaced with platy crystals which were identified as meta-autunite group minerals meta-ankoleite ($K(UO_2)(PO_4)\cdot 3H_2O$) and chernikovite ($H_3O(UO_2)(PO_4)\cdot 3H_2O$) by μ-focus X-ray diffraction and X-ray fluorescence spectroscopy. These differences in morphology and majority U phase distribution are evidence of a substantial weathering effect on the DU residues in this soil sample. As these sample sites are co-located on the Eskmeals firing range, it is suggested that the presence of organic matter from decaying timbers plays a key role in promoting the weathering of U oxide phases, and may also act as a source of phosphate for the formation of meta-ankoleite. It is also known that microbial induced precipitation of U-phosphate phases can occur [3, 4], and a biotic mechanism for the enhanced weathering of DU particle in these soils should also be considered. This invites further investigation, which is discussed below.

A single particle containing a ternary oxide of U and Fe was characterised in Chapter 5. The presence of $UFeO_4$ was verified by μ-focus X-ray diffraction measurements on a ~10 μm DU particle. Characterisation of the U oxidation state was performed by X-ray absorption near edge structure (XANES) and extended X-ray absorption fine structure (EXAFS) spectroscopies coupled with bond valence analysis, which showed that U in the particle was present as U(V). This is the first spectroscopic measurement of the U valence in $UFeO_4$, and directly confirms inferences of the U oxidation state from early measurements of this compound [5, 6]. As this particle arises from the same environmentally aged samples described above, this result provides evidence for the stability of U(V) compounds in oxic surface soil conditions over a number of decades.

The results of micro-analytical X-ray characterisation of speciation presented in Chapter 4 can be compared with those of traditional bulk scale sequential extraction presented in Chapter 6. Despite the clear differences in particle U speciation revealed by microanalysis, the bulk-scale sequential extraction profiles for the two soils are remarkably similar. This is likely due to lack of selectivity of the BCR scheme [7] for different low solubility U phases such as oxides observed in surface soils and U-PO_4 hydrates present in storage pit samples. This highlights that sequential extraction data should be supported by detailed micro analytical characterisation to understand potential interferences. Interpretation of sequential extraction data as a means to quantify speciation should therefore be cautious, and it is perhaps more appropriate to regard these results as an approximate classification of bulk geochemical properties such as contaminant mobility rather than a measure of speciation. This has been noted in previous criticism of sequential extraction techniques [8, 9].

The results presented in Chapter 4 and 5 have additional significance as a successful demonstration of the use of synchrotron microfocus X-ray analysis for chemical characterisation of environmental contaminant particles. The integrated use of spatially resolved microfocus X-ray diffraction with X-ray fluorescence and X-ray absorption spectroscopies was shown to be a powerful tool for characterising contaminant speciation within micro-particles. This approach has the advantages of not requiring destructive sample preparation or high vacuum conditions which may alter the sample. Rapid measurements are made possible by the high flux of synchrotron X-rays, allowing larger numbers of particles or larger sample sizes to be investigated than by conventional laboratory analyses.

The use of spatially resolved X-ray absorption spectroscopy (XAS) imaging to map different U valence states at micron scale resolution was also demonstrated in this investigation. The technique has previously been successfully applied to Fe speciation in archaeological relics [10] and Ce speciation in simulant nuclear waste glass [11], and this project is the first time this approach has been employed to U speciation in environmental materials. Using this approach spatial variations in U oxidation state were resolved, linked to differences in U oxide

stoichiometry (Chapter 4), the presence of U(V) in $UFeO_4$ (Chapter 5), and the formation of U(VI) weathering products (Chapter 4 and 5).

8.1.2 Remediation of DU contaminated soils

A novel batch extraction process for removal of DU from soils by alternate leaching in aqueous ammonium bicarbonate and citric acid solutions was developed. This approach was demonstrated to have higher efficiency for removing DU than single extractions, as the alternating pH of reagents acts to dissolve secondary phases which can form under batch conditions. The precipitation of secondary phases in single batch extraction with ammonium bicarbonate was identified and characterised with microfocus X-ray diffraction and scanning electron microscopy.

The extraction process was shown to be insensitive to differences in U speciation between the two Eskmeals soil samples discussed above. This suggests that bicarbonate and citric acid are highly effective at mobilising U from different low solubility phases. Additionally, the high concentrations of leaching agents used in these batch extractions (0.5M HCO_3^-, 0.1M HCit) likely represent somewhat extreme conditions, under which influence on extraction efficiency from differences in U speciation is suppressed.

This investigation raises the possibility of employing low cost, environmentally compatible reagents, such as citric acid and bicarbonate salts, to achieve effective decontamination of DU laden soils. An engineering system such as heap leaching [12, 13], whereby soils are treated ex-situ in a vessel to isolate effluent leachate from the environment, could provide means to deploy this approach to the field. Scale-up of this kind requires further investigation of the efficiency of the alternating leaching process at larger scales before a full engineering demonstration is feasible.

8.1.3 Remediation of aqueous Cr(VI) by engineered reactive barriers

The reactivity of a novel Pd-functionalised biogenic magnetite ($Fe(II)Fe(III)_2O_4$) system for remediation of aqueous chromate under field-relevant, continuous flow conditions and in the presence of an oxidising co-contaminant was investigated. When supplied with a suitable electron donor, such as sodium formate, the amount of Cr(VI) removed by the hybrid Pd-biomagnetite system increased by over an order of magnitude compared to non-Pd-functionalised control systems. The results also show that the presence of nitrate or dissolved oxygen resulted in only a modest loss in reductive capacity, with around 30% less removal under these conditions compared to an anoxic system. This is of key significance as some reductive remediation materials, such as Fe(0), have been shown to become ineffective in the presence of common oxidising co-contaminants such as nitrate.

Reacted magnetite particles were recovered from columns for analysis. The speciation of Cr was characterised by X-ray absorption spectroscopy, revealing that chromium was reduced from Cr(VI) in the influent solution to Cr(III), with evidence for some substitution of Cr(III) into the spinel structure of the magnetite. Nanoparticles of magnetite were also characterised by scanning transmission electron microscopy, revealing a nanoscale co-association of Cr and Fe. Comparison of these analyses between anoxic and nitrate-amended systems revealed similar characteristics, suggestive of no mechanistic interference of nitrate on the reduction of Cr(VI) by Pd-functionalised magnetite. This work demonstrates the potential of advanced hybrid systems combining precious metal precipitates and nanoscale biogenic minerals for selective remediation of key contaminants, and provides a potential route to effective remediation of chromate in co-contaminated, oxidising waters.

8.2 Further Work

8.2.1 Bioavailability, Environmental Behaviour and Health Risks of Aged DU particles

The data presented in Chapters 4 and 5 provides the first evaluation of changes in DU speciation within munitions particles as a result of aging in two chemically distinct environments. The substantial alteration of DU oxides to weathered uranyl phases, in this case meta-ankoleite and chernikovite, has not been previously reported in characterisation of environmental DU particles, and the process by which this weathering occurs warrants further investigation. In particular, environmentally conditions which promote rapid alteration of DU oxide particles and the speciation of U in resulting weathered phases should be investigated to improve understanding of the long term fate of these residues in a variety of surface environments. The characterisation of secondary phases is particularly important as different U(VI) species can exhibit large variation in solubility and resulting mobility of U in a system [14].

Microbial mediation of the DU alteration process should also be investigated. A first step may be comparative microbial community analyses between the Eskmeals contaminated soil samples which show DU weathering and those that do not to identify viable micro-organisms. This would also give indication of the impact of different U phases on the viability of soil microbes. Selective microcosm experiments may also provide insight on conditions which promote or control microbial action on munitions DU particles. Microbial mediated corrosion of munitions DU alloy has been investigated [15, 16], and a similar programme could be applied to DU particulate residues to understand the role of microbes in their long term environmental behaviour and fate.

To directly link the measured U speciation with environmental behaviour in these altered systems, the bulk scale properties of U in these systems may be investigated. In this work, sequential extraction by the BCR scheme was used as an assay of U partitioning between

different soil fractions and as standardised leaching protocol to compare with the results of remediation experiments. Following on from this, leaching of the soils in biologically relevant fluids such as simulated gastric fluid (SGF) or simulated lung fluid (SLF) to imitate the behaviour of uranium following ingestion or inhalation would provide data on the potential bioavailability of U from these soils by different exposure pathways. This approach has been previously applied for DU particles recovered soon after conflict [17], and application to Eskmeals soils characterised in this study would provide a link between changes in U speciation with bioavailabity and human health risk posed by this contamination.

In Chapter 4 it was hypothesised that the environmentally mediated transformation of U oxides to meta-ankoleite observed in disposal pit soils may serve to stabilise DU in the surface environment as U-PO_4 phases have low solubility at circumneutral pH. One clear route for further work is to study the mobility of U in these systems under simulated environmental conditions. Flow through experiments of U corrosion have been previously applied to evaluate the long term environmental fate of DU metal [18, 19], and such an approach could be used to assess the transport of mobile U from weathered particles in simulated rainwater or other environmentally relevant media. This would link the bulk environmental properties of the contamination with the detailed characterisation of U speciation performed in this work.

8.2.2 Scale-up of DU remediation by chemical extraction

The stepwise batch process demonstrated in Chapter 6 is the first stage in development of a methodology to effectively remediate DU contaminated soil. Further work in this area should focus on increasing the scale of operation to develop this method from a small batch operation to full engineering scale.

The first step could involve small scale continuous flow conditions in soil column experiments to emulate engineered conditions, such as in a heap leaching system. There is extensive literature on modelling of heap leaching for metal extraction using column experiments, which provide model frameworks for interpreting the results of small scale experiments with respect to

a potential field application [20]. Further development could then focus on small scale field trials to probe sensitivity to environmental conditions such as variable temperature, contact with rainwater and exchange of carbonate with the atmosphere. As engineering scale is considered, treatment of the leached solution will also become an important part of the remediation process. As the use of environmentally compatible, low cost reagents was a key advantage of bicarbonate and citric acid leaching, the leachate treatment must also conform to these requirements.

8.2.3 Sustained remediation of Cr(VI) by Pd-functionalised biogenic magnetite

The work presented on Cr(VI) remediation represents an intermediary study between that of batch scale demonstration and field relevant trials of a potentially viable technology. In contrast to the above work on DU remediation this study employs an artificial system, rather than field samples, to test reactivity with respect to Cr(VI), and a clear avenue for further work is to test the ability of this system to remove Cr(VI) under environmentally relevant conditions. This could include addition of other competing anions and redox active species both alone and in combination, to testing using real or simulated contaminated ground waters. The reactivity should also be tested with respect to environmentally relevant Cr(VI) concentrations, which are variable and can be much lower than those used in this study (50 μM). However, this may limit the application of spectroscopic analyses due to lower Cr loadings. One of the key advantages of this system is the retention of Cr(III) within the magnetite structure, which may be more stable to re-oxidation than a surface precipitate, and the maximum structural Cr loading should be optimised. As with all redox reactive remediation schemes, the potential for reoxidation of immobilised Cr(III) in these systems should be investigated.

There are also additional engineering scale challenges, such as increasing the scale of production and functionalisation of biogenic magnetite to generate sufficient quantities for eventual field trials and deployment. Development of the effective delivery of the electron donor, in this case sodium formate, is another challenge. The possibility to generate in-situ a

suitable electron donor able to sustain the biomagnetite reactivity through interaction with Pd functionalised surface should be investigated.

8.2.4 Assessing the environmental impact of tungsten munitions

Tungsten (W) is an alternative material used in armour piercing munitions due to its high density (19 g/cm^3), which is comparable to that of metallic uranium (19.1 g/cm^3). Despite lower armour piercing performance [21], tungsten has been proposed as an alternative material in response to public concerns about the toxicity and radioactivity of DU weapons. However, there are uncertainties about the environmental and human health impacts of using tungsten and tungsten alloys in kinetic energy munitions [22] which should be addressed if such a replacement were to be adopted.

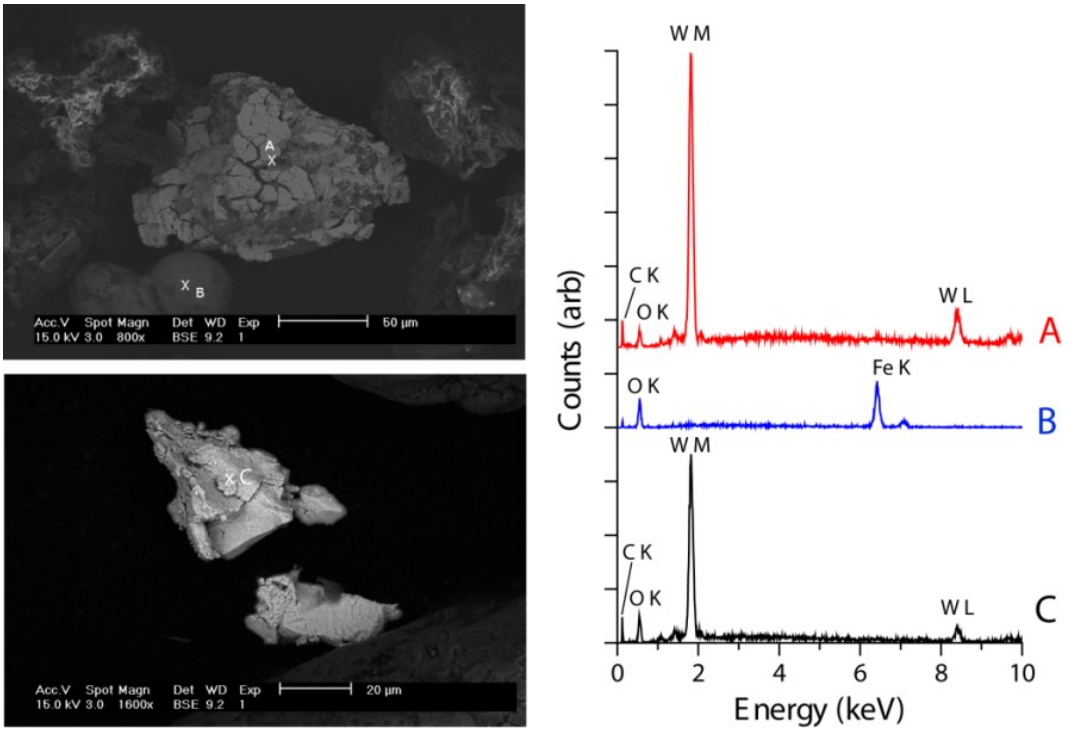

Figure 8.1 – Electron micrographs of W rich particles observed in Eskmeals soils.

Tungsten is not radioactive and is believed to have lower toxicity than uranium. However, although the absolute toxicity of tungsten is not well established and is the subject of developing research [23], early inquiries suggest that inhaled particles of munitions grade tungsten alloys

may be carcinogenic and induce lung injury. [23, 24]. The environmental impact of munitions tungsten in soils is also subject to uncertainty, although various processes have been outlined including soil acidification linked to W dissolution, decrease in soil microbial yields and large transfer factors between soil and biomass W concentrations, indicating high mobility and bioavailability [25].

In Eskmeals soil samples, tungsten rich particles were observed (Figure 8.1), consistent with the use of this range to test armour piercing munitions. It is likely that tungsten was used as a comparison in the development and testing of DU munitions at the site. Although not as numerous as DU particles in these soils, the presence of W residues may lead to additional environmental impact [25]. The characteristic length scale is similar to DU particles, and these residues may be suitable for a study of W speciation using a similar approach to this project. As much of the motivation for returning to W munitions rests on reduced risk to the environment and human health, it will be important to understand how the long term fate of these materials differs from DU residues, and how this influences the longer term evolution of risk factors associated with W munitions. Soils from the Eskmeals site could provide a means to evaluate the environmental risks posed by W particles in direct comparison to that of DU. This research would provide an interesting and important insight on the long term environmental behaviour of W as an alternative to DU in munitions.

8.3 References

[1] Sajih, M.; Livens, F. R.; Alvarez, R.; Morgan, M., Physicochemical characterisation of depleted uranium (DU) particles at a UK firing test range. *Sci Total Environ* **2010,** *408*, (23), 5990-6.

[2] Lloyd, N. S.; Mosselmans, J. F. W.; Parrish, R. R.; Chenery, S. R. N.; Hainsworth, S. V.; Kemp, S. J., The morphologies and compositions of depleted uranium particles from an environmental case-study. *Mineral. Mag.* **2009,** *73*, (3), 495-510.

[3] Martinez, R. J.; Beazley, M. J.; Taillefert, M.; Arakaki, A. K.; Skolnick, J.; Sobecky, P. A., Aerobic uranium (VI) bioprecipitation by metal-resistant bacteria isolated from radionuclide- and metal-contaminated subsurface soils. *Environmental Microbiology* **2007,** *9*, (12), 3122-3133.

[4] Beazley, M. J.; Martinez, R. J.; Sobecky, P. A.; Webb, S. M.; Taillefert, M., Uranium biomineralization as a result of bacterial phosphatase activity: Insights from bacterial isolates from a contaminated subsurface. *Environmental Science & Technology* **2007,** *41*, (16), 5701-5707.

[5] Bacmann, M.; Bertaut, E. F.; Blaise, A.; Chevalier, R.; Roult, G., Magnetic structures and properties of $UFeO_4$. *Journal of Applied Physics* **1969,** *40*, (3), 1131-1132.

[6] Bacmann, M.; Bertaut, E. F.; Bassi, G., Parametres atomqiues et structure magnetique de $UCrO_4$. *Bulletin De La Societe Francaise Mineralogie Et De Cristallographie* **1965,** *88*, (2), 214

[7] Ure, A. M.; Quevauviller, P.; Muntau, H.; Griepink, B., Speciation of Heavy Metals in Soils and Sediments. An Account of the Improvement and Harmonization of Extraction Techniques Undertaken Under the Auspices of the BCR of the Commission of the European Communities. *International Journal of Environmental Analytical Chemistry* **1993,** *51*, (1-4), 135-151.

[8] Brittain, S. R.; Cox, A. G.; Tomos, A. D.; Paterson, E.; Siripinyanond, A.; McLeod, C. W., Chemical speciation studies on DU contaminated soils using flow field flow fractionation linked to inductively coupled plasma mass spectrometry (FlFFF-ICP-MS). *Journal of Environmental Monitoring* **2012,** *14*, (3), 782-790.

[9] Oliver, I. W.; Graham, M. C.; MacKenzie, A. B.; Ellam, R. M.; Farmer, J. G., Distribution and partitioning of depleted uranium (DU) in soils at weapons test ranges - Investigations combining the BCR extraction scheme and isotopic analysis. *Chemosphere* **2008,** *72*, (6), 932-939.

[10] Grolimund, D.; Senn, M.; Trottmann, M.; Janousch, M.; Bonhoure, I.; Scheidegger, A. M.; Marcus, M., Shedding new light on historical metal samples using micro-focused synchrotron X-ray fluorescence and spectroscopy. *Spectrochimica Acta Part B: Atomic Spectroscopy* **2004,** *59*, (10–11), 1627-1635.

[11] Curti, E.; Grolimund, D.; Borca, C. N., A micro-XAS/XRF and thermodynamic study of CeIII/IV speciation after long-term aqueous alteration of simulated nuclear waste glass: Relevance for predicting Pu behavior? *Applied Geochemistry* **2012,** *27*, (1), 56-63.

[12] Hanson, A. T.; Dwyer, B.; Samani, Z. A.; York, D., Remediation of chromium-containing soils by heap leaching – column study. *Journal of Environmental Engineering-Asce* **1993,** *119*, (5), 825-841.

[13] Mason, C. F. V.; Turney, W.; Thomson, B. M.; Lu, N.; Longmire, P. A.; ChisholmBrause, C. J., Carbonate leaching of uranium from contaminated soils. *Environmental Science & Technology* **1997,** *31*, (10), 2707-2711.

[14] VanHaverbeke, L.; Vochten, R.; VanSpringel, K., Solubility and spectrochemical characteristics of synthetic chernikovite and meta-ankoleite. *Mineral. Mag.* **1996,** *60*, (402), 759-766.

[15] Alvarez, R.; Livens, F. R.; Lloyd, J. R.; Holt, J. P.; Boothman, C.; Wincott, P.; Handley-Sidhu, S.; Keith-Roach, M.; Vaughan, D. J., Geochemical and Microbial Controls of the Decomposition of Depleted Uranium in the Environment: Experimental Studies using Soil Microorganisms. *Geomicrobiology Journal* **2011,** *28*, (5-6), 457-470.

[16] Handley-Sidhu, S.; Keith-Roach, M. J.; Lloyd, J. R.; Vaughan, D. J., A review of the environmental corrosion, fate and bioavailability of munitions grade depleted uranium. *Sci Total Environ* **2010,** *408*, (23), 5690-700.

[17] Lind, O. C.; Salbu, B.; Skipperud, L.; Janssens, K.; Jaroszewicz, J.; De Nolf, W., Solid state speciation and potential bioavailability of depleted uranium particles from Kosovo and Kuwait. *Journal of Environmental Radioactivity* **2009,** *100*, (4), 301-307.

[18] Handley-Sidhu, S.; Bryan, N. D.; Worsfold, P. J.; Vaughan, D. J.; Livens, F. R.; Keith-Roach, M. J., Corrosion and transport of depleted uranium in sand-rich environments. *Chemosphere* **2009,** *77*, (10), 1434-1439.

[19] Schimmack, W.; Gerstmann, U.; Schultz, W.; Geipel, G., Long-term corrosion and leaching of depleted uranium (DU) in soil. *Radiation and Environmental Biophysics* **2007,** *46*, (3), 221-227.

[20] Bouffard, S. C.; West-Sells, P. G., Hydrodynamic behavior of heap leach piles: Influence of testing scale and material properties. *Hydrometallurgy* **2009,** *98*, (1-2), 136-142.

[21] Bleise, A.; Danesi, P. R.; Burkart, W., Properties, use and health effects of depleted uranium (DU): a general overview. *Journal of Environmental Radioactivity* **2003,** *64*, (2-3), 93-112.

[22] Braida, W.; Christodoulatos, C.; Ogundipe, A.; Dermatas, D.; O'Connor, G., Electrokinetic treatment of firing ranges containing tungsten-contaminated soils. *Journal of Hazardous Materials* **2007,** *149*, (3), 562-567.

[23] Witten, M. L.; Sheppard, P. R.; Witten, B. L., Tungsten toxicity. *Chemico-Biological Interactions* **2012,** *196*, (3), 87-88.

[24] Roedel, E. Q.; Cafasso, D. E.; Lee, K. W. M.; Pierce, L. M., Pulmonary toxicity after exposure to military-relevant heavy metal tungsten alloy particles. *Toxicology and Applied Pharmacology* **2012,** *259*, (1), 74-86.

[25] Strigul, N.; Koutsospyros, A.; Arienti, P.; Christodoulatos, C.; Dermatas, D.; Braida, W., 54Effects of tungsten on environmental systems. *Chemosphere* **2005,** *61*, (2), 248-258.

Appendicies

Appendix 1 - Supporting Figures for Chapter 4

A1.1 – XANES Calibration Standards

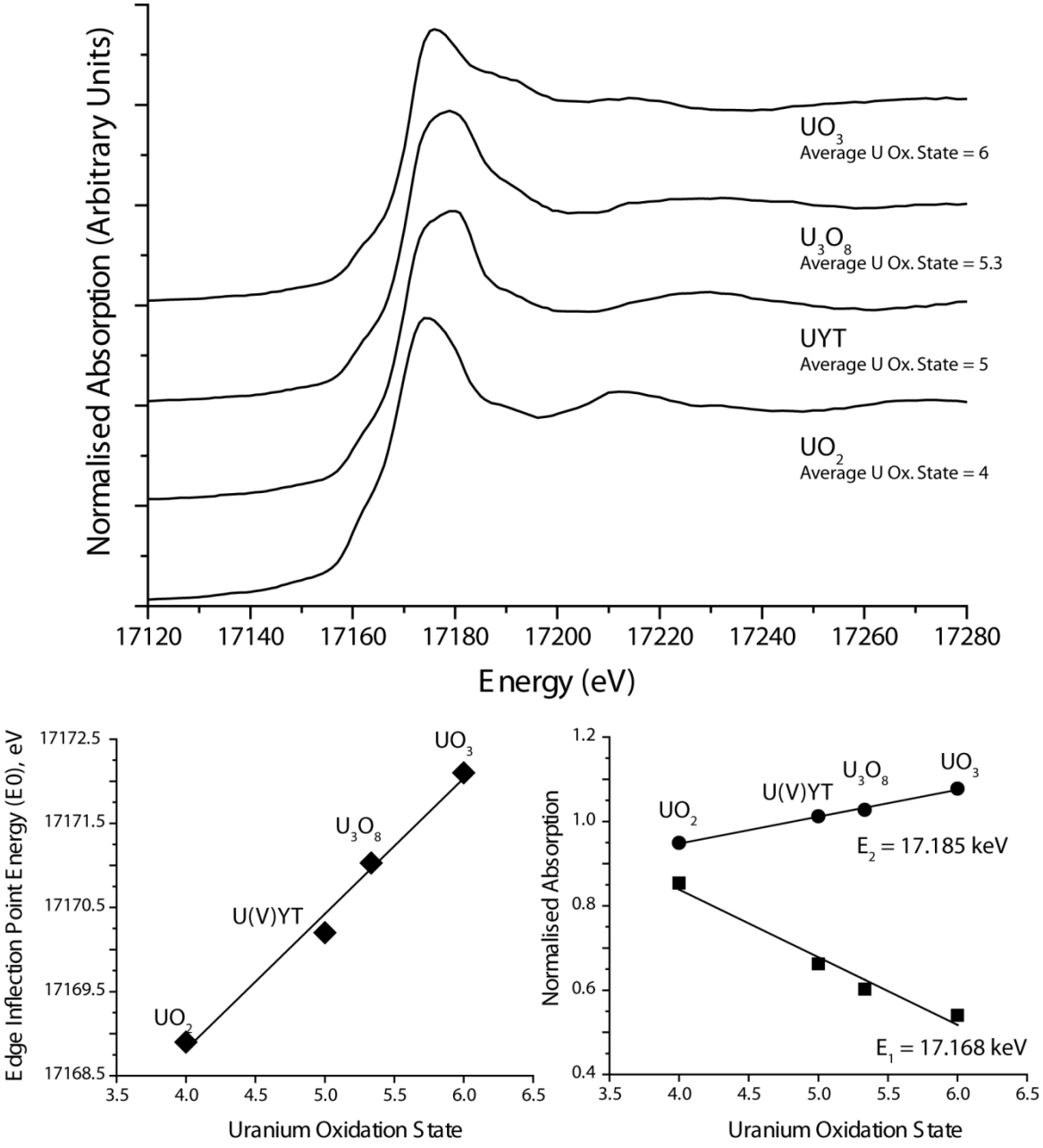

Figure A1.1 – XANES spectra of standards and calibration relationships used for determination of edge position and XAS mapping at near-edge (17.1677 keV) and post-edge (17.195 keV) energies. UYT is $U_{0.5}Y_{0.5}Ti_2O_6$.

A1.2 – Electron Microscopy of Surface Particles

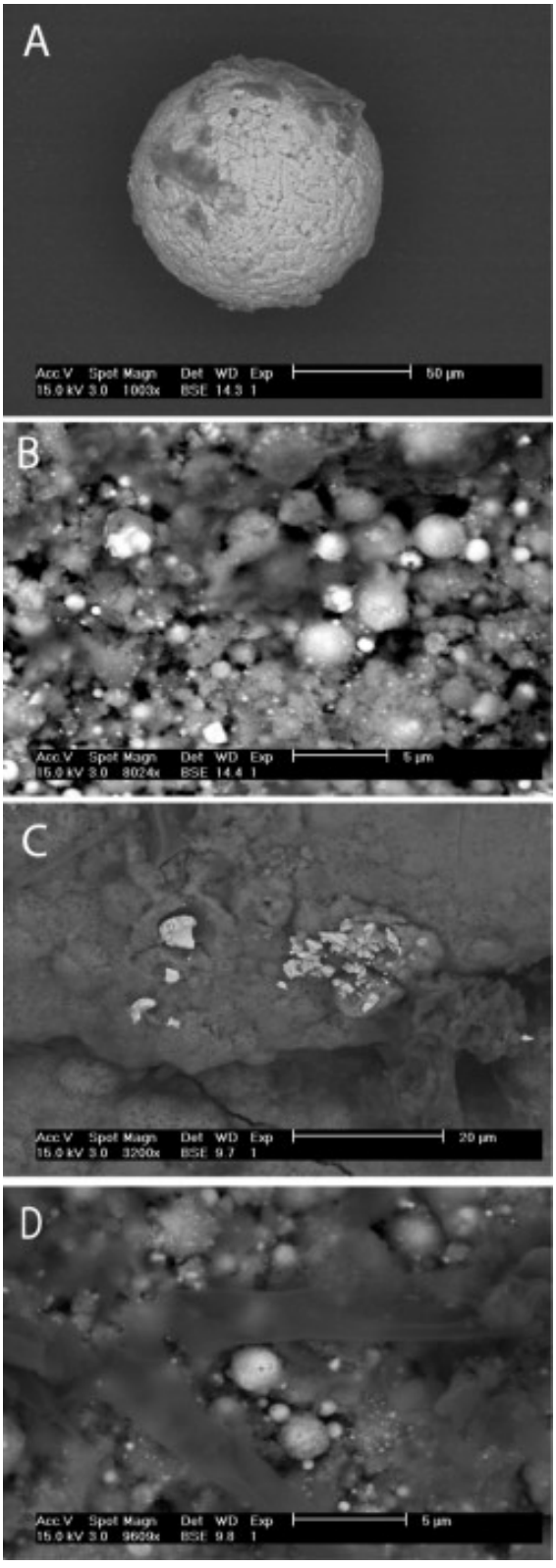

Figure A1.2 – Representative backscattered electron micrographs of DU particles in surface soil samples. Areas which appear brightly were confirmed to contain U by spot EDX analysis.

A1.3 – Mapping Powder Diffraction Patterns

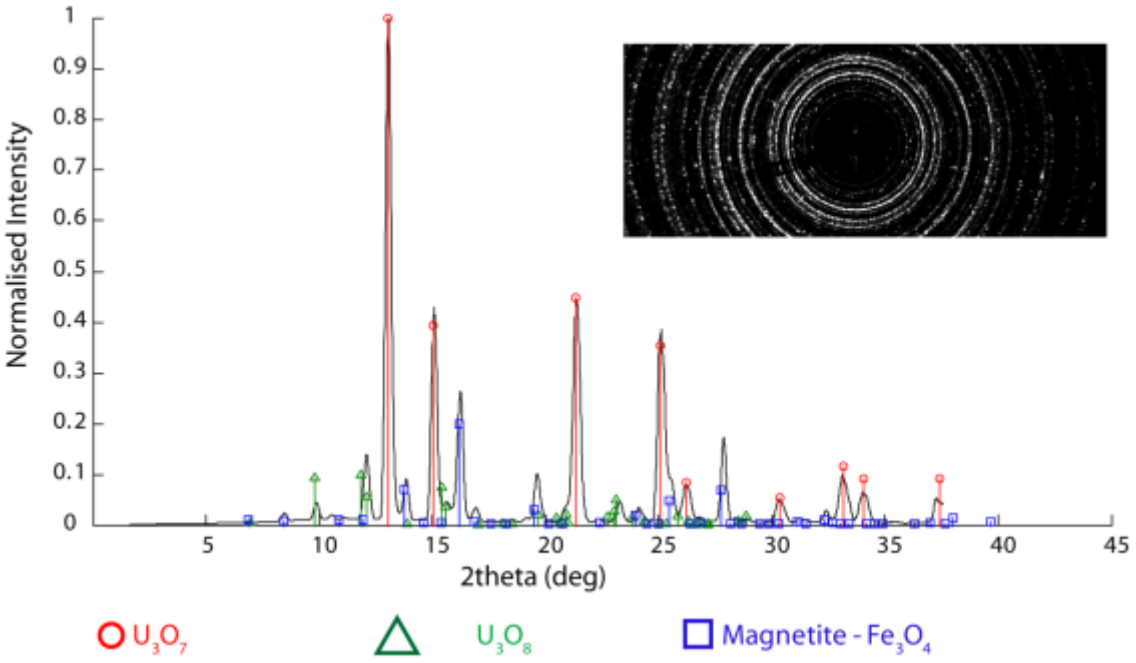

Figure A1.3 – Powder Diffraction pattern for surface particles imaged in Figure 4.3.

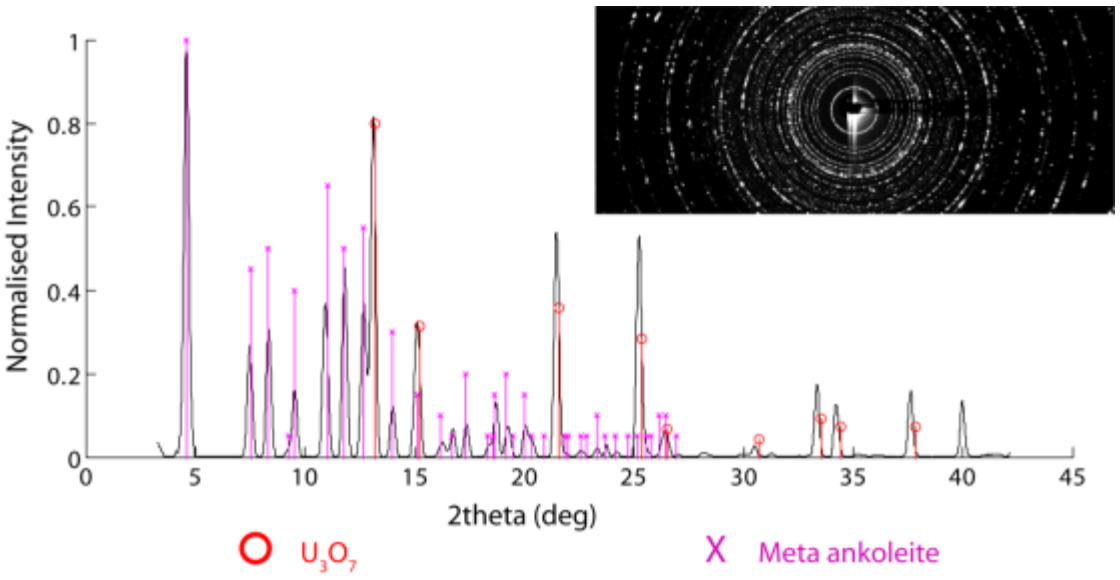

Figure A1.4 – Powder Diffraction pattern for storage pit particles imaged in Figure 4.7.

Appendix 2 - Supporting Figures for Chapter 7

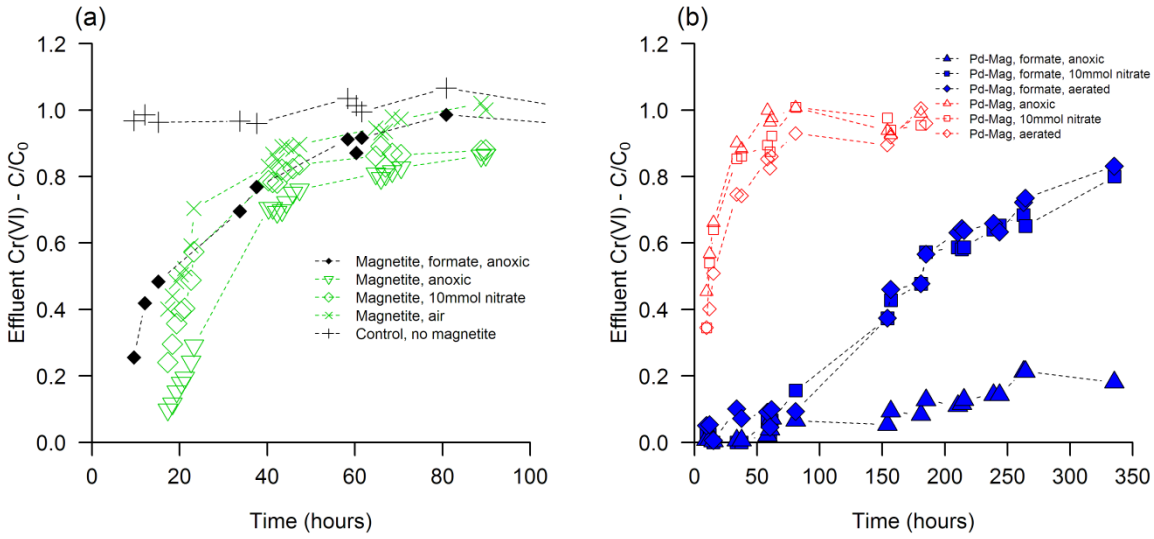

Figure A2.1 – Scaled breakthrough curves for (a) Cr(VI) from magnetite loaded columns and (b) Pd treated magnetite columns, as measured by DPC colorimetric assay. Integration of these curves gives cumulative data shown in Figure 7.1.

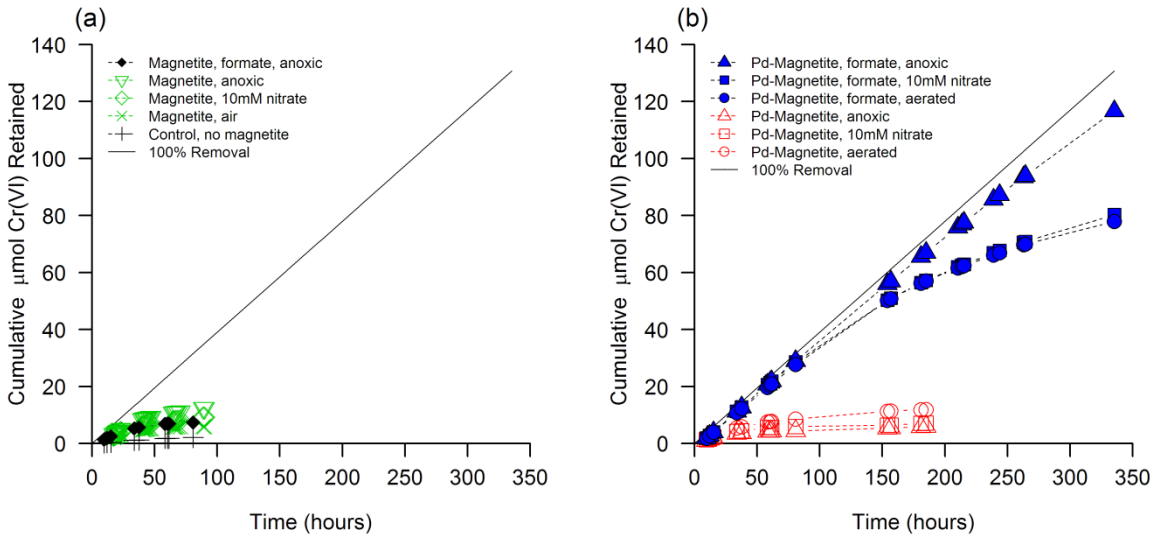

Figure A7.2 - Cumulative Cr(VI) removed from solution in (a) magnetite loaded columns and (b) Pd-functionalized magnetite columns. Curves are formed by integration of column outlet Cr(VI) concentrations (see Figure S1), measured by colorimetric assay. This is an alternative plot of Figure 7.1 with identical axis scaling.

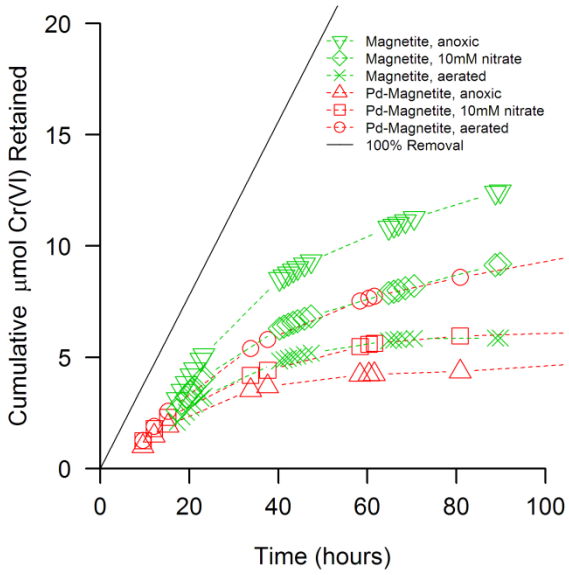

Figure A2.3 – Comparison of 100 hour cumulative Cr(VI) removed from solution by magnetite and Pd-magnetite systems without the addition of formate.

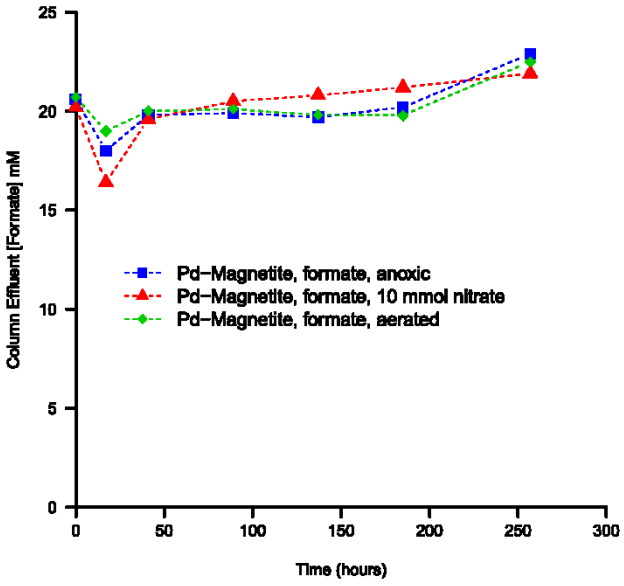

Figure A2.4 – Effluent formate concentrations determined by ion chromatography (IC).

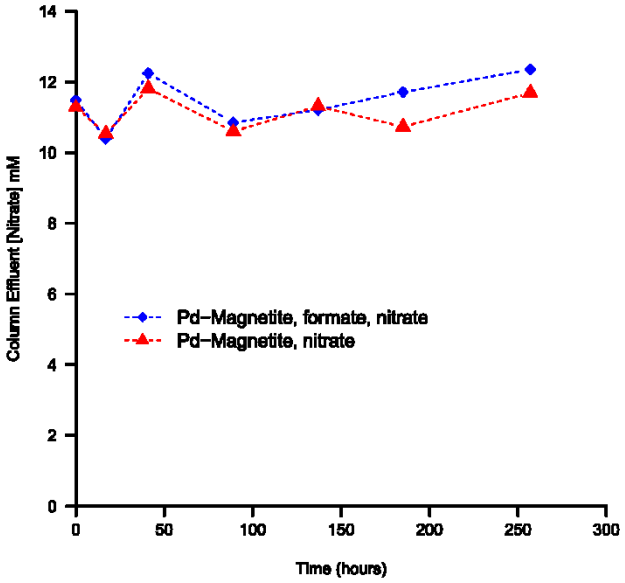

Figure A2.5 – Effluent nitrate concentrations determined by ion chromatography (IC).

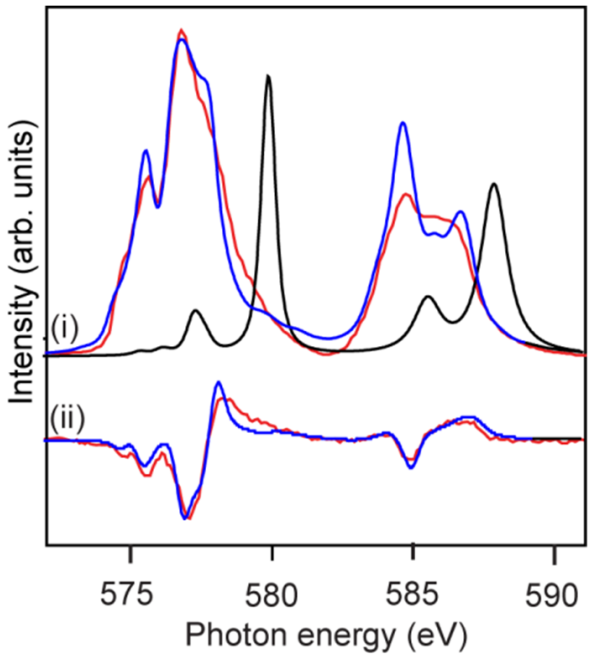

Figure A2.6. Cr $L_{2,3}$-edge (i) XAS of Pd-magnetite with formate anoxic (red) with calculations for Cr(III) (blue) and Cr(VI) (black); (ii) XMCD of Pd-magnetite with formate anoxic (red) and calculation for Cr(III) (blue).

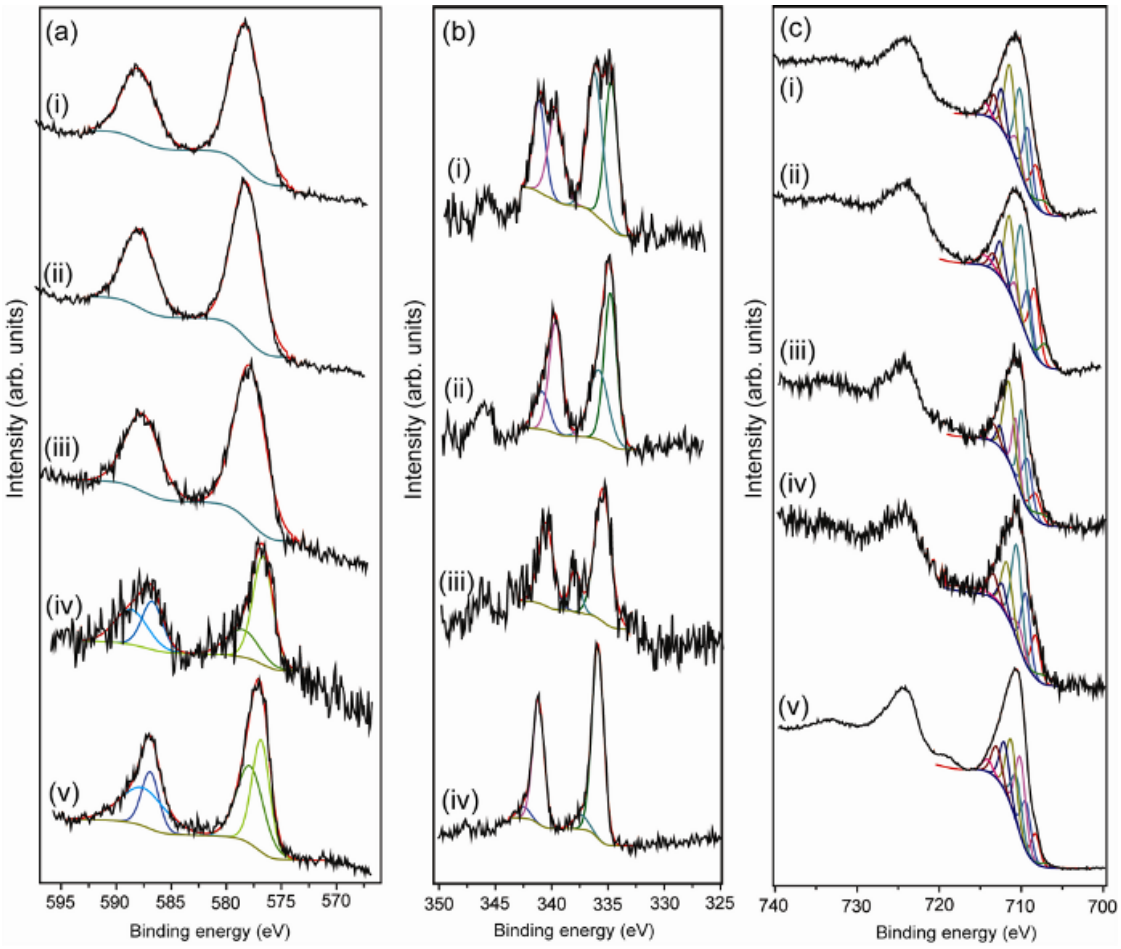

Figure A2.7 - High resolution XPS showing fits of the Cr 2p (a), Pd 3d (b) and Fe 2p (c) regions for Pd-magnetite with formate anoxic (i) anoxic with nitrate (ii); Pd magnetite without formate anoxic (iii) anoxic with nitrate (iv); Magnetite with formate under anoxic conditions (v) (Cr 2p & Fe 2p only). Fitting components are detailed in Tables A2.1, A2.2 and A2.3.

X-ray Photoelectron Fitting Components

Table A2.1- Cr 2p fitting components for X-ray photoelectron spectra based on Cutting et al. (2010); Kendelewicz et al. (1999).

	Cr									
	Cr2p3/2				Cr 2p1/2				%	
	Cr(III)		Cr(VI)		Cr(III)		Cr(VI)		Cr(III)	Cr(VI)
	Peak (BE)	%	Peak (BE)	%	Peak (BE)	%	Peak (BE)	%		
Pd-magnetite, formate, anoxic	577.2	63.7	-	-	586.9	36.3	-	-	100	0
Pd-magnetite, formate, nitrate	577.0	64.0	-	-	586.7	36.0	-	-	100	0
Pd-magnetite, anoxic	578.0	65.0	-	-	587.8	35.0	-	-	100	0
Pd-magnetite, nitrate	576.7	30.2	578.6	12.4	586.8	26.7	588.3	30.8	57	43
Magnetite, formate, anoxic	576.9	27.3	577.9	17.7	586.9	22.1	587.5	32.9	49	51

Table A2.2 - Pd 3d fitting components for X-ray photoelectron spectra based on Wagner et al. (1979) and Kim et al. (1974).

	Pd									
	Pd 3d5/2				Pd 3d3/2				%	
	Pd-metal		Pd-oxide		Pd-metal		Pd-oxide		Pd-metal	Pd-oxide
	Peak (BE)	%	Peak (BE)	%	Peak (BE)	%	Peak (BE)	%		
Pd-magnetite, formate, anoxic	335.1	24.3	336.7	29.6	340.4	23.1	342.0	22.9	47	53
Pd-magnetite, formate, nitrate	335.2	30.2	336.3	20.4	340.4	14.3	341.0	35.1	44	56
Pd-magnetite, anoxic	335.5	47.3	337.9	10.5	340.5	34.8	342.0	7.5	82	18
Pd-magnetite, nitrate	335.9	48.3	337.4	4.4	341.1	44.2	342.4	3.1	92	8

Table A2.3 - Fe $2p^{3/2}$ fitting components for X-ray photoelectron spectra based on Gupta & Sen (1975) and McIntyre & Zetaruk (1977).

	Fe 2p3/2													
Sample	Fe2+ Component 1		Fe2+ Component 2		Fe2+ Component 3		Fe3+ Component 1		Fe3+ Component 2		Fe3+ Component 3		Fe3+ Component 4	
	Peak (BE)	%	Peak (BE)	%	Peak (BE)	%	Peak (BE)	%	Peak (BE)	%	Peak (BE)	%	Peak (BE)	%
Pd-magnetite, formate, anoxic	708.3	11.5	709.3	15.2	710.6	5.8	710.2	23.4	711.5	22.4	712.5	8.9	713.4	5.1
Pd-magnetite, formate, nitrate	708.4	16.4	709.1	10.6	710.8	4.0	710.0	26.0	711.4	20.8	712.6	8.4	713.4	3.9
Pd-magnetite, anoxic	708.4	8.6	709.4	15.6	710.8	13.4	710.1	18.9	711.6	26.8	712.7	4.8	713.5	5.8
Pd-magnetite, nitrate	708.4	10.4	709.3	15.6	710.6	16.7	710.2	14.0	711.5	19.2	712.4	13.2	713.5	7.3
Magnetite, formate, anoxic	708.3	7.0	709.4	12.9	710.6	13.1	710.1	21.8	711.2	18.6	712.1	12.8	713.0	9.0

A2.1 References

Gupta R. P. and Sen S. K. (1975) Calculation of multiplet structure of core p-vacancy levels II. Phys. Rev. B 12(1), 15–19.

Kendelewicz, T.; Liu, P.; Doyle, C. S.; Brown, G. E.; Nelson, E. J.; Chambers, S. A. X-ray absorption and photoemission study of the adsorption of aqueous Cr(VI) on single crystal hematite and magnetite surfaces. *Surf. Sci.* **1999**, *424*, 219–231.

Kim, K. S.; Gossmann, A. F.; Winograd, N. X-ray photoelectron spectroscopic studies of palladium oxides and the palladium-Oxygen electrode. *Anal. Chem.* **1974**, *46*, 197–200.

McIntyre N. S. and Zetaruk D. C. (1977) X-ray photoelectron spectroscopic studies of iron oxides. Anal. Chem. 49, 1521–1529.

Wagner, C. D.; Riggs, W. M.; Davis, L. E.; Moulder, J. F.; Muilenberg, G. E., *Handbook of X-ray Photoelectron Spectroscopy*; Perkin Elmer Corporation: Eden Prairie, MN, 1979.

Appendix 3 – Publications List

A3.1 – Journal Articles

Crean, D. E.; Coker, V. S.; van der Laan, G.; Lloyd, J. R., Engineering Biogenic Magnetite for Sustained Cr(VI) Remediation in Flow-through Systems. *Environmental Science & Technology* **2012,** *46*, (6), 3352-3359.

Crean, D. E.; Livens, F. R.; Sajih, M.; Stennett, M. C.; Grolimund, D.; Borca, C. N.; Hyatt, N. C., Remediation of soils contaminated with particulate depleted uranium by multi stage chemical extraction. *Journal of Hazardous Materials*, **2013**, In Press. DOI:10.1016/j.jhazmat.2013.08.013

Crean, D. E.; Livens, F. R.; Stennett, M. C.; Grolimund, D.; Borca, C. N.; Hyatt, N. C., Micro-analytical X-ray imaging of depleted uranium speciation in environmentally aged munitions residues.*Environmental Science and Technology,***2014,** In press.

A3.2 – Conference Proceedings

Goldschmidt 2013

Crean D, Livens F, Stennett M, Grolimund D, Borca C & Hyatt N, Characterisation of Depleted Uranium Munitions Residues by Synchrotron X-Ray Microanalysis. *Mineralogical Magazine* **2013**, *77*(5), 925

Goldschmidt 2011

Coker V, Crean D, Cutting R, Telling N, Byrne J, Pattrick R, van der Laan G, Vaughan D & Lloyd J, Bioengineering Nano-Magnetite for Contaminant Clean-Up. *Mineralogical Magazine* **2011**, *75*(3) 686

A3.3 – Others

Call for Evidence - Managing Radioactive Waste Safely: Review of the Siting Process for a Geological Disposal Facility. A collective response of postgraduate and postdoctoral researchers

of the Immobilisation Science Laboratory Research Group, The University of Sheffield. Lead contact - Kris James, other contact - Daniel Crean, other contact – Dr. Claire Corkhill.**2013**

A3.4 – In preparation and submitted

Crean, D. E.; Livens, F. R.; Stennett, M. C.; Grolimund, D.; Borca, C. N.; Hyatt, N. C., Determination of the uranium oxidation state in $UFeO_4$ by X-ray microanalysis of an environmental hot particle. *In preparation for submission*.

Crean D.E.; Bailey, D. J.; Stennett, M. C.; Blackwell, T. B.; Corkhill, C. L.; Tappero, R.; Ravel, B; Hyatt, N.C.; A Synchrotron X-ray Micro-Spectroscopy Study of the Explosive Melt Glass Derived From the Trinity Nuclear Test. *In prepration for submission*

Corkhill, C.L.; Bridge, J.W.; Gardner, L.J.; Hillel, P.; Tappero, R; Crean, D.E.; Stennett, M.C.; Hyatt, N.C.; Immobilisation of technetium-99 on backfill cement candidates: sorption under static and saturated flow conditions. *In preparation for submission*